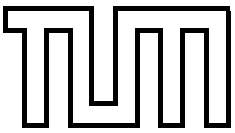

Fakultät für Physik
der Technischen Universität München

Max-Planck-Institut für Biochemie
Abteilung für Molekulare Strukturbiologie

Structural studies of the 26S proteasome and its interaction with Ubp6 by cryo-electron microscopy

Antje Renate Aufderheide

Vollständiger Abdruck der von der Fakultät für Physik
der Technischen Universität München
zur Erlangung des akademischen Grades eines
Doktors der Naturwissenschaften (Dr. rer. nat.)
genehmigten Dissertation.

Vorsitzender:		Univ.-Prof. Dr. M. Rief
Prüfer der Dissertation:	1.	Hon.-Prof. Dr. W. Baumeister
	2.	Univ.-Prof. Dr. M. Zacharias

Die Dissertation wurde am 13.10.2016 an der Technischen Universität München eingereicht und durch die Fakultät für Physik am 06.12.2016 angenommen.

Contents

List of Figures

List of Tables

Summary

The 26S proteasome is responsible for the degradation of proteins that are marked for destruction by ubiquitin chains into smaller polypeptides. It is composed of the central core particle (CP), harbouring the catalytic sites, and one or two regulatory particles (RP) regulating the access to the CP. An RP contains six RP triple-A-ATPase (Rpt) subunits forming an AAA-ATPase module and thirteen non-ATPase (Rpn) subunits. In order to understand the molecular mechanisms of this molecular machine, its detailed structure is required.

Single-particle cryo-electron microscopy (SP cryo-EM) is an excelling method for the structural characterisation of large and heterogeneous complexes, such as the 26S proteasome. Three-dimensional (3D) densities of the purified complex of interest are computed from the cryo-EM projections and classification methods allow to distinguish different conformations present in the dataset.

The aim of this thesis is to further the mechanistic understanding of the 26S proteasome. Towards this aim, two aspects were studied by SP cryo-EM. Firstly, the structural basis of the reciprocal regulation of the 26S proteasome and the most abundant proteasome interacting protein (PIP), the deubiquitylating enzyme Ubp6, was investigated in the presence and absence of the Ubp6 inhibitor ubiquitin aldehyde (UbAld), which mimics substrate binding. Ubp6 binds to the RP subunit Rpn1 via its ubiquitin-like domain. In the absence of UbAld the catalytic domain of Ubp6 is located variably, whereas the addition of UbAld stabilises this domain in a position where it binds to the ATPase subunit Rpt1, suitable for acting on a substrate already engaged by the ATPase module. Binding of Ubp6, and in particular Ubp6–UbAld, changes the conformational space of the 26S proteasome holocomplex, which may explain effects of Ubp6 on the kinetics of proteasomal degradation.

The second project aimed to improve the resolution of 26S proteasome reconstructions. A workflow was implemented that is tailored to the peculiarities of the 26S proteasome and makes use of movies, acquired by modern detectors. The workflow was applied to a dataset of the human 26S proteasome yielding a 3.9 Å resolution structure, which served as a basis for atomic model building. The high resolution structure allowed the detection of nucleotides bound to all six Rpt subunits and revealed previously unidentified features of several Rpn subunits, most likely involved in coordinating the RP subunits during the degradation process.

Taken together, this thesis provides first insights into the reciprocal regulation of the 26S proteasome and PIPs, as well as the most detailed structure of the substrate-accepting 26S proteasome conformation to date.

Zusammenfassung

Das 26S Proteasom zerlegt Proteine, die durch Polyubiquitinketten für den Abbau markiert sind, in kleinere Polypeptide. Es besteht aus einem zentralen, proteolytisch aktiven 20S Kernkomplex (CP) und ein oder zwei regulatorischen 19S Komplexen (RPs), die den Zugang zum CP regulieren. Die RPs sind aus einer ATPase mit sechs RP Tripel-A-ATPase (Rpt) Untereinheiten, sowie dreizehn Nicht-ATPase (Rpn) Untereinheiten aufgebaut. Um die Wirkungsweise dieser molekularen Maschine zu verstehen sind detaillierte strukturelle Untersuchungen notwendig.

Kryo-Elektronenmikroskopie (cryo-EM) in Kombination mit Einzelpartikelanalyse (SPA) ermöglicht die strukturelle Untersuchung von großen und heterogenen Proteinkomplexen, wie z.B. dem 26S Proteasom. Diese Methode erlaubt es, dreidimensionale (3D) Strukturen von Proteinen und Proteinkomplexen zu berechnen und konformelle Unterschiede mit Hilfe von Klassifikation zu unterscheiden.

Das Ziel dieser Arbeit ist es, zu einem besseren mechanistische Verständnis des 26S Proteasoms beizutragen. Dafür wurden zwei Aspekte mit Hilfe der SPA untersucht. Als erstes wurde die gegenseitige Regulierung des 26S Proteasoms und des deubiquitylierenden Enzyms Ubp6 in Gegenwart und Abwesenheit des Ubp6-Inhibitors Ubiquitin Aldehyd (UbAld) analysiert. Ubp6 bindet mit einer Ubiquitin-ähnlichen Domäne an die RP Untereinheit Rpn1. Die zweite, katalytisch aktive Domäne kann viele verschiedenen Positionen einnehmen und wird erst unter Bindung von UbAld so stabilisiert, dass sie an Rpt1 bindet und dadurch nahe der zentralen Öffnung des ATPase-Rings gebundene Substrate prozessieren kann. Ubp6 und insbesondere Ubp6–UbAld verändern den Raum der eingenommenen Konformationen des 26S Proteasoms. Dies bietet eine Erklärung für Änderungen in der Proteinabbau-Kinetik in der Gegenwart von Ubp6.

Der zweite Teil der Arbeit zielte darauf ab, die Auflösung von SPA Rekonstruktionen des 26S Proteasoms zu verbessern. Dafür wurde ein Bildverarbeitungsprotokoll implementiert, das auf die Besonderheiten von 26S Proteasom-Datensätzen zugeschnitten ist und das die Vorteile der von modernen Kameras aufgezeichneten Einzelbilderstapel nutzt. Die Anwendung des Protokolls auf einen Datensatz des humanen 26S Proteasoms resultierte in einer durchschnittlich zu 3.9 Å aufgelösten Dichte, die es ermöglichte ein atomares Model zu erstellen. In der Dichte sind Nukleotide an allen sechs Rpt Untereinheiten sichtbar. Außerdem geben einige bislang unentdeckte Einzelheiten von Rpn Untereinheiten Hinweise auf die Koordination der Untereinheiten während des Proteinabbaus.

Damit erzielte diese Arbeit die bislang detailierteste Struktur des 26S Proteasoms und erste strukturelle Erkenntnisse über die Wechselwirkung mit PIPs.

1 Introduction

The 26S proteasome, a 2.5 MDa large protein complex, is responsible for regulated disassembly of proteins into smaller polypeptides in the cytosol and nucleus of eukaryotic cells. The 26S proteasome is part of the ubiquitin proteasome system, described in section 1.1. The subunits of the 26S proteasome and their arrangement within the complex are introduced in section 1.2. Whereas the overall architecture of the 26S proteasome has been elucidated, the interaction with transiently-binding partners remains to be explored. In this context, proteins which interact with the 26S proteasome are discussed in section 1.3, with emphasis on the deubiquitylating enzyme Ubp6 (subsection 1.3.1). A method that is highly suitable for 3D structural characterisation of the 26S proteasome complex is single particle cryo-electron microscopy (SP cryo-EM), as described in section 1.4. Finally, the aims of this work are formulated in section 1.5.

1.1 The Ubiquitin Proteasome System

In all cells the abundance of proteins is highly regulated. Many proteins must be degraded to avoid cellular stress and apoptosis. For example, specific proteins must not be present in specific states of the cell cycle and others have defects that may cause toxic aggregates. In eukaryotic cells, the ubiquitin-proteasome-system (UPS) is responsible for inter-cellular protein degradation [Hershko and Ciechanover, 1998; Finley, 2009; Finley et al., 2012]. Protein degradation by the UPS is highly specific, which is achieved by attachment of polyubiquitin chains to substrates through a cascade of E1/E2/E3 enzymes (Figure 1.1.1). In a first step, ubiquitin (Ub) binds to an ubiquitin-activating enzyme (E1) in an ATP-dependent manner. In the second step, E1 enzymes facilitate the transfer of Ub to the ubiquitin-conjugating enzymes (E2). This transfer is followed by binding of the E2 enzyme to an ubiquitin ligase (E3), which also binds the substrate protein. Depending on the type of E3 ligase, Ub is either transferred directly from the E2 enzyme to the substrate or it binds transiently to the E3 ligase during this process [Glickman and Ciechanover, 2002; Berndsen and Wolberger, 2014]. There is a large variety of E3 ligases, which is the

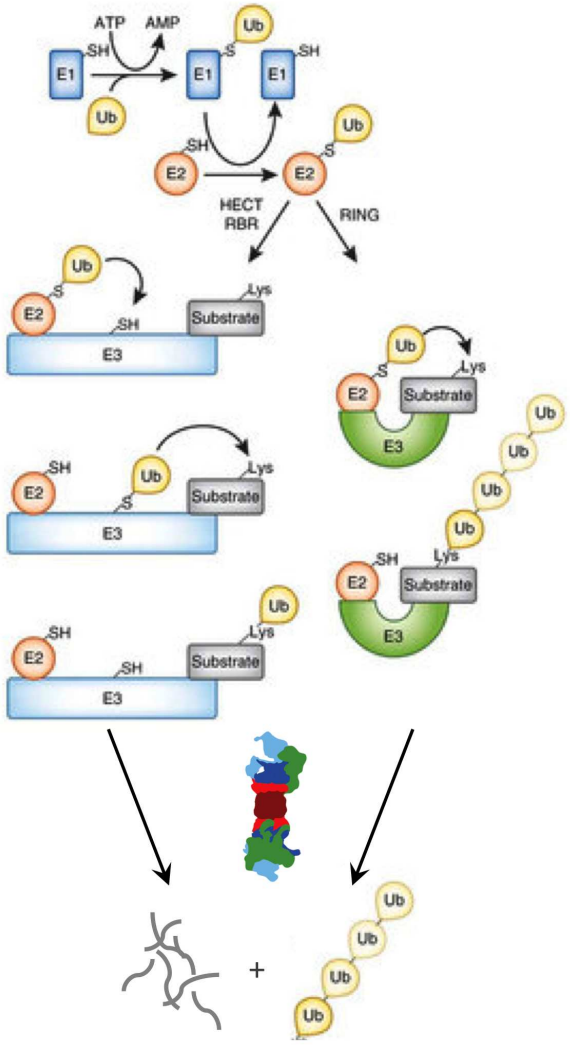

Figure 1.1.1: The ubiquitin-proteasome-system: An ubiquitin activating enzyme (E1) binds an ubiquitin molecule in order to transfer it to an ubiquitin conjugating enzyme (E2). The E2 enzyme then interacts with an E3-ligase, by which the ubiquitin is transferred to the substrate to be marked. Whereas E3-RING ligases (*Really Interesting New Gene*) mediate a direct transfer of ubiquitin from the E2 enzyme to the substrate, HECT ligases (*Homology to E6AP C Terminus*) bind the ubiquitin moiety in an intermediate step. Subsequently, the ubiquitylated substrate is recognised and degraded by the 26S proteasome, releasing the ubiquitin chain. Figure taken from [Unverdorben, 2014]

main means to achieve specificity in protein degradation via the UPS [Berndsen and Wolberger, 2014]. Proteins, which have been Ub-marked for degradation by the E1-E2-E3 cascade, are recognised by the 26S proteasome, a large protease of 2.5 MDa molecular weight.

Polyubiquitin chains are formed through bonds between one of the seven lysine residues of one Ub (most commonly K11, K48 or K63) and the C-terminal residue (G76) of the ligated Ub. The chains can be linear or branched and of different size in order to cause proteasomal degradation of the substrate, with K48-linked chains being the most common degradation signal [Kravtsova-Ivantsiv and Ciechanover, 2012; Finley et al., 2012]. For a long time, a minimum length of 4 Ub moieties was believed to be required for efficient recognition by the 26S proteasome [Thrower et al., 2000]. A recent study showed that for substrates ubiquitylated at multiple sites 2 diubiquitin chains lead to better recognition [Lu et al., 2015]. In some cases of small proteins even monoubiquitin is sufficient [Kravtsova-Ivantsiv and

Ciechanover, 2012]. For longer chains, Meyer and colleagues demonstrated that branching can increase the efficiency of recognition by the 26S proteasome [Meyer and Rape, 2014].

In addition to polyubiquitylated substrates, the 26S proteasome can further degrade a small number of proteins without prior ubiquitylation [Kravtsova-Ivantsiv and Ciechanover, 2012]. Most of these proteins have large unfolded regions and can also be directly degraded by the 20S core particle [Takeuchi et al., 2007].

Unstructured regions are also required for the degradation of ubiquitylated substrates and serve as initiation sites for degradation [Prakash et al., 2004]. Their specific position, amino acid composition and distance to the ubiquitylation site influences the degradation efficiency [Sharipo et al., 1998; Inobe et al., 2011] and directionality [Berko et al., 2012] (reviewed in [Aufderheide et al., 2015b]). Degradation of many substrates of the UPS is assisted by the AAA-ATPase Cdc48 [Beskow et al., 2009; Richly et al., 2005]. Such assistance is particularly required for substrates without unstructured regions that can serve as initiation sites [Beskow et al., 2009].

The UPS and in particular the 26S proteasome are key players in fundamental processes in the cell, such as cell-cycle regulation, protein-quality controle and apoptosis [Finley et al., 2012; Jung and Catalgol, 2009]. Defects in the UPS pathway have been associated with pathologies including neurodegenerative diseases [Hershko and Ciechanover, 1998; Glickman and Ciechanover, 2002].

1.2 The 26S proteasome

The 26S proteasome constitutes the executive arm of the UPS. The 2.5 kDa large protein complex consists of a barrel-shaped 20S core particle (CP), which harbours the catalytically active sites, and one or two 19S regulatory particles (RPs), which flank the CP on either end and regulate the entrance to the CP (Figure 1.2.1) [Peters et al., 1993]. If two RPs attach, a so-called double-capped 26S proteasome forms, which measures ∼48 nm in length and ∼20 nm in width [Voges et al., 1999]. The following sections will describe the 26S proteasome architecture in more detail.

1.2.1 The 20S core particle

The 20S core particle assembles from 28 subunits, which arrange in four stacked heptameric rings (see Figure 1.2.1). The two outer rings are each formed by seven related α-subunits (α-rings). The two inner rings contain the same amount of β-subunits (β-rings), which belong to the class of N-terminal nucleophilic (Ntn) hy-

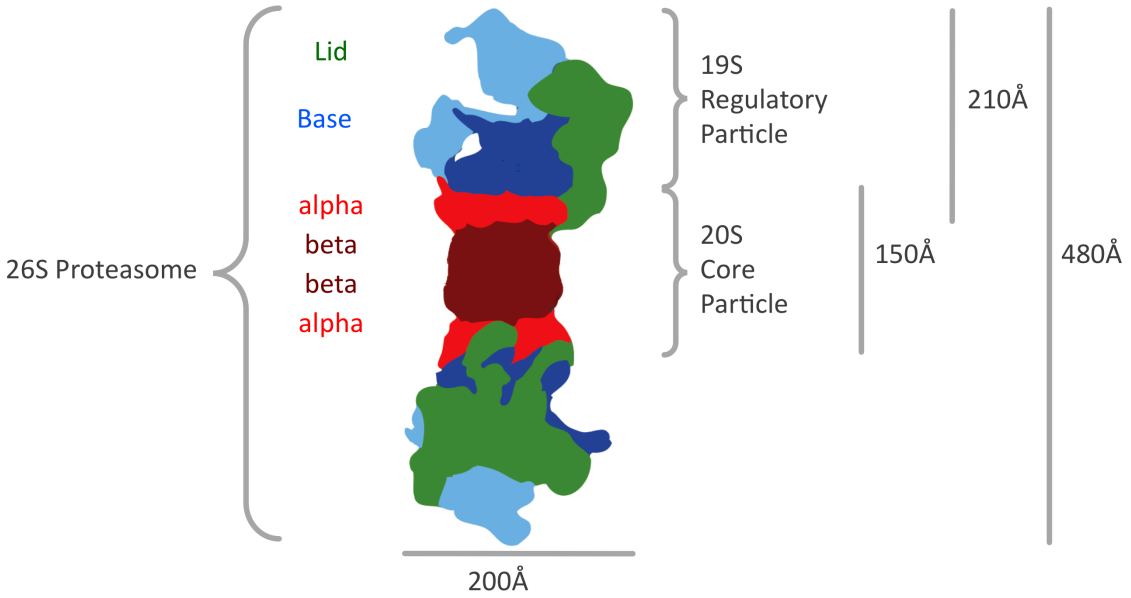

Figure 1.2.1: Overall architecture and dimensions of the 26S proteasome with two RPs attached to the CP. Figure taken from [Unverdorben, 2014]

drolases [Borissenko and Groll, 2007]. The overall architecture of the CP is evolutionary highly conserved, whereas the composition of the heptameric rings differs. In archea, 14 identical copies of α and β subunits form a D7-symmetrical complex [Löwe et al., 1995]. In bacteria, the 20S is only present in actinomycetes and includes one or two types of α and β subunits [Aoyama et al., 1996; Nagy et al., 1998]. In eukaryotic cells, the heptameric rings are formed by 7 different α or β subunits (Figure 1.2.2 A), which assemble in a C2-symmetrical CP [Groll et al., 1997].

In eukaryotes, only three of the seven β subunits, β_1,β_2 and β_5, possess catalytically active sites with caspase-like, trypsin-like, and chymotrypsin-like activity, respectively [Borissenko and Groll, 2007; Finley, 2009; Tomko and Hochstrasser, 2013]. These active sites are positioned in an inner cavity, formed by the two β-rings (Figure 1.2.2 B). The β-rings are sandwiched between the α-rings giving rise to two 'antechambers', which are responsible for maintaining the substrate in an unfolded state until it is degraded in the inner cavity [Ruschak et al., 2010].

The enzymatic activity of the 20S is fairly unspecific. To confer selectivity, the access to the 20S chambers has to be controlled, which is facilitated by the N-terminal tails of the α-subunits, in particular those of α_2, α_3 and α_4 (Figure 1.2.2 C). These tails form gates at the ends of the CP and restrict the entry to unfolded substrates [Wenzel and Baumeister, 1995; Groll et al., 2000; Jung and Grune, 2013].

Throughout the different types of organisms, there is a variety of so-called activators, which bind to the ends of the CP and regulate the access of substrates

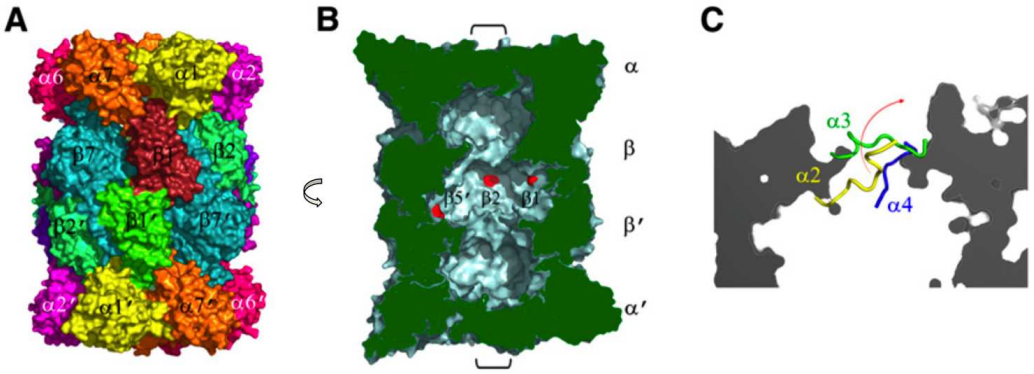

Figure 1.2.2: The eukaryotic 20S core particle. (A) Seven distinct subunits for the α- and β- rings, which form the C2-symmetrical CP. (B) Cut-open and rotated view of the CP. The three active sites are rendered in red. The brackets indicate the position of the CP gates in the α-rings. (C) Close up on the CP gate. The N-terminal tails of α_2, α_3 and $\alpha 4$, which control access to the CP are depicted in yellow, green and blue, respectively. The arrow indicates a suggested movement of the tails upon gate opening. Figure adapted from [Finley et al., 2012]

(reviewed in [Stadtmueller and Hill, 2011]). These activators can be divided into three major subclasses: 11S activators, Blm10 activators (both ATP-independent) and ATP-dependent activators. ATP-dependent activators are ring-shaped complexes formed by AAA-ATPases and exist in bacteria, arcea and eukaryotes (reviewed in [Förster et al., 2013]).

In eukaryotic cells, the ATP-dependent activator is the 19S RP. Among other subunits the RP includes an AAA-ATPase module, which interacts with the CP-α subunits via its C-terminal ends [Tian et al., 2011].

1.2.2 The 19S regulartory particle

The 19S RP of *S. cerevisiae* consists of 19 stoichometric subunits, divided into 6 RP TripleA-ATPases (Rpt1-6) and 13 RP NonATPases (Rpn1-3,5-13,15) [Glickman et al., 1998b; Voges et al., 1999]. Some of them are orthologs with similar structures. A proteasome, cOP9 Signalosome, eIF3 Translation initiation factor (PCI)-domain is found in 6 Rpns (Rpn3,5,6,7,9,12). Two Rpn subunits include a Mpr1/ Pad1 N-terminal (MPN)-domain (Rpn8,11). Finally, Rpn1 and Rpn2 have a proteasome/ cyclosome (PC)-Repeat in common (reviewed in [Förster et al., 2010]).

These subunits form two subcomplexes, which are referred to as the 'lid' and the 'base' for historical reasons. The base subunits are Rpt1-6, Rpn1, Rpn2 and Rpn13 [Glickman et al., 1998a; Schreiner et al., 2008; Husnjak et al., 2008; Sakata et al., 2012]. The lid contains the remaining subunits Rpn3,6-9,11,12 [Glickman et al.,

1998a] and Rpn15 (referred to as Sem1 in yeast) [Funakoshi et al., 2004; Sone et al., 2004; Bohn et al., 2013] with the exception of Rpn10, which is neither part of the base nor the lid but attaches to the lid subunits Rpn8,9 [Sakata et al., 2012; Beck et al., 2012].

While the structure of the 20S was solved about two decades ago [Voges et al., 1999], the structure of the 19S remained largely elusive until two recent studies unraveled the subunit arrangement through different approaches [Lasker et al., 2012; Lander et al., 2012]. Both studies concluded essentially the same arrangement of the RP subunits in *S. cerevisiae*, depicted in Figure 1.2.3. Additionally, a pseudo-atomic model was obtained from an integrative modelling approach based on a CEM density at subnanometer resolution [Beck et al., 2012].

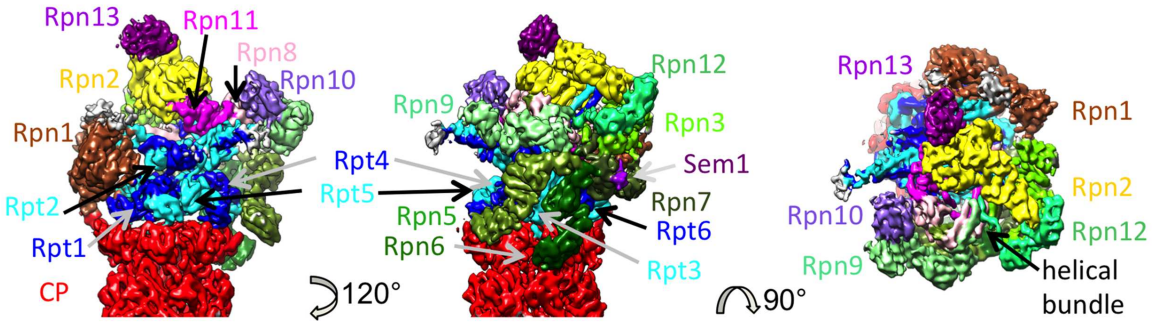

Figure 1.2.3: Structural arrangement of the RP subunits. The reconstruction from *S. cerevisiae* particles (EMDB entry 2592) is shown from 3 different views, coloured according to the subunits extracted from PDB entry 4cr2. The names of the subunits are indicated in the respective colours.

The AAA-ATPase, assembled by Rpt1-6, is placed on top of the CP. The six Rpt subunits form two stacked rings with a channel leading to the gate of the CP. This AAA-ATPase module constitutes the central part of the base and binds the PC-domain containing subunits Rpn1 and Rpn2. Rpn1 is bound by the coiled-coil of Rpt1/2 and positioned next to the ATPase subunits Rpt1,2,6. Rpn2 interacts with the coiled-coil of Rpt6/3, is positioned on top of the ATPase ring and binds Rpn13. The PCI subunits of the lid (Rpn3,5,6,7,9,12) form a horseshoe-shaped scaffold, which stretches over the full height of the RP. The subunits Rpn3,12 bind to Rpn2, forming connections between lid and base, Rpn3,7 are tethered by the small subunit Rpn15, Rpn5,6 reach down to the CP and Rpn9 binds Rpn10. The MPN-domain subunits Rpn8/11 are positioned in the center of the RP, above the channel formed by the AAA-ATPase ring.

Proteins marked for degradation by ubiquitin are recognised by the Ub-receptors, Rpn10 and Rpn13, where they bind with low affinity. During an ATP-dependent step the substrate is engaged with higher affinity ('commitment', [Peth et al., 2010]).

In a subsequent step the marked protein is unfolded by the AAA-ATPase module of the 26S proteasome and translocated into the 20S core particle for degradation. During this process, Rpn11 cleaves off the polyubiquitin-chain and the Ub-moieties can be reused.

The following paragraphs give further details on the RP subunits grouped corresponding to their structural and functional roles.

The AAA-ATPases

The six *S. cerevisiae* AAA-ATPase (ATPase associated with diverse cellular activities) subunits Rpt1-6 arrange in a circle and form two stacked rings. The bigger ring contains the AAA-domains of the Rpt subunits and resides on the CP α-ring. The smaller ring, stacked on top, consists of the oligosaccharide-binding (OB) domains. The N-termini of the Rpts lead from the OB-ring into coiled coils formed by pairs of two neighbouring Rpts (Rpt1-Rpt2,Rpt6-Rpt3,Rpt4-Rpt5) [Förster et al., 2009; Tomko et al., 2010].

Each Rpt contributes one N-terminal α-helix to a coiled-coil. The two helices from an Rpt-pair twist around each other caused by an interaction mediated by specific residues, which repeatedly occurs every 7 residues. Normally, the number of residues per α-turn is 3.6. Therefore, the helices of coiled-coils are distorted to enable the interaction after 7 residues, i.e. after two α-turns [Lupas and Gruber, 2005]. Coiled-coil regions have been identified in many functionally important areas of proteins [Lupas et al., 1991]. In the 26S proteasome, the coiled-coil of Rpt1/2 binds to Rpn1 and that of Rpt6/3 interacts with Rpn2 as well as with several lid subunits (Figure 1.2.3, [Beck et al., 2012]).

The C-terminal tails of Rpt2,3,5 exhibit a conserved motif of a hydrophobic (Hb) residue, followed by a tyrosine and a residue of any kind (HbYX). These residues can bind to groves between the α-subunits. Thereby, the ATPase associates with the CP [Smith et al., 2011; Tian et al., 2011]. In the *S. cerevisiae* 26S proteasome the HbYX motifs of Rpt2 and Rpt3 were identified to tightly bind in the pockets of the α-ring, whereas Rpt5 binds more flexibly [Beck et al., 2012; Tian et al., 2011].

During proteasomal degradation, the ATPase engages the substrate, unfolds it and translocates it into the CP [Peth et al., 2010; Zhang et al., 2009b] in an ATP-dependent manner. Therefore, each Rpt harbours a nucleotide binding site in its AAA subdomain formed by a Walker A and a Walker B motif. The bound nucleotide is further stabilised by two arginine (Arg) fingers from the neighbouring Rpt subunit, which reach towards the Walker A motif (reviewed in [Wendler et al.,

2012]). The Rpt subunits are arranged in a lockwasher-like topology [Sledz et al., 2013]. Therefore, the interaction between the Arg-fingers and the nucleotide binding site of the neighbouring subunit is always interrupted at one interface. Depending on the conformational state of the RP (subsection 1.2.3), this interruption is found at the interface of Rpt3 and Rpt6 or that of Rpt5 and Rpt1 [Sledz et al., 2013; Unverdorben et al., 2014]. In order to translocate substrates, each Rpt subunit has a so-called pore loop, which is a hydrophobic aromatic (Ar-Φ) loop positioned in the AAA-domain and which protrudes into the channel formed by the ring of the 6 Rpts. The lockwasher-like topology of the ATPase induces a staircase arrangement of these pore loops [Lander et al., 2012, 2013].

Substrate translocation was found to be coordinated over the pore loops of the Rpt subunits [Iosefson et al., 2015]. Recent studies show that also the binding and hydrolysis of ATP is coordinated over the ATPase ring [Kim et al., 2015; Iosefson et al., 2015]. However, it is less clear to which degree [Olivares et al., 2016].

Rpn1 and Rpn2

Rpn1 and Rpn2 are the largest of the RP subunits and part of the base subcomplex, binding to the ATPase via the coiled coils of Rpt1-Rpt2 and Rpt6-Rpt3, respectively. The overall structures of Rpn1 and Rpn2 are highly similar. They share a large domain, containing PC repeats, which arrange in an α-helical toroid [Kajava, 2002; He et al., 2012], whereas the N-terminal domains are positioned differently [He et al., 2012; Beck et al., 2012].

Rpn1 and Rpn2 both serve as binding platforms for integral subunits of the 26S proteasome as well as proteasome interacting proteins (PIPs) [Rosenzweig et al., 2012]. However, their functions within the 26S proteasome holocomplex appear to differ. Rpn2 binds the ubiquitin receptor Rpn13 and tightly interacts with the lid subunits Rpn3,12,11 at its N- and C-terminal parts [Chen et al., 2010; Beck et al., 2012; Lander et al., 2013], whereas Rpn1 itself has been identified as a ubiquitin receptor and a major hub for PIP binding [Leggett et al., 2002; Elsasser et al., 2002; Gomez et al., 2011; Shi et al., 2016]. These different roles of Rpn1 and Rpn2 within the 26S holocomplex, despite their similar structure, might be due to their different positioning. Whereas Rpn2 is tightly incorporated into the RP, Rpn1 is in a very exposed position (Figure 1.2.3), ideal for the interaction with PIPs.

The ubiquitin receptors

Rpn10 and Rpn13, the two integral Ub-receptors [van Nocker et al., 1996; Schreiner et al., 2008; Husnjak et al., 2008], are located in the periphery of the RP [Sakata et al., 2012]. Rpn13 binds to Rpn2 [Husnjak et al., 2008; Chen et al., 2010] and Rpn10 to Rpn8 and Rpn9 [Beck et al., 2012; Lander et al., 2013]. These locations expose them (compare Figure 1.2.3), which serves their function of recruiting polyubiquitylated substrates. The two Ub-receptors bind Ub in different ways. Rpn13 has a Pleckstrin-like receptor for ubiquitin (PRU) domain, which interacts with Rpn2 and simultaneously with Ub or ubiquitin-like (UBL) domains through loops [Husnjak et al., 2008]. In contrast, Rpn10 interacts with Ub via ubiquitin interacting motifs (UIMs), which are helices connected by flexible domains. The number of UIMs varies depending on the organism (reviewed in [Tomko and Hochstrasser, 2013]).

Rpn13, which is a stoichiometic subunit in *S. cerevisiae*, is only present in substoichiometric amounts in *S. pombe* as well as in human 26S proteasomes [Bohn et al., 2010; Chen et al., 2010; Schweitzer, 2016]. Interestingly, Rpn13 as well as Rpn10 are not essential [Sakata et al., 2012; Husnjak et al., 2008], which hints that their function can be compensated by shuttling Ub-receptors (sUbR), a group of PIPs discussed in more detail in section 1.3.

The PCI-domain containing subunits and Rpn15

The subunits Rpn3,5,6,7,9 and 12 arrange in a horseshoe manner through assembly of their PCI-domains in the order Rpn9/5/6/7/3/12 (Figure 1.2.3 middle) [Lasker et al., 2012; Lander et al., 2012]. They are located on the side of the base subunits and reach over the full hight of the RP. Rpn3,12 interact with Rpn2 , while the N-terminal parts of Rpn5,6 contact the CP and, therefore, have been suggested to function as a clamp connecting the RP and the CP [Pathare et al., 2012]. Towards the C-terminal end, the PCI subunits form helices that assemble into a helical bundle, which also engages C-terminal helices of Rpn8,11 and, thereby, ties the lid subunits together [Beck et al., 2012; Estrin et al., 2013; Dambacher et al., 2016].

The small subunit Rpn15, is also part of the horseshoe, although it does not have a PCI domain. It contains a small helix and a large region without any secondary structure elements. In the 26S holocomplex, the helix of Rpn15 is located between Rpn7 and Rpn3, stabilising the interaction of the two subunits [Bohn et al., 2013] as well as the overall 26S proteasome [Funakoshi et al., 2004; Sone et al., 2004]. Rpn15 has been found to bind Ub and, therefore, might act as an additional Ub-receptor [Paraskevopoulos et al., 2014].

The MPN-domain containing subunits

The MPN subunits Rpn8 and Rpn11 belong to the class of deubiquitinating enzymes (DUBs). However, only Rpn11 is catalytically active, as the Zn^{2+}-dependent JAB1/MPN/Mov34 metaloenzyme (JAMM) domain is missing in Rpn8 [Pathare et al., 2014; Worden et al., 2014]. Rpn8,11 form a heterodimer, which is positioned on the inside of the horseshoe, between the Ub-receptors Rpn10,13 and the entrance of the ATPase ring (Figure 1.2.3). As described above, the C-terminal helices of Rpn8,11 interact with the PCI subunits through the helical bundle, forming the lid subcomplex.

In the isolated lid, Rpn11 is inhibited through an interaction with Rpn5. During integration into the 26S holocomplex, the lid undergoes a significant rearrangement, activating Rpn11 [Dambacher et al., 2016]. Additionally, the DUB activity of Rpn11 is coupled to ATP-hydrolysis [Verma et al., 2002; Yao and Cohen, 2002], i.e. substrate processing. This can be explained by conformational changes of the RP during the degradation process (see subsection 1.2.3), as the active site of Rpn11 is only accessible in states associated with substrate processing by the ATPase. Once active, Rpn11 cleaves off the entire polyubiquitin chain in one step [Verma et al., 2002; Yao and Cohen, 2002].

1.2.3 Different conformational states of the RPs

To date three different conformational states of the 26S proteasome are known [Unverdorben et al., 2014]. They were determined from isolated 26S proteasomes in the presence of ATP or ATP-γS and are referred to as the s1, s2 and s3 states (Figure 1.2.4 A). The s1 state is predominant in the presence of ATP [Bohn et al., 2010; Lander et al., 2012; Beck et al., 2012; Unverdorben et al., 2014], whereas the s3 state is induced by ATP-γS [Sledz et al., 2013]. The s2 conformation is present in low amounts in both conditions [Unverdorben et al., 2014] (Figure 1.2.4 B).

A comparison of the three states reveals s2 as an intermediate conformation. From the s1 to the s2 state the ATPase shifts, improving the alignment of the ATPase pore with the CP gate. Additionally, the lid subunits and Rpn2 undergo a 25° rotation (Figure 1.2.4 C&D left). This rotation places Rpn5 and Rpn6 further apart and locates Rpn11 directly above the entrance to the pore of the ATPase (Figure 1.2.4 A). This motion of Rpn11 renders its active site accessible for substrates. A switch from the s2 to the s3 state is accomplished by a shift and rotation of the ATPase and a shift of the outer lid subunits (Figure 1.2.4 C&D right). Most significantly, the Rpt subunits undergo a rearrangement, which aligns the ATPase pores with the gate

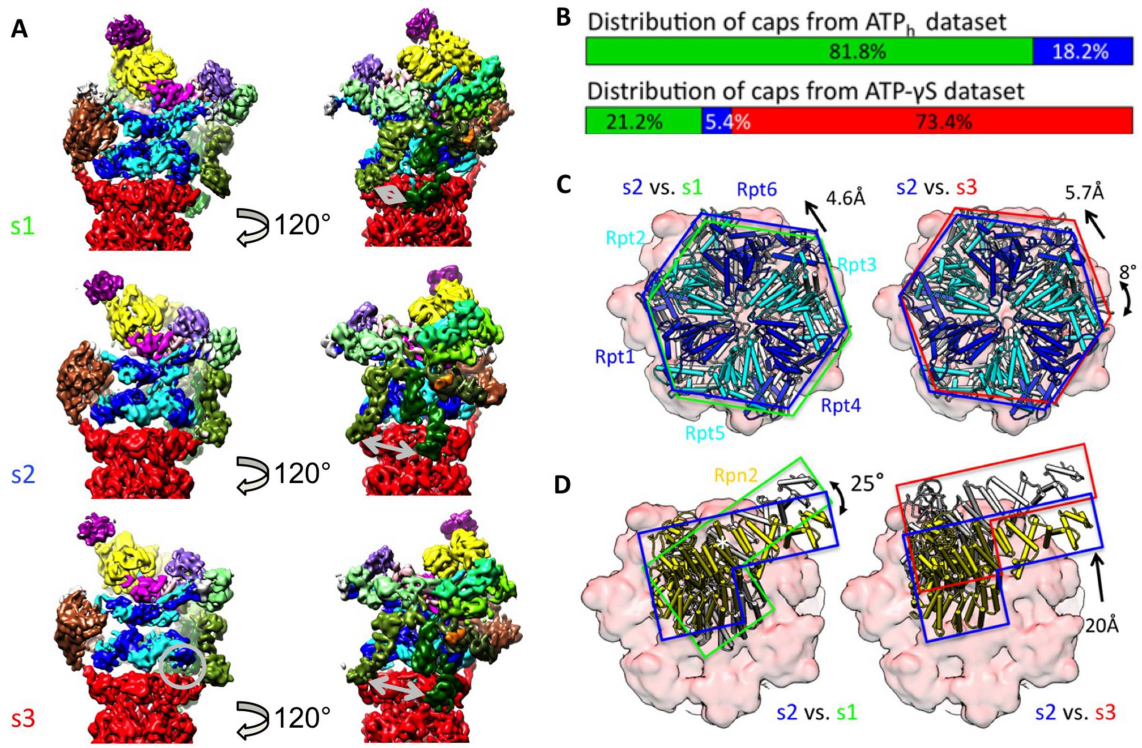

Figure 1.2.4: The three conformational states of the 26S proteasome. (A) 3D reconstructions coloured with respect to the subunits as in Figure 1.2.3, Rpn15/Sem1 (orange). The main structural differences seen in these two views are marked with grey arrows and circles. (B) occupancy of the states in the different datasets. (C&D) Top view onto different parts of the RP with respect to the 20S (red in background) (C) The AAA-ring of the ATPase shifts and rotated between the three states. (D) Rpn2 visualises the lid movements between the states. Figure adapted from [Unverdorben et al., 2014].

and, thereby, enables substrate translocation [Sledz et al., 2013; Unverdorben et al., 2014]. Interestingly, this rearrangement changes the staircase formed by the pore loops. In the s1 and s2 state the staircase spans from Rpt2 (lowest) to Rpt3 (highest). In comparison, in the s3 state the staircase has a lower pitch with Rpt1 in the highest and Rpt5 in the lowest position [Sledz et al., 2013; Matyskiela et al., 2013].

The s3 state was not only found in the presence of ATP-γS but also in 26S proteasomes bound to ubiquitylated substrates [Matyskiela et al., 2013]. Taken together, the results from the different studies lead to hypothesise a functional model of the three states [Unverdorben et al., 2014]. This model suggests, that ubiquitylated substrates are recognised in the s1 state ('substrate accepting state'). The s2 state constitutes a 'commitment state', during which the substrate is engaged by the ATPase. This step is followed by translocation and degradation of the substrate in the s3 state ('translocating state').

In an *in-situ* study by cryo-electron tomography (CET) on neuronal cells, 26S proteasomes were identified in the s1 and s3 state [Asano et al., 2015], suggesting that

the s2 state may constitute a rather short-lived state in the cell environment that eludes detection at this point due to limited resolution and sensitivity. Interestingly, the subtomogram average of s3-like particles showed a large extra density most likely caused by PIPs assisting the degradation procedure [Asano et al., 2015].

1.3 Proteasome interacting proteins

There is a variety of proteasome interacting proteins (PIPs) in the cell. They bind to the 26S proteasome transiently [Wang and Huang, 2008] and typically dissociate during the purification procedures applied to the 26S proteasome [Sakata et al., 2011]. There are three major functional groups of proteins among the most abundant PIPs (reviewed in [Schmidt et al., 2005; Finley, 2009; Finley et al., 2012; Förster et al., 2014]). Firstly, the shuttling Ub receptors (sUbR), such as Rad23,

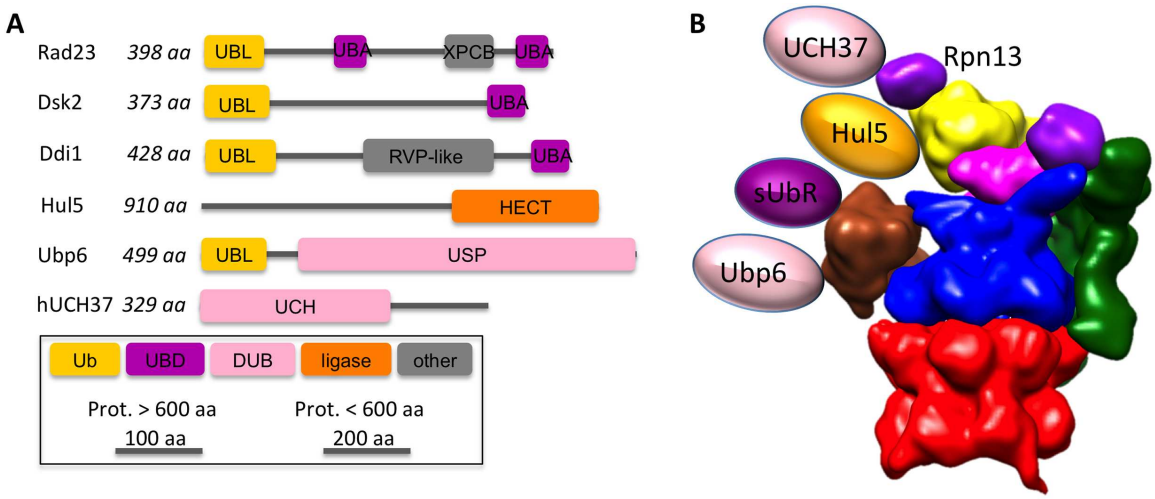

Figure 1.3.1: Proteasome interacting proteins. (A) Schematic representation of the domains of the most abundant PIPs. Yellow: domains with an Ub-related fold; purple: domains that bind to Ub and Ub-related domains (UBD); pink: DUB domains; orange: ubiquitin ligase domains; gray: established domains with different or unknown functions. (B) The major PIPs bind to Rpn1 and Rpn2. In higher eukaryotes UCH37 binds to the Ub-receptor Rpn13. Figure adapted from [Förster et al., 2014]

Dsk2 or Ddi1, function as dynamic Ub receptors additional to the integral receptors Rpn10,13 [Leggett et al., 2002; Gomez et al., 2011]. Secondly, DUBs, such as Ubp6 (Usp14 in mammals) and hUCH37 (not present in yeast), trim Ub chains. Thirdly, a group of Ub ligases extends Ub chains of substrates bound to the 26S proteasome, with Hul5 the most abundant among PIPs [Leggett et al., 2002].

PIPs mainly bind to the subunit Rpn1 and in some cases also to Rpn2 [Elsasser et al., 2002; Saeki et al., 2002; Rosenzweig et al., 2012; Shi et al., 2016]. However,

in higher eukaryotes some PIPs with a Ub-like (UBL) domain have been shown to bind to the Ub receptors Rpn10 and Rpn13 [Hamazaki et al., 2006; Hiyama et al., 1999; Walters et al., 2002]. Figure 1.3.1 summarises the domains and proteasomal interaction partners of the major PIPs.

All major PIPs include a large number of domains, which are predicted to be disordered and presumably render them structurally highly flexible (reviewed in [Aufderheide et al., 2015b]). In particular the UBL domains (Figure 1.3.1), responsible for docking to the 26S proteasome, are connected to the functional regions through unstructured domains, presumably supporting the complex formation process, as suggested for human Rad23 [Walters et al., 2003]. These unstructured connections in PIPs may additionally allow the functional domains to adopt various positions, when bound to the 26S proteasome.

1.3.1 Ubp6 - a major proteasome interacting protein

The ubiquitin specific protease 6 (Ubp6, Usp14 in mammals) is a 57 kDa large DUB and the most abundant PIP in 26S proteasome purifications [Sakata et al., 2011; Lander et al., 2012]. It consists of a UBL domain, followed by a flexible linker of ~25 amino acids and an ubiquitin- specific- protease (USP) domain containing the catalytically active site (Figure 1.3.1 A) for hydrolysing linkages of Ub moieties.

Due to its USP domain, Ubp6 belongs to the DUB family of ubiquitin specific proteases. In total, there are five different DUB families, which can be divided into two main groups depending on their mechanism of deubiquitylation (reviewed in [Komander et al., 2009; Komander, 2010]). The DUBs from the JAMM/MPN+ family, which includes Rpn11, cleave Ub linkages with the help of coordinated zinc ions. In contrast, the DUBs from all other families, which include the PIPs Ubp6 and UCH37, act through a catalytic cystein residue.

The UBL domain of Ubp6 has been shown to interact with the 26S proteasome by binding to Rpn1 [Elsasser et al., 2002; Rosenzweig et al., 2012]. The activity of Ubp6 is low in isolation but increases significantly when Ubp6 interacts with the 26S proteasome [Borodovsky et al., 2001; Leggett et al., 2002; Hu et al., 2005]. In contrast to the integral DUB Rpn11, which removes polyubiquitin chains *en-bloc* while the substrate is already translocated to the CP [Verma et al., 2002; Yao and Cohen, 2002] (section 1.2.2), Ubp6 has been reported to trim ubiquitin chains successively and may, thereby, free bound substrates from degradation [Lee et al., 2011]. However, a recent study showed that for cyclin B ubiquitylated at multiple sites, proteasome-bound Ubp6 removes chains *en-bloc* until a single chain remains [Lee et al., 2016].

The differing results illustrate that the mechanisms of deubiquitylation by Ubp6 are not fully understood yet.

Ubp6 was reported to delay the degradation of folded, polyubiquitylated substrates [Hanna et al., 2006; Lee et al., 2010]. Interestingly, the catalytic activity is not required for this inhibitory effect [Hanna et al., 2006]. In contrast to the delay of the degradation of folded substrates, binding of Ub-conjugates or the USP inhibitor ubiquitin aldehyde (UbAld) to proteasome-bound Ubp6 enhances the degradation of short unfolded peptides by the CP [Peth et al., 2009] and activates the proteasomal ATPases [Peth et al., 2013].

The structures of the USP domains of Ubp6 and Usp14 were solved by X-ray crystallography [Hu et al., 2005]. However, the structure of Ubp6 in complex with the 26S proteasome remains unknown. Structural insights into the 26S–Ubp6 complex would be valuable to understand the mechanisms of proteasomal regulation by Ubp6.

1.4 3D electron-cryo microscopy

Electron microscopy (EM) is a suitable method for high-resolution imaging of proteins and protein complexes such as the 26S proteasome. The resolution is generally limited by the wavelength used for imaging (see section 1.4.3). High-energy electrons have a much smaller wavelength than visible light or X-rays [Förster et al., 2012], making them ideal for high-resolution structure determination.

1.4.1 Electron - specimen interaction

High energy electrons passing through matter undergo electrostatic Coulomb interactions with the atoms therein, resulting in elastic and inelastic scattering [Reimer and Kohl, 2008].

Elastic scattering is mostly due to the electrostatic interaction between the incident electron and the nucleus of an atom, in which the energy transfer from the electron to the specimen is negligible. The higher the atomic number of a specimen atom and the closer the electron passes by the nucleus the larger is the resulting angular deviation from the incoming direction, which may also lead to back-scattering (see Figure 1.4.1).

Inelastic scattering results from an interaction of the incoming electron with specimen electrons and results in an energy deposition in the specimen. There are two types of interaction of inelastic scattering most relevant for EM : (1) Intra- and

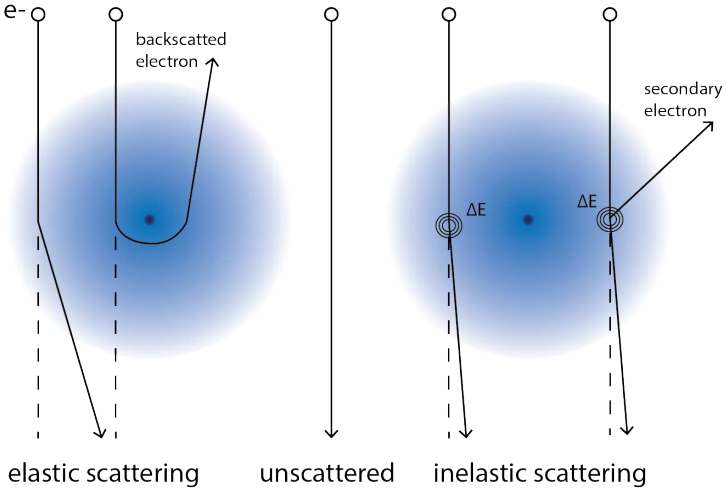

Figure 1.4.1: Examples for electron - specimen interaction. Elastic scattering with the electrostatic potiential of the nucleus (blue) of an atom leads to a scattering angle, which depends on the nucleus-electron distance (left). If the distance is too large, no interaction occurs (middle). Inelastic scattering results in energy deposition in the specimen, which can result in secondary electrons (right).

interband excitation as well as collective oscillations (plasmons) and (2) ionisation of electrons in the inner electronic shells. Ionisation leads to so-called 'secondary electrons' [Reimer and Kohl, 2008], which are emitted in a random direction.

The **cross-section** σ reflects the probability for scattering of an incoming particle, here the electron of a certain energy, by a scattering potential. In the case of several scattering potentials, e.g. the atoms in a specimen, the average distance between two scattering events , the '**mean-free path**' Λ, can be calculated from the cross-section as $\Lambda = 1/\sigma$. If elastic and inelastic scattering occurs, the respective cross-sections σ_{el} and σ_{inel} add up to the total cross-section σ_{tot}. Therefore, the mean-free-path of the electrons in the specimen can be calculated as [Williams and Carter, 2009]:

$$\begin{aligned} \Lambda_{tot} &= \frac{1}{\sigma_{tot}} = \frac{1}{\sigma_{el} + \sigma_{inel}} \\ &= (\frac{1}{\Lambda_{el}} + \frac{1}{\Lambda_{inel}})^{-1} \end{aligned} \tag{1.1}$$

The ratio between inelastic and elastic scattering was estimated to be 3:1 for cryo-EM on biological samples [Dubochet et al., 1988; Henderson, 1992]. Consequently, the thickness of an EM sample is limited by the inelastic mean-free path Λ_{inel}. For typical cryo-EM conditions Λ_{inel} is approximately 200 nm [Grimm et al., 1996]. For samples of purified protein complexes in solution (section 1.4.2) the sample thickness is normally well below this value.

1.4.2 Electron microscopy

There are two different types of EM methods. In a scanning electron microscope (SEM) the surface of objects is studied by detecting backscattered and secondary electrons [Goldstein et al., 2003]. In a transmission electron microscope (TEM) electrons, which have passed through the object, are detected [Frank, 2006]. In comparison to SEM, the resolution that can be achieved by TEM is approximately one order of magnitude higher [Reimer and Kohl, 2008].

TEM imaging of biological samples requires fixation. Rapid freezing (described below) embeds the sample in non-crystalline ice in its hydrated state and is therefore the preferred method of fixation. TEM measurements of these samples are referred to as cryo-electron microscopy (cryo-EM). Among TEM methods, there are three that allow the determination of three-dimensional (3D) structures of the sample under investigation: electron crystallography, tomography and single particle analysis (SPA) [Baumeister and Steven, 2000; Engelhard, 2006].

In electron crystallography, electrons are scattered by two-dimensional (2D) crystals formed by a layer of periodically arranged proteins. Scattering patterns at different tilt angles of the crystal can be used for 3D structure determination (see [Glaeser, 1999; Engelhard, 2006] for details).

In tomography, TEM images of the sample are acquired at multiple tilt angles. From these images and the tilt angle information, the corresponding 3D volume can be computed. Under cryo conditions (cryo-electron tomography, CET), a 3D structure of the sample, e.g. vesicles or entire cells, can be obtained under native conditions (reviewed in [Baumeister et al., 1999; Förster et al., 2012]).

For the single-particle approach, a purified sample in solution is visualised in TEM images at a tilt angle of 0°. These images include projections of different copies of the molecule of interest from different angles. From the projections a 3D structure can be computed [Frank, 2006] (subsection 1.4.4). In this work, cryo-EM data were used for SPA, referred to as single particle cryo-EM (SP cryo-EM).

Sample preparation for cryo-electron microscopy

In order to use the TEM technology for studies of biological samples, several challenges have to be met. In contrast to inorganic samples studied in material science, biological samples are sensitive to damage by the electron beam through inelastic scattering (radiation- or beam damage). Additionally, due to their soft nature and to avoid evaporation in the vacuum of the microscope column, they have to be fixed on a grid, which is used as a microscope slide. Therefore, TEM imaging requires

careful preparation of the biological sample [Engelhard, 2006; Frank, 2006].

Cryogenic ('cryo') sample preparation preserves the sample in a close-to-native state and meets the challenges mentioned above. In the first step of this method, the sample is pipetted onto the grid, typically a copper grid covered by a carbon film with holes. This grid is then rapidly frozen by plunging it into a cryogen, such as liquid ethane, cooled by liquid nitrogen to a temperature of ~ -180 °C ('plunge freezing'). The high cooling rate of $\sim 100,000$ °Cs^{-1} during plunging transforms the water molecules into a vitreous ice state, preventing the formation of crystalline ice. Thereby, the density of the water remains constant, leaving the sample components intact and in a close-to-native state. The frozen sample on the grid is then transferred into a TEM (see next paragraph), where it is cooled to ~ -180 °C throughout the cryo-EM data acquisition (see [Engelhard, 2006]).

Plunge freezing is applicable to thin samples, such as purified proteins in solution, used in this work. For thicker samples, the cooling-rate of this method is too low, but vitrification can be achieved by high-pressure freezing [Müller-Reichert et al., 2003; O'Toole, 2010]. As the mean-free path of electrons in matter (Equation 1.1) limits the sample thickness suitable for TEM measurements to ~200 nm (see subsection 1.4.1), thinning of the thicker vitrified samples might be required for cryo-EM data acquisition, e.g. by focused ion beam (FIB) milling [Rigort et al., 2012].

In the vitreous state, the sample is fixed on the grid and prevented from evaporation inside the microscope. However, beam damage does occur, accumulates and becomes significant for total dose values above ~ 20 e$Å^{-2}$ [Baker and Rubinstein, 2010], limiting the signal-to-noise ratio (SNR) and thereby the resolution. The beam damage most significantly affects the high-resolution signal. With increasing dose, the degradation of signal progresses towards the lower-resolution regime, while the contrast for the unaffected spatial frequencies increases. Therefore, the total dose used for imaging has to be chosen depending on the required resolution.

The transmission electron microscope

The overall composition of a TEM (Figure 1.4.2) is similar to that of a light microscope. However, electrons probe the sample instead of photons. The source of the electron beam used for high-resolution imaging is a field emission gun (FEG), providing a beam of highly coherent electrons [Förster et al., 2012]. To avoid interactions of the electron beam with gas atoms, which would lead to noise in the image, the whole microscope column is kept in high vacuum conditions (usually

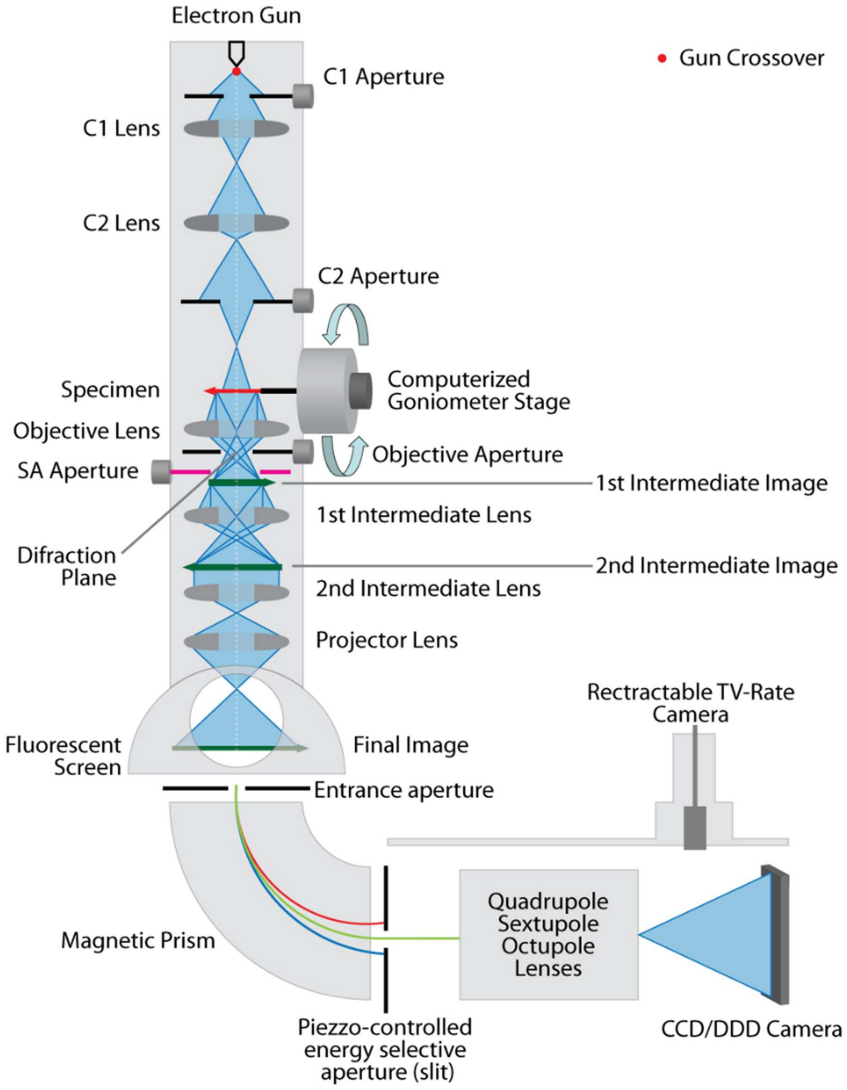

Figure 1.4.2: Composition of a transmission electron microscope. Figure taken from [Asano, 2015].

$\sim 10^{-10}$ bar) [Williams and Carter, 2009].

Electromagnetic lenses and apertures allow manipulation of the beam. The condenser lenses C1 and C2 (in the Titan Krios (FEI), used for this work, there is an additional lens C3) and the corresponding apertures ideally provide parallel illumination of the sample on the grid stage. Traversing the sample, the illuminating electrons either pass through without any interaction or get scattered (see subsection 1.4.1). The beam of scattered and unscattered electrons then passes the objective lens, which creates the first projection image. The objective aperture filters out electrons scattered at high angles, which do not contribute to the signal of the sample, followed by two additional lenses, which enlarge the projection further, leading to the final image ([Williams and Carter, 2009; Reimer and Kohl, 2008]).

With increasing sample thickness the percentage of inelastically scattered electrons increases (see subsection 1.4.1). Due to the strong chromatic aberration of the electromagnetic lenses (see section 1.4.3), inelastically scattered electrons do not add to the signal in the image. Therefore, energy filters can improve the image quality by removing electrons that have lost energy from the final projection ('Zero-loss filtering') [Krivanek et al., 1995]. However, for cryo-EM on purified proteins energy filtering is not necessary and was not used in this study.

The final image is recorded by a photographic film or a digital detector. Until recently, digital detectors were charge-coupled device (CCD) based cameras, which first convert an incoming electron into a photon, subsequently detected. The novel direct electron detectors (DEDs) can detect electrons directly through a semiconductor membrane (reviewed in [Booth and Mooney, 2013]).

Direct electron detectors

The direct detection of electrons leads to an improved detective quantum efficiency (DQE) in particular for the high spatial frequencies (high-resolution information) [Ruskin et al., 2013; McMullan et al., 2014]. This results in a dramatically improved SNR. An additional advantage of DEDs is their fast data readout, which allows to record several subframes for each image. Alignment of these frames can correct for drift and weighting them according to the dose accumulating over time can reduce effects of beam damage. Both may improve the data quality further (reviewed in [Bai et al., 2014]). The data for this work were acquired with the FalconII and FalconIII DEDs [Kuijper et al., 2015]. The Gatan K2 detector, a different type of DED, and the FalconIII detector can additionally operate in a 'counting mode' to localise incoming electrons more precisely and suppress electronic noise (as described in [Booth and Mooney, 2013]).

1.4.3 Physical basics of the image formation process

Theoretical resolution

In microscopy, the resolving power of an instrument (d) is defined as the minimal distance between two points, which can be visualised separately. Generally, the resolving power is limited by diffraction and can be calculated according to the Rayleigh-criterion as [Williams and Carter, 2009]:

$$d = \frac{0.61 \cdot \lambda}{\alpha} \tag{1.2}$$

from the angular aperture α of the instrument and the wavelength λ used for imaging. Therefore, the resolution in microscopy is generally limited by the wavelength. For particles with a mass m with a momentum p the wavelength is given through the deBroglie equation (Equation 1.3). High-energy electrons used in TEM have an energy of typically 100-300 keV and relativistic effects have to be taken into account, leading to a wavelength as given in Equation 1.4 [Williams and Carter, 2009].

$$\lambda = \frac{h}{p} = \frac{h}{m \cdot v} \tag{1.3}$$

$$\lambda = h \cdot c \frac{1}{\sqrt{2E_0 \cdot E + E^2}} \tag{1.4}$$

with the Planck constant h, the velocity v, the speed of light c, the rest energy $E_0 = m_0 c$ and the kinetic energy E. Electrons with a kinetic energy of 300 keV, used for the imaging in this study, have a corresponding wavelength of ∼0.02 Å, which is much smaller then that of visible light (400-700 nm) or X-rays used for structural studies (∼1 Å) [Förster et al., 2012]. However, the resolution obtained in TEM is further limited by several factors discussed in the following paragraphs.

Aberrations - resolution limitation by lenses

Aberrations are caused by imperfections of lenses. The most performance limiting aberrations in TEM are spherical aberration, chromatic aberration and astigmatism [Williams and Carter, 2009].

Spherical aberration is caused by differences in the refraction of a lens depending on the distance to the optical axis. Rays passing the electromagnetic lens towards the outside are bent more strongly than those passing close to the optical axis. Therefore, the rays are not focused in one point. In the image plane this leads to a disk with a radius r_{sa}, which depends on the spherical-aberration coefficient C_s, specific for a lens/lens system ($C_s \sim 2.7$ for the Titan Krios), and the angular aperture α [Williams and Carter, 2009]:

$$r_{sa} = C_s \alpha^3 \tag{1.5}$$

The spherical aberration limits the resolution to $r_{min} = 0.91 \cdot (C_s \lambda^3)^{\frac{1}{4}}$, which is normally in the order of 2-3 Å for standard TEMs and between 0.7-1.5 Å for high-resolution instruments [Williams and Carter, 2009].

Chromatic aberration also leads to different focus planes. However, this artefact is caused by the dependence of the lens refraction on the wavelength of the

electrons. Electrons with lower energy are refracted more strongly than those with higher energy. Although a highly monochromatic electron source is used in TEM, this effect is still important as electrons may lose energy through inelastic scattering by the specimen (subsection 1.4.1). Due to chromatic aberration, a point of an object is projected as a disk with a radius r_{ca} in the image plane [Williams and Carter, 2009]:

$$r_{ca} = C_c \frac{\Delta E}{E_0} \alpha \tag{1.6}$$

with the chromatic-aberration coefficient C_c, the angular aperture α and the energy loss ΔE with respect to the energy of the electrons in the initial beam E_0. The resolution limitation caused by chromatic aberration strongly depends on the sample thickness, as inelastic scattering and thereby ΔE increases with the thickness of the specimen.

Astigmatism is caused by a non-symmetrical magnetic field in the electromagnetic lenses of a TEM, leading to differences in refraction depending on the angle between the electron beam and the optical axis (for details see [Reimer and Kohl, 2008]). This aberration can be compensated by so-called stigmators and does not limit the resolution when corrected [Williams and Carter, 2009].

Comatic aberration (coma) results from asymmetric passage through a lens. In EM this aberration appears if the rotation centre is not aligned correctly. When aiming for high-resolution structural information coma may become a resolution limiting aberration [Reimer and Kohl, 2008] and needs to be corrected by a coma-free alignment prior to data acquisition [Williams and Carter, 2009].

Resolution limitation by digital cameras

Projection images are usually recorded using digital cameras with a finite pixel size. In order to distinguish two features in an image, they have to be projected onto two pixels that are separated by at least one pixel. Therefore, the accessible resolution is limited to two times the image pixel size ('sampling theorem', [Frank, 2006]). The corresponding spatial frequency (after Fourier transformation of the image) is commonly referred to as the 'Nyquist frequency', beyond which no information is accessible. The cryo-EM data for the studies of this thesis were taken with a magnified pixel size of ∼1.4 Å (section 2.3), limiting the possible resolution to 2.8 Å. By using higher magnifications the effective pixel size on the specimen level can be decreased.

A second resolution-limiting property of the detector is the detective quantum efficiency (DQE). It reflects how much noise is added to a detected signal by the

camera itself [Ruskin et al., 2013]:

$$\mathrm{DQE(k)} = \frac{\mathrm{SSNR(k)_{out}}}{\mathrm{SSNR(k)_{in}}} \tag{1.7}$$

with the input and output spectral signal-to-noise ratios $\mathrm{SSNR(k)_{in}}$ and $\mathrm{SSNR(k)_{out}}$, respectively. The DQE depends on the spatial frequency k and decreases towards high frequencies due to the interaction of the electrons with the detector material. Therefore, with an increasing magnification the overall image quality improves, as a broader frequency range is not dampened by the DQE. From the resulting $\mathrm{SSNR(k)_{out}}$ the resolution on the raw image can be determined [Unser et al., 1987, 1989]. DEDs offer a better DQE than CCD cameras in particular for high spatial frequencies [Ruskin et al., 2013; McMullan et al., 2014], leading to higher $\mathrm{SSNR(k)_{out}}$ values and therefore a better resolution in the raw images.

Contrast formation in cryo-EM images

In TEM, the electrons from the incoming beam interact with the specimen through elastic and inelastic scattering (subsection 1.4.1). The contrast in cryo-EM images is mainly formed by elastically scattered electrons, whereas inelastically scattered electrons mostly contribute to noise, in particular in the higher-resolution range [Henderson, 1992]. Therefore, inelastic scattering is unwanted for high-resolution structure determination. For purified protein complexes in solution the sample thickness is normally below the mean free path of inelastic scattering (section 1.4.2 and subsection 1.4.1). Due to this small sample thickness it can also be assumed that each electron is scattered no more than once ('kinematic approximation').

Contrast C in an image can be defined as the difference in intensity ΔI between two neighbouring areas showing the intensities I_1 and I_2 [Williams and Carter, 2009]:

$$C = \frac{I_2 - I_1}{I_1} = \frac{\Delta I}{I_1} \tag{1.8}$$

There are two main contrast formation mechanisms in EM images: phase contrast and amplitude contrast. Scattering as presented in subsection 1.4.1 treats electrons as particles. In an alternative approach, an incoming electron is described by a wave function, which undergoes a phase shift upon scattering. In order to understand contrast formation by electron scattering in a biological specimen, the wave-function approach is particularly useful as described in the following.

Phase contrast results from the interference of the elastically scattered and unscattered electron waves in the image plane. Scattering of an electron, travelling

along the z axis, at the 3D Coulomb Potential $V(x, y, z)$ of the specimen induces a phase shift $\Phi(x, y)$ [Frank, 2006]:

$$\Phi(x, y) = \Phi(\mathbf{r}) = \int V(x, y, z)dz \tag{1.9}$$

which modifies the incoming wave $\Psi_0 = \exp\left(i\frac{2\pi}{\lambda}z\right)$ as [Frank, 2006]:

$$\Psi_{sc}(\mathbf{r}) = \Psi_0 \exp(i\Phi(\mathbf{r})) \tag{1.10}$$

Due to the low atomic numbers Z of the atoms in biological samples the phase shift Φ will be small: $\Phi \ll 1$ ('weak phase approximation', WPA). Therefore, we can approximate the scattered wave Ψ_{sc} by the first two terms of a Taylor expansion of Equation 1.10:

$$\Psi_{sc}(\mathbf{r}) = \Psi_0\left[1 + i\Phi(\mathbf{r})\right] \tag{1.11}$$

In this approximation the scattered wave can be considered as a sum of the incoming wave and a scattered wave with a small amplitude $\Phi(\mathbf{r})$, with a phase shift of $\frac{\pi}{2}$ [Frank, 2006; Reimer and Kohl, 2008]. Figure 1.4.3 A illustrates that, in this scenario, the resulting intensity $I = |\Psi_{sc}|^2$ is dominated by the incoming wave Ψ_0. Therefore, the small $\Phi(\mathbf{r})$ of weak phase objects is not sufficient for contrast forma-

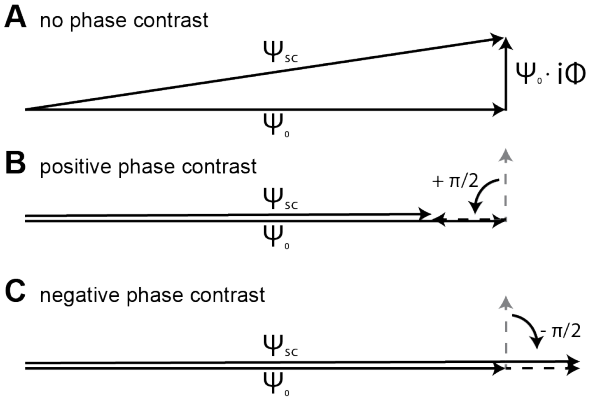

Figure 1.4.3: Phase contrast for weak phase objects. (A) Without any additional phase shift, no contrast is formed by the scattered wave. (B&C) If an additional phase shift of $\pm\frac{\pi}{2}$ is induced, a positive (B) or negative (C) phase contrast occurs. Figure adapted from [Reimer and Kohl, 2008].

tion. However, in TEM the lens aberrations and defocusing of the image induce an additional phase shift γ. Neglecting effects of astigmatism, γ can be determined by the so-called Scherzer formula [Frank, 2006; Reimer and Kohl, 2008]:

$$\gamma(k) = \frac{\pi}{2}\left(C_s\lambda^3k^4 - 2\Delta z\lambda k^2\right) \tag{1.12}$$

Therefore, γ is influenced by the spherical aberration constant C_s (Equation 1.5), the defocus Δz and the wave length λ and is a function of the spatial frequency of the

wave after scattering $k = |\mathbf{k}| = |(k_x, k_y)| = \theta/\lambda$, with the scattering angle θ. The contrast is maximal for an additional phase shift γ of $\pm\frac{\pi}{2}$ [Reimer and Kohl, 2008], leading to positive or negative phase contrast (see Figure 1.4.3 B&C).

In the back-focal plane the wave function is then described by the Fourier transform of Ψ_{sc} and the additionally induced phase shift γ [Frank, 2006]:

$$\Psi_{bf}(\mathbf{k}) = \mathcal{F}\{\Psi_{sc}(\mathbf{r})\}\exp(i\gamma(\mathbf{k})) \tag{1.13}$$

To obtain the wave function in the image plane $\Psi_i(\mathbf{r})$, an inverse Fourier transform ($\mathcal{F}^{-1}$) is applied under consideration of the aperture $A(\mathbf{k})$ (see Figure 1.4.2), which limits the spatial frequencies that can pass to k_{max} [Frank, 2006].

$$\Psi_i(\mathbf{r}) = \mathcal{F}^{-1}\{\mathcal{F}\{\Psi_{sc}(\mathbf{r})\}A(\mathbf{k})\exp(i\gamma(\mathbf{k}))\} \tag{1.14}$$

$$A(\mathbf{k}) = \begin{cases} 1 & \text{if } |k| \leq k_{max} \\ 0 & \text{if } |k| > k_{max} \end{cases} \tag{1.15}$$

The image detected is the intensity I resulting from $\Psi_i(\mathbf{r})$ and it can be shown that within the WPA the intensity, i.e. the contrast, is linearly related to the object's Coulomb potential [Frank, 2006]:

$$I(\mathbf{r}) = |\Psi_i(\mathbf{r})|^2 \tag{1.16}$$

$$I(\mathbf{r}) \propto V(\mathbf{r}) \tag{1.17}$$

Amplitude contrast results from electron absorption by either the aperture, after elastic scattering to large angles (also referred to as 'scattering contrast' [Reimer and Kohl, 2008]) or the specimen during an inelastic scattering event [Frank, 2006]. This leads to darker areas in the image, i.e. lower intensity. The amplitude contrast can be integrated into the wave function of the scattered wave (Equation 1.10) by an imaginary component of the scattering potential Φ [Frank, 2006; Reimer and Kohl, 2008].

The influence of this contrast forming mechanism increases with specimen thickness (increasing inelastic scattering) and the atomic number of the specimen's atoms (larger elastic scattering angles) (see subsection 1.4.1). In cryo-EM, the amplitude contrast contributes to ~7% of the contrast in the image [Toyoshima and Unwin, 1988] and therefore constitutes a minor influence on the contrast formation dominated by the phase contrast.

Contrast transfer function

As already seen in Equation 1.12 and Equation 1.14 the image is influenced by the microscope parameters. In real space the imaging properties of the microscope are described by the point spread function (PSF). The image is a convolution of the ideal projection of the object and the PSF. In Fourier space this transforms to a multiplication with the contrast transfer function (CTF), which is the Fourier transform of the PSF [Frank, 2006]. In general, the CTF has three contributing factors: the aperture function $A(k)$, the envelope function $E(\mathbf{k})$ and the aberration function $B(\mathbf{k})$ [Williams and Carter, 2009]:

$$\mathrm{CTF}(\mathbf{k}) = A(\mathbf{k}) \cdot E(\mathbf{k}) \cdot B(\mathbf{k}) \tag{1.18}$$

The aperture function $A(\mathbf{k})$ is given by Equation 1.15. The envelope term $E(\mathbf{k})$ is caused by partial spatial and temporal incoherence of the electrons and leads to damping of the CTF towards higher spatial frequencies [Frank, 2006; Williams and Carter, 2009; Förster et al., 2012]. Finally, the aberration function $B(\mathbf{k})$ depends on the spherical aberration, the astigmatism and the defocus, as given by γ (Equation 1.12 for negligible astigmatism). Under the approximation that the ratio of amplitude and phase contrast $Q(\mathbf{k})$ is identical for all atoms in the specimen and that it is constant over the spatial frequency range of interest Q_0, $B(\mathbf{k})$ is given by [Frank, 2006]:

$$B(\mathbf{k}) = \sin(\gamma(k)) - Q_0 \cos(\gamma(k)) \tag{1.19}$$

Thus, the CTF induces an oscillating function of the Fourier transform of the image and dampens it towards higher frequencies [Frank, 2006; Förster et al., 2012]. If the defocus and the parameters of the microscope, such as C_s and $A(\mathrm{k})$, are known, current image processing procedures can correct for the CTF (as done for this work, see section 2.4).

Modulation transfer function

An additional modulation of the detected signal is due to the camera itself, described by the modulation transfer function (MTF). In contrast to the CTF, the MTF can be measured directly using a sharp edge as an object [de Ruijter and Weiss, 1992]. The improvements of the DEDs involve a higher MTF [Ruskin et al., 2013; McMullan et al., 2014].

1.4.4 Single-particle analysis

For SPA, the protein or protein complex of interest is purified. After vitrification, multiple copies of this structure are fixed on the grid in varying orientations. Their projections ('particles') can be extracted from cryo-EM images (micrographs) and used to reconstruct the 3D structure of the protein of interest (reviewed in [Frank, 2009; Orlova and Saibil, 2011; Förster et al., 2012; Nogales and Scheres, 2015]). The electron dose, which can be used for imaging, is restricted due to the beam damage (section 1.4.2) leading to a very low SNR of the individual particles. Therefore, the projections of many ($\sim 50,000 - 500,000$) 'single' particles are used for the reconstruction to increase the signal and thereby the resolution of the resulting 3D structure. The name 'single-particle analysis' was chosen to distinguish this method from crystallography, where millions of particles contribute to one diffraction pattern used for structure determination. It should not be confused with 'single-molecule imaging', which denotes measurements on a single molecule [Förster et al., 2012].

3D reconstruction in SPA

The basis of 3D reconstruction from projection is the projection-slice theorem, illustrated in Figure 1.4.4. According to this theorem, the projection of an object in real

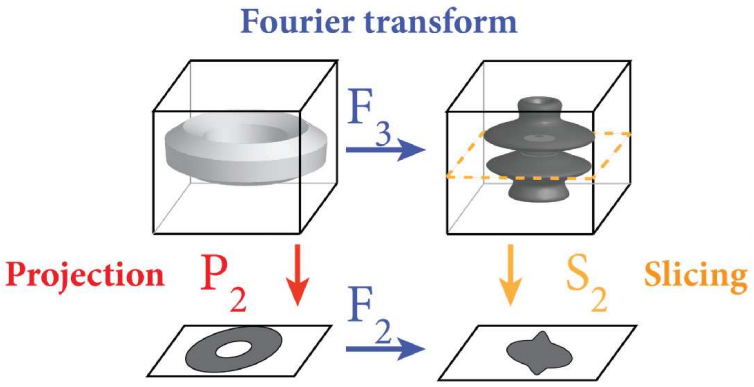

Figure 1.4.4: Illustration of the projection-slice theorem. The Fourier transform of the projection of a 3D volume in real space is identical with a central slice of the 3D Fourier transform of the volume. Figure adaped from [Asano, 2015].

space corresponds to a central slice in the corresponding direction in Fourier space (reviewed in [Förster et al., 2012; van Heel et al., 2000]. Assuming that projections are taken from all possible directions, the corresponding slices sample the Fourier space and give the structure factors of the investigated structure, from which the 3D volume can be reconstructed.

Therefore, to reconstruct a 3D volume, the projection directions and particle positions have to be determined for each projection. This alignment is an optimisation

problem. Five 'hidden parameters' have to be optimised for each particle: the three Euler angles, Φ, Ψ and Θ, describing the projection direction and in-plane rotation, as well as the x- and y-shifts [Frank, 2006; Sorzano et al., 2006; Sigworth et al., 2010]. There are several approaches to determine the orientation parameters [Orlova and Saibil, 2011], in SPA the most commonly used one is 'projection matching'.

Projection matching employs 'quasi expectation maximisation' or 'expectation maximisation' optimisation algorithms. Quasi expectation maximisation constitutes a least-square optimisation of, e.g., the cross correlation values for scoring the projection angles [Frank, 2006; Orlova and Saibil, 2011], whereas the classical expectation maximisation optimises a maximum likelihood (ML) or maximum a posteriori (MAP) function [Sigworth, 1998; Sigworth et al., 2010; Scheres, 2012b].

Both approaches iterate over two steps. In a first step, each experimental projection is compared with the projections of a reference at known angles, determining the maximum cross correlation values or the ML or MAP function ('angular-assignment' or 'expectation' step). Therefore, for the first iteration *a priori* knowledge of a volume, which can be used as an initial structure, is required. Possibilities for obtaining such an initial reference are reviewed in [Förster et al., 2012]. In the studies presented here, previously obtained structures of the 26S proteasome filtered to low resolution ($\sim$50 nm) serve as initial references.

In the second step of the procedure, a 3D volume is reconstructed from the experimental projections using the parameters determined in the first step ('maximisation' step). There is a variety of real-space and Fourier-space reconstruction algorithms (reviewed in [Sorzano et al., 2006; Frank, 2006; Orlova and Saibil, 2011; Förster et al., 2012]). All methods first average over the projections assigned to the same angular class, which gives one average for each angular view with an increased SNR. These angular class averages are than used for the respective reconstruction procedure leading to a 3D volume. The reconstruction resulting from the maximisation step is then used as the reference for the expectation step of the next iteration. Thereby, the steps are repeated until the optimisation converges, i.e. no significant change in the alignment parameters occurs [Frank, 2006; Förster et al., 2012].

All these implementations constitute a local optimisation around the initial volume and may converge to a local minimum. Therefore, the outcome may be biased by the input structure ('reference bias'). While the standard projection matching implementations (quasi expectation maximisation) converge faster, the statistical approaches (ML and MAP) are less prone to reference bias and overfitting [Sigworth, 1998; Scheres, 2012b].

Resolution of single-particle 3D reconstructions

As discussed in subsection 1.4.3, cryo-EM images do not reach the theoretically possible resolution. Among the limiting factors are the lens aberration, the electron detection mechanisms of cameras, drift during data acquisition and most significantly the low SNR (for more details see [Frank, 2006; Penczek, 2010]). Two aspects lead to the low SNR. Firstly, the beam-damage limits the applicable electron dose and thereby the SNR (section 1.4.2). The second limitation on the SNR is the low contrast of vitrified protein specimen due to the small difference in specific density between proteins and water, 1.3 g/cm^3 versus 1.0 g/cm^3, respectively [Engelhard, 2006]. The SNR can be improved by averaging aligned particles of the same angular class, as it is done in SPA. Therefore, the reconstructions yield a much higher SNR than a single-particle projection from a raw image, making the determination of high-resolution 3D structures possible [Engelhard, 2006; Orlova and Saibil, 2011].

The resolution of SPA reconstructions is commonly assessed by the Fourier shell correlation (FSC) [Van Heel, 1987; Penczek, 2010]:

$$\mathrm{FSC}_{12}(q_i) = \frac{\sum_{q \in q_i} F_1(q) \cdot F_2(q)^*}{\sqrt{\sum_{q \in q_i} F_1^2(q) \cdot \sum_{q \in q_i} F_2^2(q)}} \tag{1.20}$$

F_1 and F_2 are the Fourier transforms of two volumes, with the spatial frequency q. F_1 and F_2 are compared within shells q_i and the resolution is then determined by an FSC cutoff criterion. There are different rationals for choosing a cutoff criterion, also depending on the method of choosing the volumes for the FSC calculation (appendix of [Rosenthal and Henderson, 2003; Unser et al., 2005]).

One approach is to estimate the resolution q_r as the spatial frequency where the spectral SNR (SSNR) is 1 [Unser et al., 1987; Rosenthal and Henderson, 2003]. This corresponds to $\mathrm{FSC}(q_r) = 0.5$ for a 'pairwise FSC', for which reconstructions of two random half sets of aligned particles are subjected to the FSC analysis. However, when comparing the reconstruction under investigation with a simulated density from an available atomic model ('Fourier cross resolution', FCR) the $\mathrm{SNR} = 1$ criterion corresponds to $\mathrm{FCR}(q_r) = 0.71$ [Penczek, 2010].

Rosenthal and Henderson suggested that the $\mathrm{SNR} = 1$ criterion underestimates the resolution and showed that a cutoff at $\mathrm{FSC}(q_r) = 0.14$ can be an appropriate measure for the resolution [Rosenthal and Henderson, 2003]. This criterion is commonly applied, if the two volumes used for the FSC calculation have been obtained through the so-called 'gold-standard' procedure; i.e. the data is separated in two random half sets and is processed independently, resulting in two reconstructions,

which can be used for FSC calculation and are combined for the final result [Scheres, 2012a].

The improved DQE and MTF of DEDs (section 1.4.2) leads to significant improvements of the SNR in cryo-EM images, enabling the determination of 3D cryo-EM structures at atomic resolution, with 1.8 Å the highest resolution obtained so far [Bai et al., 2014; Merk et al., 2016].

However, such high resolution can only be obtained for very stable complexes. If a complex is present in multiple conformational states, as it is the case for the 26S proteasome (subsection 1.2.3), the resolution of 3D reconstructions is additionally limited by the flexibility, as different conformations may increase alignment errors and averaging over the different conformations during the reconstruction procedure leads to smearing out of the resulting density. 3D classification procedures may facilitate the separation of particles into different states, as discussed in the following.

Conformational heterogeneity and 3D classification

SPA is based on the assumption that the particles in the sample are structurally identical. This assumption is violated, if multiple conformations are present. However, it is generally possible to group particles *in-silico* with respect to their conformation, referred to as classification. Different algorithms are available for this task (reviewed in [Spahn and Penczek, 2009; Bai et al., 2014]).

Approaches to classify particles on the two dimensional (2D) image level have the shortcoming that different 2D classes might either reflect different conformations or different angular views [Spahn and Penczek, 2009]. Therefore, multiple conformations present in SP cryo-EM data are most commonly revealed by so-called 3D classification methods. The two main approaches for 3D classification employed by different software packages are the 3D principle component analysis (PCA) [Penczek et al., 2011] and the so-called 'multi-reference alignment' [Spahn and Penczek, 2009]. The latter was used for the data analysis in this thesis.

Multi-reference alignment can be seen as an extended version of projection matching, which compares the particles to more than one 3D volume [Spahn and Penczek, 2009; Scheres, 2010]. If the different conformations are known, these can be given as starting models ('supervised classification'). However, this is prone to reference bias. Therefore, 'unsupervised classification' gives more objective results [Spahn and Penczek, 2009]. For this procedure, the particles are aligned using one initial reference. Random subsets of the aligned particles are subsequently reconstructed

to serve as seeds for the multi-reference alignment. Like for projection matching procedures, particles can either be assigned by maximising the cross-correlation or by optimising the ML or MAP function [Scheres et al., 2007; Scheres, 2012b].

Multi-reference approaches are computationally costly, as the sampling space grows exponentially with the number of classes [Förster et al., 2012]. However, efforts have been made to reduce computational costs of multi-reference approaches and computational resources generally increase. In this context, the MAP multi-reference alignment implemented in RELION has become the state-of-the-art tool for 3D classification [Scheres, 2012a].

1.5 Aims of this work

The isolated 26S proteasome from yeast has been resolved in three distinct conformations to intermediate resolution (subsection 1.2.3). This work aims to decipher the structure of the 26S proteasome at a higher level of detail in two respects. Firstly, I studied the structural basis for the reciprocal regulation of the 26S proteasome and Ubp6, one of the major PIPs involved in the degradation process (subsection 1.3.1). Secondly, I aimed to improve the resolution of the 26S proteasome in the s1 state, allowing for accurate atomic model building. For both parts of the project my main focus was to develop and apply appropriate SPA image processing protocols that allow approaching these aims.

Towards a structural understanding of the 26S–Ubp6 complex, I asked the following questions: What is the overall structure of the holocomplex? Does the binding of Ubp6 and subsequent Ub-binding to Ubp6 induce conformational changes in the integral subunits of the 26S proteasome? To answer these questions different 3D classification approaches had to be combined and applied.

In the second part of this thesis, I contributed my expertise in image processing to a collaborative effort, aiming at high-resolution structure determination of the human 26S proteasome. The two main questions addressed in this project were: Can we obtain an SP cryo-EM reconstruction from heterogeneous, pseudo-symmetrical particles that is resolved to at least 4 Å, sufficient for atomic model building? What can we learn about proteasomal function from such a high-resolution structure? In this context, I established an image processing workflow based on the RELION software, tailored to the particularities of the 26S proteasome.

Along the lines of these aims the chapters of this thesis cover the following:

- chapter 2 describes the methods used for the sample preparation, characterisation, cryo-EM data acquisition and in particular the developed and applied processing workflows.
- chapter 3 presents the results on the 26S–Ubp6 complex and discusses them in the context of current literature.
- chapter 4 summarises and discusses the developed workflow and presents the insights obtained from the resulting high-resolution structure of the human 26S proteasome.
- chapter 5 contains overarching conclusions of this work and provides future perspectives.

2 Materials and methods

2.1 Protein expression and purification

2.1.1 Purification of the yeast 26S proteasome

Table 2.1.1: Materials for the purification of *S. cerevisiae* 26S proteasomes
Abbreviations: ATP: adenosinetriphosphate, DTT: dithiothreitol, CPh: creatine phosphate, CPK: creatine phosphatekinase, YPD: yeast extract peptone dextrose

strain	YYS40: MATa RPN11-3FLAG::HIS3 (in-house yeast strain library)
YPD medium	1% yeast extract (BD, New Jersey), 2% peptone (BD, New Jersey), 2% dextrose
lysis buffer	50 mM Tris-HCl pH 7.1, 100 mM NaCl, 10 mM $MgCl_2$, 4 mM ATP, 10% glycerol
sucrose collumn buffer	20 mM HEPES/ KOH pH 7.1, 40 mM NaCl, 10 mM $MgCl_2$, 5mM DTT, 4 mM ATP, 1 mM CPh, 3 units/ml CPK

Saccharomyces cerevisiae (*S. cerevisiae*) 26S proteasomes were purified using an established protocol [Sakata et al., 2011]. The yeast strain YYS40 was cultured in YPD medium for 5 days at 30 °C. After the cells had reached the stationary phase, they were harvested by centrifugation (4,000xg) and frozen at -80 °C for storage or immediately lysed. For lysis the cells were resuspended in 20 ml lysis buffer per 10 grams of cells and placed in a cell mill with 1 mm glass beads at 4 °C (milling 2 times for 3 min). After separation of the glass beads from the crude cell extract by centrifugation and washing of the glass beads with lysis buffer, the lysate was cleared by 2 centrifugation steps (SS34, 20 min, 20,000 rpm; Ti50.2, 45 min, 33,200 rpm). The affinity purification of 26S proteasomes via Rpn11-3FLAG from the cell lysate included an incubation with anti-FLAG M2 agarose beads (Sigma-Aldrich) for 2 hours at 4 °C, washing the agarose three times with lysis buffer in an gravity flow column and elution of 26S proteasomes three times with 1 column

volume of 400 μg/ml 3XFLAG peptide (Sigma-Aldrich). The eluted sample was concentrated in a 5 ml Amicon Ultra MWCO 10000 concentrator at 4 °C 4,000 g in 10 min intervals and subjected to a 15%- 40% sucrose gradient (buffer as given in subsection 2.1.1) for further isolation. Gradient fractions were analysed by sodium dodecyl sulfate polyacrylamide gel electrophoresis (SDS-PAGE) for the typical 26S proteasome band pattern and by an activity assay (as described in subsection 2.2.2 but using Suc-Leu-Leu-Val-Tyr-AMC as a substrate).

2.1.2 Purification of yeast Ubp6

Table 2.1.2: Materials for the purification of yeast GST-Ubp6

strain	BL21Star (DE3) (Invitrogen, Carlsbad)
GST binding buffer	10 mM PBS pH 7.4, 1 mM DTT
GST elution buffer	50 mM Tris-HCl pH 8.0, 20 mM reduced gluthation
MonoQ wash buffer	20 mM Tris-HCl pH 7.5
MonoQ elution buffer	20 mM Tris-HCl pH 7.5, 1 M NaCl

Yeast GST-Ubp6 (plasmid: pDL74 from Finley Lab, Harvard) was expressed in *Escherichia coli* (*E.coli*) and purified based on a protocol from [Leggett et al., 2002]. Cells were harvested by centrifugation and resuspended with GST binding buffer (6 ml buffer per 1 g cells). The cell suspension was incubated for 1 hour on ice with 1 mg/ml lysozyme, protease inhibitor without EDTA (Roche) and 0.5 mg/ml DNAse I (Roche), before the cells were finally lysed by sonication (30 s, 50%, Branson Sonifier 250). The crude cell extract was centrifuged (SS34, 20000 rpm, 30 min) and the resulting cleared cell extract was then incubated with 7 ml 4% Gluthation Agarose (Jens Bioscience) at 4 °C for 1 hour in batch mode. The cell-extract-agarose mix was poured in an empty gravity flow column, the flowthrough was collected and the Gluthation Agarose beads were washed 10 times with one column volume cold GST binding buffer. GST-Ubp6 was eluted with 5 times half the column volume cold GST elution buffer. The eluted protein was diluted with MonoQ wash buffer to a final volume of 45 ml for further purification by a 1 ml MonoQ column (GE Healthcare) using a standard purification protocol. Fractions were analysed by SDS-PAGE.

2.1.3 Purification of the human 26S proteasome

For purification of human 26S proteasomes, Andreas Schweitzer adapted an existing protocol [Liu et al., 2006]. The procedure is described in detail in [Schweitzer, 2016; Schweitzer et al., 2016]. In brief, 26S proteasomes were purified from erythrocytes by osmotic shock, ammonium sulfate precipitation, ultracentrifugation, and a sucrose gradient centrifugation. Gradient fractions were analysed by SDS-PAGE for the typical 26S proteasome band pattern and by an activity assay (as described in subsection 2.2.2 but using Suc-Leu- Leu-Val-Tyr-AMC as a substrate).

2.2 Sample characterisation

2.2.1 Pull-down experiments

To confirm the interaction between GST-Ubp6 (subsection 2.1.2) and the 26S proteasome (subsection 2.1.1) as well as GST-Ubp6 and ubiquitin aldehyde (UbAld, purchased from Boston Biochem), a pulldown assay was performed using the Rpn11-3XFlag tag and anti-FLAG M2 agarose beads (Sigma-Aldrich). 2.5 μM GST-Ubp6 were mixed with 110 nM 26S proteasomes in the absence and presence of 11 μM UbAld. All samples were incubated on ice for 30 min, before 20 μl of the 50% slurry of anti-FLAG M2 beads were added to the mixture, followed by another incubation of 30 min at 4 °C while being inverted on a rotating wheel. The M2 beads were washed three times with the lysis buffer (see Table 2.1.1) and eluted with 400 μg/ml FLAG peptide (Sigma-Aldrich). The resulting samples were subjected to SDS-PAGE analysis and the gels were analysed by Coomassie staining or immunoblotting.

2.2.2 Fluorogenic hydrolysis assays

Table 2.2.1: Materials for the fluorogenic hydrolysis assays

hydrolysis assay buffer	25mM HEPES/ KOH pH 8.0, 0.5 mM ATP, 125 mM K-acetate, 2.5 mM $MgCl_2$, 0.025% Triton X-100, 0.5 mM DTT, 0.1 mg/ml BSA

To verify the catalytic activity of the 26S proteasome-bound Ubp6 and the effects of UbAld [Peth et al., 2009], hydrolysis assays using fluorescent substrates

were carried out. The deubiquitylating activity of Ubp6 was monitored using Ub-AMC (ubiquitin-7-amido-4-methylcoumarin, Boston Biochem). Additionally, in separate samples the chymotrypsin-like activity of the CP of the 26S proteasome was assessed by GGL-AMC (glycine-glycine-leucine-7-amido-4-methylcoumarin, Bachem). The covalently attached ubiquitin or short peptide (GGL) quenches the fluorescence of the fluorophor AMC. Through the enymatic activity of Ubp6 or the CP, this quenching part of the substrate is cleaved off and free AMC starts to fluoresce. Hydrolysis of Ub-AMC or GGL-AMC by Ubp6 or the 20S, respectively, was measured at 360 nm excitation/465 nm light emission. Over time, free AMC accumulates. At the used concentrations, the substrates are cleaved at a constant rate, leading to a linearly increasing fluorescence intensity over time until the hydrolysis is hampered by e.g. the decreasing amount of substrate. The activity of the hydrolysing enzyme can be assessed as the intensity increase in the linear regime.

The experiments were carried out on a 384-well plate (Bachem). Up to 50 samples with differing compositions were prepared. For sample preparation, 3 μM GST-Ubp6 were added to 10 nM 26S proteasomes in the presence of the hydrolysis assay buffer, followed by an incubation for 15 min on ice. Then UbAld was added at different concentrations (0-15 μM) to the mixture, followed by further incubation for 15 min on ice. The enzymatic reaction was started by addition of 40 nM Ub-AMC or 40 nM GGL-AMC peptide. The fluorescence signal was taken for each sample approximately every 20 s using a GENios Pro (TECAN) fluorometer. To obtain the activity the linear regime of the fluorescence intensity I_F over time was determined by eye and fitted with a linear function $I_F = a \cdot x + b$, with a being the activity.

2.3 Electron microscopy

For SP cryo-EM sample preparation, Quantifoil R 2/1 holey carbon (Cu 200 mesh) grids (Quantifoil Micro Tools GmbH) were used. The human 26S proteasome sample was additionally prepared on Quantifoil Lacey Carbon grids (Cu 200 mesh). To obtain a vitrified sample, 4 μl of the sample (human 26S, or one of the samples listed in Table 3.1.2) were pipetted onto a glow-discharged grid and incubated for 20 s. The incubation was followed by manual blotting with filter paper and two washing steps with 4 μl of water to minimise the sucrose content. The sample was then vitrified by an in-house built 'plunger', which drops the sample into liquid ethane in a guillotine-like manner. The vitrified grids were stored in liquid nitrogen until

data acquisition.

All datasets analysed in this thesis were acquired on a Titan Krios transmission electron microscope (FEI) equipped with a DED. Images were recorded with the EPU software (FEI). Acquisition parameters and further information on the equipment are summarised in Table 2.3.1.

Table 2.3.1: Parameters and equipment used for data acquisitions

Parameter	datasets for project: 26S–Ubp6–UbAld	datasets for project: human 26S
microscope	Titan Krios (FEI)	Titan Krios (FEI)
detector	Falcon2 (FEI)	FEI Falcon3 (FEI)
energy of electron beam	300 keV	300 keV
pixelsize at specimen level	1.4 Å	1.35 Å
total dose	45 electrons/Å^2	45 electrons/Å^2
number of frames per image	7	~60
nominal defocus (underfocus)	2 to 3 μm	0.8 to 3 μm

2.4 Image processing

For all datasets, each image was acquired as a stack of frames (see Table 2.3.1), which were aligned with an in-house program based on the algorithm in reference [Li et al., 2013]. The aligned frame stacks as well as the summed images were saved for further use. Due to the different aims of the two projects included in this work, the SPA performed differs in many respects and will be discussed separately in the following two subsections.

Previous analysis has revealed that the conformational states of the two RPs of double-capped 26S proteasomes are not correlated [Beck et al., 2012; Matyskiela et al., 2013; Unverdorben et al., 2014]. Therefore, both data processing workflows include an *in-silico* separation of the RPs as described in [Unverdorben et al., 2014] as a key element, i.e., the two RPs of the double-capped 26S proteasomes were treated as separate virtual particles.

2.4.1 Data processing pipeline for the 26S–Ubp6–UbAld structure

For the 26S–Ubp6–UbAld project only the summed images of the aligned frame stacks were used. The CTF of each image was estimated and double-capped 26S

proteasome (dc26S) particles were automatically localised by cross-correlation analysis of template projections with the images as described in [Beck et al., 2012]. Both steps are implemented in the TOM toolbox [Nickell et al., 2005]. The localised particles were extracted with and without CTF-correction. For further processing in XMIPP, extraction with CTF correction was performed using the TOM toolbox. Additionally, particles were also extracted in RELION [Scheres, 2012a] without CTF-correction, because the algorithms used for alignment and classification in RELION correct for the CTF on-the-fly. Low-quality particles were identified using RELION 2D classification [Scheres, 2012a] and deleted from the dataset.

The remaining particles (Figure 2.4.1 A, setA) were subjected to 3D alignment and reconstruction (in XMIPP [Scheres et al., 2008]) with a full angular search imposing C2 symmetry. The obtained angles were then used for an *in-silico* separation of the RPs (Figure 2.4.1 A, setB). The idea of this *in-silico* separation is to duplicate each particle and to change the Euler angles of the copied particle from (`rot`,`tilt`,`psi`) to (`rot+180°`,`tilt`,`psi`).

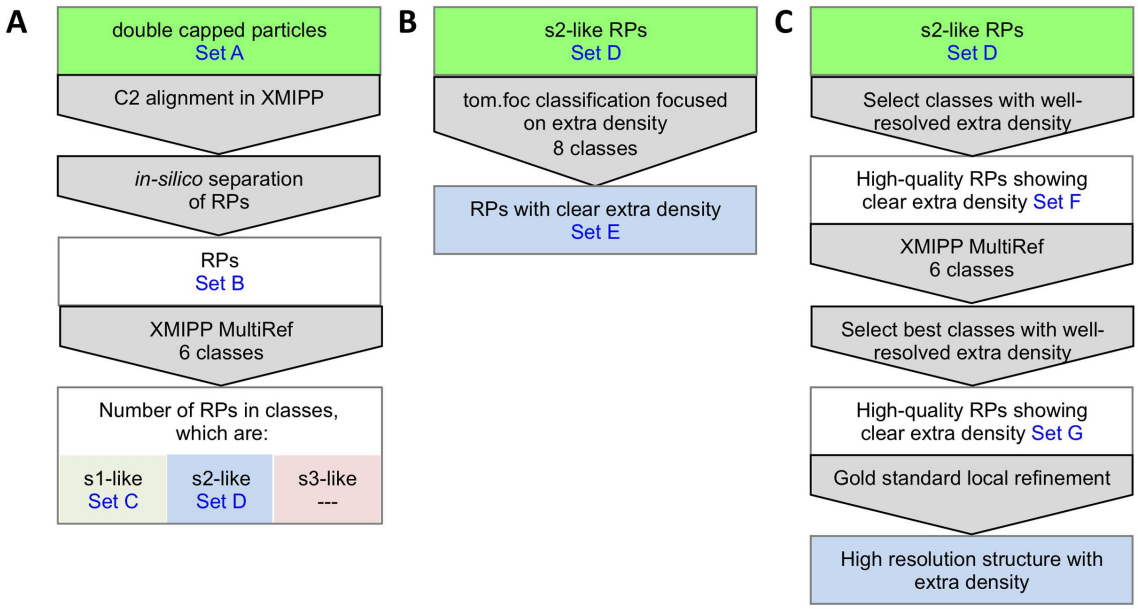

Figure 2.4.1: A: Workflow applied to all three datasets of the Ubp6 project, which aims to separate particles in different overall RP states. B: Focused classification with a mask on the region of the larger extra density observed for 26S–Ubp6–UbAld was applied to all datasets using tom.foc. C: Workflow applied to obtain a higher resolution structure of the 26S–Ubp6–UbAld complex.

These separated RPs were classified using an in-house modified version of XMIPP, which allows restricting the in-plane rotation and to focus the analysis on one of the RPs [Unverdorben et al., 2014]. For a comparison of the state occupancy, subsets of equal size (~180,000 particles) were classified into six classes. The resulting den-

sities were grouped by comparing them with the known conformations s1, s2 and s3 by cross-correlation (Figure 2.4.1 A, setC&D). For analysing the region of extra density the same classification approach was applied to all RPs of a dataset. The resulting s2-like particles (Figure 2.4.1 A, setD) were subjected to additional classification (Figure 2.4.1 B) as described in [Bohn et al., 2010] and implemented in the TOM toolbox with a small mask focused on the area between Rpn1 and Rpn10, where the larger part of the extra density in the reconstruction of 26S–Ubp6–UbAld is located. This analysis revealed small populations of classes showing the extra density in the 26S–Ubp6 and 26S–UbAld datasets (Figure 2.4.1 B, setE).

For a more detailed analysis of proteasome bound Ubp6–UbAld, the s2-like 26S–Ubp6–UbAld RPs (setD) were cleaned to achieve higher homogeneity by an additional round of classification employing the modified XMIPP version (Figure 2.4.1 C). Only particles from classes in an s2-like state with a clear extra density were kept. The resulting cleaned set of particles (setG) was subjected to a refinement of the alignment parameters in two independent halves ('gold-standard') as described in [Unverdorben et al., 2014]. The overall resolution of the final structure was calculated according to [Scheres, 2012a]. Additionally, the local resolution was assessed using Bsoft [Cardone et al., 2013] and the map was filtered accordingly.

2.4.2 Data processing pipeline for a high-resolution 26S structure

For processing of the human 26S proteasome dataset, the summed images of the aligned frame stacks were used for CTF estimation in CTFFIND4 [Rohou and Grigorieff, 2015]. From the fitted values, the image quality was assessed and images with a CTF fit score below 0.05 and a defocus outside the range of 0.8-3.5 μm were deleted. The remaining 40,211 images were subjected to automated particle localisation. The particle localisation and subsequent cleaning was done in the same way as for the datasets of the 26S–Ubp6 project described above (subsection 2.4.1). 2D classification in RELION was also used to divide the particles into single-capped and double-capped 26S proteasomes (sc26S and dc26S, respectively). Both subsets were extracted at full size (box size: 384x384 pixels, pixel size: 1.35 Å) and at a reduced size (box size: 256x256 pixels, pixel size: 2.03 Å). The size-reduced particles were preferably used for further processing steps except for the particle polishing and refinement (Figure 2.4.2). As mentioned above (subsection 2.4.1), no CTF correction was performed during particle extraction, as the RELION algorithms, used for subsequent steps of alignment and classification, correct for the CTF on-the-fly.

The dc26S and sc26S particles were processed separately until the final refine-

ment (for an overview on the processing see Figure 2.4.2). In the first step of processing the dc26S particles, an alignment and 3D reconstruction with imposed C2 symmetry was performed in RELION [Scheres, 2012a]. The result indicated an uneven angular distribution (Figure 4.1.1). This unbalanced distribution was used to decrease the size of the dataset. Angular classes with an above-average occupancy were reduced to the mean occupancy by discarding particles that score worst in terms of the 'rlnMaxValueProbDistribution' value, as calculated by RELION, which is a measure for the unambiguity of the (angular) class assignment of a particle. An evaluation did not show any significant decrease in resolution upon data reduction by this method (subsection 4.1.1). The alignment parameters of the remaining particles were refined imposing C2 symmetry using the gold-standard refinement procedure in RELION. Applying the refined parameters, the particles were polished in RELION, which includes a per frame shift alignment for each particle and a frequency-dependent dose weighting of the frames. The resulting summed particles are referred to as 'polished' or 'shiny' particles.

In the next step, the broken C2 symmetry was addressed by an *in-silico* separation of the RPs. To this end, the method used for the 26S–Ubp6 project (see subsection 2.4.1) and described in [Unverdorben et al., 2014] was implemented for the RELION data format. To maintain the separation of the RPs throughout the following steps, a mask has to be applied to one half of the 26S proteasome and any angular alignment has to be restricted to a local search around the angles used for the *in-silico* separation, this will be referred to as 'restricted alignment' in the following. The initial local search range for the restricted alignment was chosen as 7.5° and RELION decreases this range automatically depending on the resolution.

The separated and shiny RPs were subjected to classification in RELION, focused on one RP using a soft-edged spherical mask. As RELION applies this mask only to the 3D volume but not on the 2D particle level, particles may be misaligned to increase the density inside the masked area, leading to so-called 'moving target' artefacts, which include the classification according to different misalignments. Therefore, the alignment parameters were kept constant throughout the classification. The particles were classified in two rounds, keeping only those classes in a well-defined s1-like state. The resulting 'cleaned' RPs were then subjected to a refinement of the alignment parameters in RELION (gold-standard approach), with a restricted alignment and a soft-edged mask on one half of the 26S protesome.

For processing of the sc26S particles, C1- symmetry was imposed throughout all steps (Figure 2.4.2). After the initial alignment, the dataset was reduced as done for the dc26S particles, followed by refinement and particle polishing. The shiny par-

ticles were subjected to classification with a mask on the entire sc26S and a global angular search. The sc26S particles from s1-like classes were selected and refined onto the the final reconstruction of the dc26S RPs with a full angular search.

The classification of the sc26S particles also identified wrongly classified dc26S particles (dc26S*). These particles were reprocessed to obtain the high-quality RPs. A refinement imposing C2 symmetry was followed by a separation of the RPs, as done for the dc26S particles. A subsequent step of classification under the same conditions as done for the dc26S particles identified s1-like RPs, which were then refined with restricted alignment conditions onto the final reconstruction of the dc26S particles using a soft-edged mask on one half of the 26S protesome. These refined dc26S* RPs were then added to the dc26S RPs.

In the final step, the dc26S RPs and sc26S particles were merged and refined (Figure 2.4.2) under restricted alignment conditions using a soft-edged mask on one RP and the CP. The resolution of the resulting final reconstruction was assessed by Fourier shell correlation of the two gold-standard halfs in RELION [Scheres, 2012a]. This method includes an assessment and correction of a possible over-estimation of the resolution due to noise reinforcement and masking [Chen et al., 2013]. The local resolution of the map was computed using B-soft [Cardone et al., 2013].

2.5 Modelling of the high-resolution 26S structure

Based on the high-resolution density of the human 26S proteasome an atomic model was built. The procedure is described in detail in [Schweitzer et al., 2016] and follows the integrative modelling approach from [Goh et al., 2016]. In brief, an initial model was built from an existing crystal structure of the 20S and comparative models of the RP subunits using Modeller [Šali and Blundell, 1993] in combination with *de novo* prediction for missing or low-homology parts in Rosetta [Kaufmann et al., 2010; Leaver-Fay et al., 2011]. VMD [Humphrey et al., 1996; Stone et al., 2014] was employed to analyse the predicted models and select the best model, which was then fitted into the density using MDFF [Trabuco et al., 2008]. Segments of the model that deviated from the density were corrected through an interactive combination of a Monte Carlo backbone and side chain rotamer search algorithm (implemented in Rosetta) and MDFF (following an optimised strategy from [Lindert and McCammon, 2015]). The model was further refined in reciprocal space using PHENIX [Adams et al., 2002; Greber et al., 2014] and the result was analysed in COOT [Emsley et al., 2010].

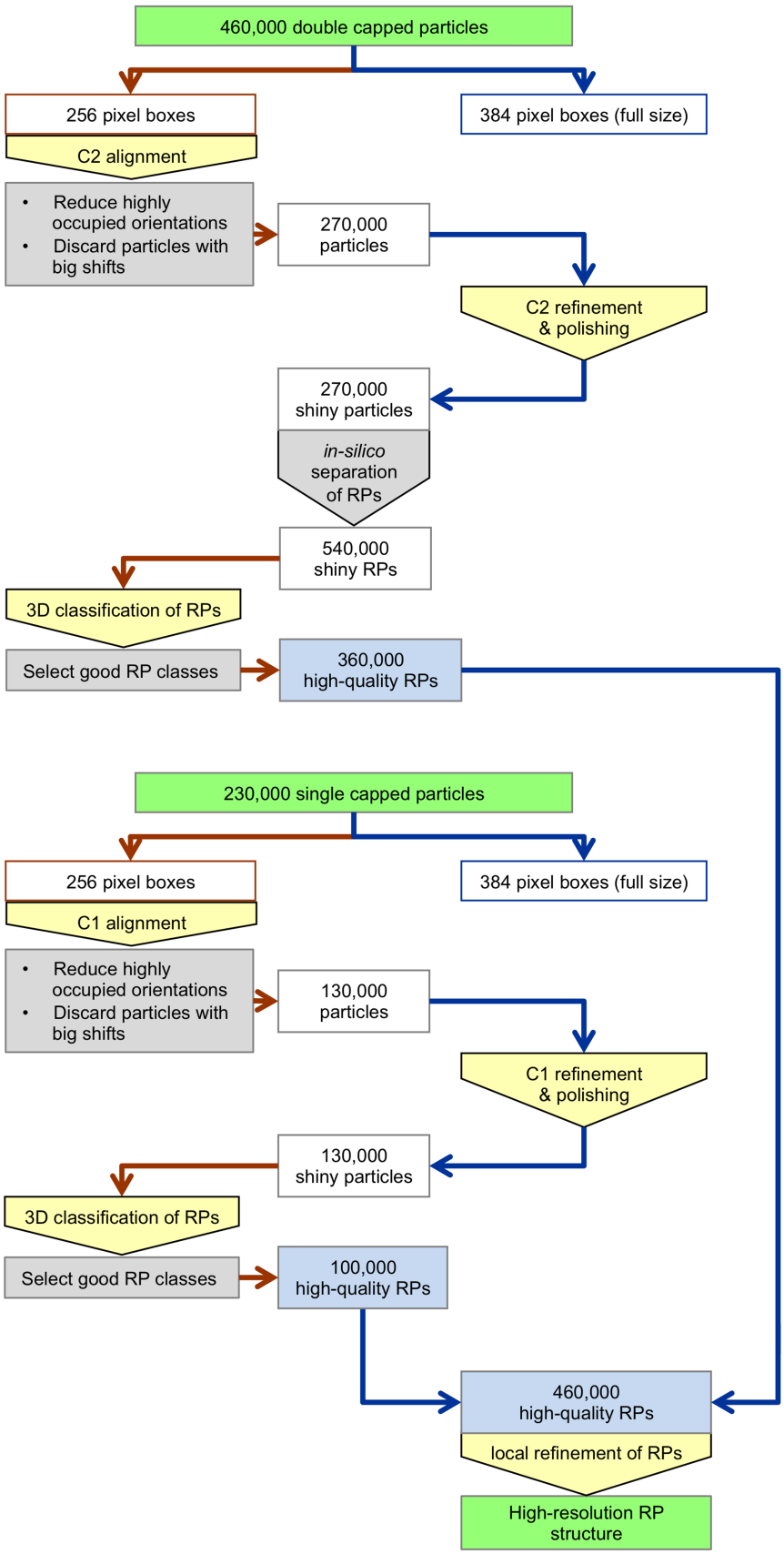

Figure 2.4.2: Workflow applied to double- and single-capped 26S proteasome particles to obtain a high resolution structure of the RP. Boxes in yellow represent steps conducted in RELION, boxes in grey stand for steps done outside of RELION using own tools.

3 Structure of the 26S proteasome in the presence of Ubp6 and ubiquitin aldehyde

Motivated by the results from Peth and colleagues [Peth et al., 2009] described in subsection 1.3.1, the structure of the 26S–Ubp6 complex was studied by cryo-EM in presence and absence of ubiquitin aldehyde. The work aimed to explore the arrangement of the complex as well as the effects of ubiquitin binding to it on a structural level. The results were published in the peer-reviewed article [Aufderheide et al., 2015a] and this chapter is based on this publication. The co-authors contributed as stated in the publication. In particular, some of the results presented below were obtained in cooperation with Eri Sakata, who carried out the pull-down experiments, Florian Beck, who supported me during fitting a crystal structure of Ubp6 into the obtained density and Florian Stengel, a collaborator, who performed the cross-linking mass spectrometry (XL-MS) experiments.

3.1 Results

3.1.1 Biochemical characterisation

Ubp6 has been shown to be present in substoichometric amounts in wild type (WT) 26S proteasome purifications from yeast [Sakata et al., 2011]. According to label-free mass spectrometry quantification the amount of Ubp6 in our samples is approximately 30% of the canonical RP subunits (Table 3.1.1). In order to achieve a higher occupancy of Ubp6, we added recombinant Ubp6 in excess amounts to purified 26S proteasomes (‘26S–Ubp6‘). In a second step, UbAld was added to the complex to study the effects of ubiquitin-binding (‘26S–Ubp6–UbAld‘).

Table 3.1.1: iBAC values determined by label-free mass spectrometry of the WT 26S sample. Comparison of the values obtained for major PIPs with the average iBAC value of the stoichiometric 26S subunits. The stoichiometry is calculated by the ratio of the respective PIP iBAC value and the averaged iBAC value of the stoichiometric subunits.

	iBAC	approximated stoichiometry [%]
average over all stoichiometric subunits	$1.86 \cdot 10^{10}$	100
Rpn13	$1.28 \cdot 10^{10}$	69
Ubp6	$5.74 \cdot 10^{9}$	31
Dsk2	$5.95 \cdot 10^{7}$	< 1
Rad23	$5.80 \cdot 10^{7}$	< 1

Characterisation of the binding of Ubp6 to the 26S and UbAld to 26S–Ubp6

Due to the activation of Ubp6 upon binding to the 26S proteasome(subsection 1.3.1), it is possible to study the binding kinetics through fluorogenic hydrolysis assays (subsection 2.2.2) using Ub-AMC as a substrate, which is cleaved by Ubp6. Using these assays we verified the catalytic activity of the recombinant Ubp6 in the presence of purified 26S proteasomes and determined a concentration of Ubp6 in the saturated binding regime suitable for further experiments to be 3 µM. Additionally, we confirmed that the catalytic activity of proteasome bound Ubp6 was fully inhibited by UbAld at a concentration of 12 µM indicating a near-stoichiometric binding of UbAld to Ubp6 (Figure 3.1.1 A). This concentration of UbAld was used for further experiments on the 26S–Ubp6–UbAld complex.

The binding of Ubp6 to the 26S proteasome in the presence and absence of UbAld was further confirmed by a pulldown analysis (Figure 3.1.2), carried out by Eri Sakata. The pulldown assay was performed against the Rpn11-3XFlag analysing the occupancy of Ubp6 by coomassie staining and immunoblotting (for details see subsection 2.2.1). Interestingly, the band of Ubp6 is slightly intensified under addition of UbAld, indicating a more stable binding of Ubp6 to the 26S proteasome under this condition.

Increased proteasomal activity of the 26S–Ubp6 complex in the presence of UbAld

Using the fluorogenic substrate GGL-AMC, which is hydrolysed by the 20S, we were able to qualitatively reproduce the increase of proteasomal activity upon bind-

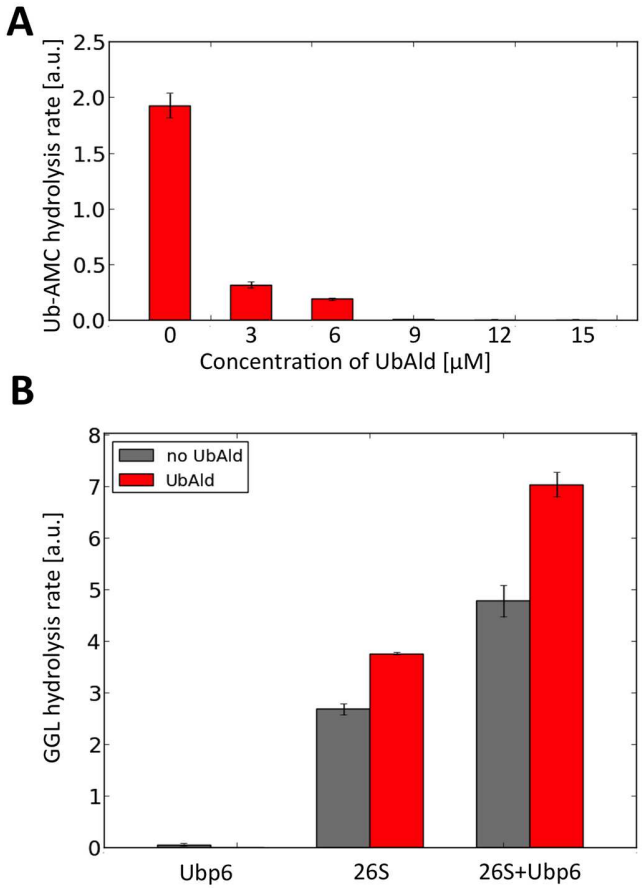

Figure 3.1.1: Catalytic activity of Ubp6 and the 20S: (A) Ub-AMC hydrolysis decreases with increasing concentration of UbAld. The activity of Ubp6 (3 µM) in the presence of WT 26S (10 nM) is completely inhibited by UbAld at concentrations above 9 µM. (B) Ubp6 (3 µM), WT 26S (10 nM), and WT 26S–Ubp6 (10 nM and 3 µM, respectively) were tested for the activity of the 20S CP in the absence (gray) and presence (red) of UbAld (15 µM). The GGL-AMC hydrolysis rates indicate an activation of WT 26S proteasomes in the presence of Ubp6 as well as UbAld and qualitatively reproduce the results from [Peth et al., 2009]. Figure adapted from [Aufderheide et al., 2015a].

ing of UbAld to 26S–Ubp6 reported by the Goldberg lab [Peth et al., 2009]. Interestingly, the detected GGL-AMC hydrolysis rates indicate an activation of 26S proteasomes (10 nM) in two steps (Figure 3.1.1 B). The first increase in hydrolysis by the 20S is encountered in the presence of recombinant Ubp6 (3 µM) and a second more significant increase is detected upon addition of UbAld (12 µM).

3.1.2 Single particle cryo-EM reconstructions

As discussed in subsection 3.1.1, Ubp6 is present in substoichometric amounts in purified WT 26S. Therefore, Ubp6 was not localised in previous cryo-EM studies of WT 26S. The biochemical characterisation of addition of recombinant Ubp6 (subsection 3.1.1) confirmed a higher occupancy of Ubp6 at the chosen concentrations of Ubp6 and UbAld, 3 µM and 12 µM, respectively. Thereby, we anticipated the localisation of Ubp6 in the holocomplex under these conditions. In order to obtain a sufficiently large amount of particles per image, WT 26S was used at a concentration of 300 nM for the cryo-EM experiments, implying that Ubp6 was added at 10-fold excess. The studied samples are summarised in Table 3.1.2.

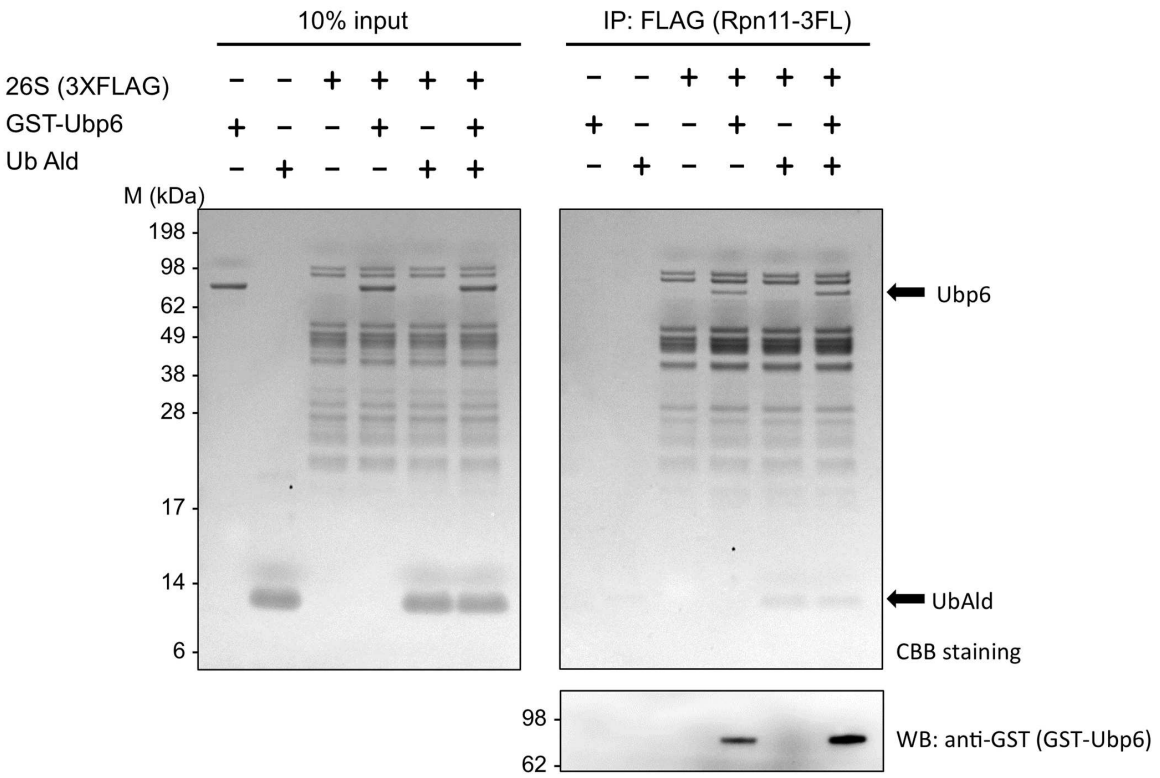

Figure 3.1.2: Purified GST-Ubp6 binds to the 26S proteasome: The pulldown assay was performed in the presence and absence of UbAld. The presence of UbAld slightly increases the interaction of Ubp6 with the 26S proteasome. Figure adapted from [Aufderheide et al., 2015a]

Table 3.1.2: Samples studied by cryo-EM

	26S–Ubp6	26S–Ubp6–UbAld	26S–UbAld
WT 26S [µM]	0.3	0.3	0.3
GST-Ubp6 [µM]	3	3	–
UbAld [µM]	–	12	12

Cryo-EM was performed as described in section 2.3 and the single-particle analysis was carried out as summarised in subsection 2.4.1. The main feature of the computational analysis is a separate treatment of the two RPs of the double-capped 26S proteasomes during the 3D alignment and classification procedures. Table 3.1.3 summarises the number of particles in each step of the analysis. The reconstruction from ∼160,000 26S–Ubp6 particles (each corresponding to a 26S proteasome half) yields a blurred RP density, which is typically observed for a mixture of multiple conformational states. In particular, the horseshoe-shaped scaffold assembled from the six PCI subunits is smeared out (Figure 3.1.3 B). Compared with the previously

published density of WT 26S proteasomes alone ('26S', Figure 3.1.3 A), no extra density could be detected upon addition of Ubp6. Thus, the overall blurriness of the RP in the 26S–Ubp6 reconstruction is the only detectable difference to the WT 26S dataset.

Table 3.1.3: Number of particles in the 26S–Ubp6 data analysis. The names Set A-G are as given in Figure 2.4.1.

Datasets	26S–Ubp6	26S–Ubp6–UbAld	26S–UbAld
Picked double capped particles (Set A)	81,100	84,100	250,600
Separated RPs (Set B)	162,200	168,200	501,200
s1-like RPs (Set C)	81,000	32,500	321,000
s2-like RPs (Set D)	81,200	135,800	180,200
s2-like RPs with extra density (Set E)	10,200	135,800	20,000
cleaning for high resolution structure:			
s2-like RPs with clear extra density (Set F)	–	107,700	–
s2-like RPs with clear extra density used for refinement (Set G)	–	52,900	–

In a second step, 15 uM of UbAld was added to study the structural consequences of ubiquitin binding to Ubp6 (26S–Ubp6–UbAld sample). Although the number of particles in the 26S–Ubp6–UbAld dataset ($\sim$ 170,000) is comparable to that of 26S–Ubp6, the reconstruction is better defined (Figure 3.1.3 C), indicative of less structural heterogeneity, and it differs notably from that of 26S alone. While the latter predominantly adopts the s1 conformation [Beck et al., 2012; Unverdorben et al., 2014], the overall structure of 26S–Ubp6–UbAld appears more similar to the s2 conformation [Unverdorben et al., 2014]. Most importantly, two extra densities in the direct vicinity of Rpn1 are clearly distinguishable. A smaller density is attached to Rpn1, while a larger density is in contact with Rpn1 as well as the ATPase OB-ring.

In the last step, the 26S–UbAld sample, we repeated the experiment without added Ubp6, to verify that these effects are due to the interaction of UbAld with Ubp6. The reconstruction from $\sim$500,000 particles also yielded a well-defined structure (Figure 3.1.3 D). In contrast to the 26S–Ubp6–UbAld map, it is highly similar to the reconstruction from 26S alone (Figure 3.1.3 A). Notably, the extra density of the 26S–Ubp6–UbAld reconstruction is not found in this reconstruction.

Taken together, these data strongly suggest that the extra density observed for 26S–Ubp6–UbAld can be attributed to Ubp6–UbAld. To further support this in-

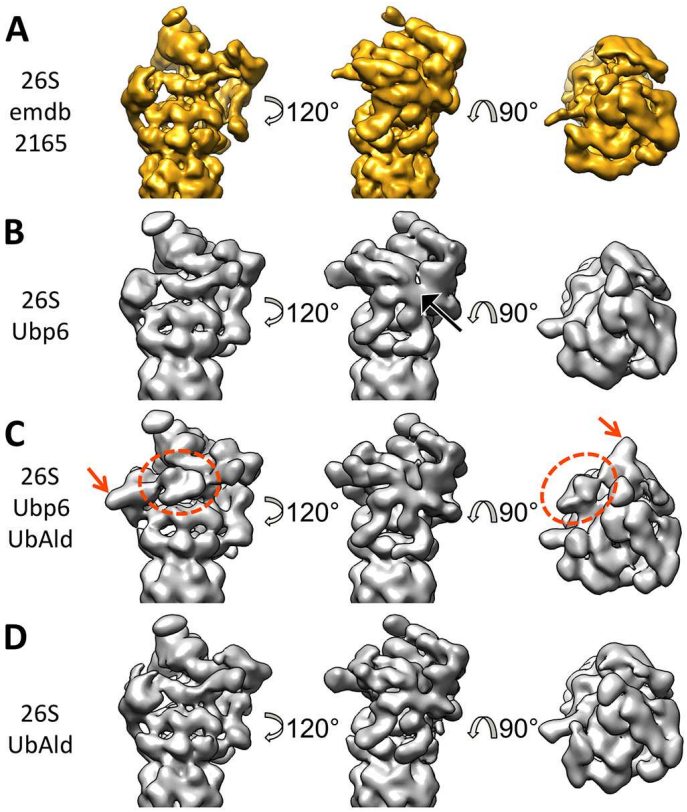

Figure 3.1.3: 26S proteasome reconstructions for different conditions. Reconstructions from datasets of (A) 26S, (B) 26S–Ubp6, (C) 26S–Ubp6–UbAld and (D) 26S–UbAld. All reconstructions were filtered to 15-Å resolution. While the reconstruction in A was taken from [Beck et al., 2012], datasets for B-D were acquired in this study. The black arrow in B indicates the blurred PCI horseshoe. The dotted orange ellipse and the orange arrow in C mark the extra density seen for the 26S–Ubp6–UbAld reconstruction. Figure adapted from [Aufderheide et al., 2015a].

terpretation, Florian Stengel, a collaborator from the University of Konstanz, performed XL-MS of 26S–Ubp6–UbAld. Overall, roughly 100 high-confidence crosslinks between different subunits of the 26S proteasome were identified, among them six involving Ubp6. Of those, three links were found between the ubiquitin-specific protease (USP) domain and the unstructured N-terminal region of Rpt2 as well as two links to the C-terminal part of Rpt1 (Table 3.1.4, [Aufderheide et al., 2015a]). Thus, essentially all detected crosslinks involving Ubp6 are in the immediate vicinity of the extra density, corroborating the findings from the cryo-EM reconstructions.

3.1.3 Analysis of conformational ensembles by classification

For a comparative analysis of the three datasets, subsets of equal size ($\sim$ 160,000 RPs) were subjected to 3D classification and divided into 6 classes (see subsection 2.4.1 for details). The class reconstructions were assigned to the known conformations s1, s2 and s3 [Unverdorben et al., 2014]. Different distributions of classes in the s1- and s2 states were observed in the datasets, whereas no classes were assigned to the s3 state (Figure 3.1.4). While the s1/s2 ratio of 26S–UbAld particles is comparable to that in 26S datasets (S1/S2=4:1) [Unverdorben et al., 2014], the other

Table 3.1.4: XL-MS intersubunit crosslinks involving Ubp6: AbsPos1 and AbsPos2 are the absolute positions of the cross-linked lysine residues within the UniProt (used uniprot sequences given in brackets) or construct sequence of Protein1 and Protein2, respectively. deltaS is a measure for how close the best assigned hit was scored with regard to the second best, Id is a weighted sum of different scores used to assess the quality of the composite MS2 spectrum as calculated by xQuest and FDR denotes the false-discovery rate as calculated by xProphet. All residues part of unstructured regions are coloured in light grey. Note: The residue numbers of GST_Ubp6 were chosen to have the first residue of Ubp6 numbered as 1 and residues of the GST-tag have negative values. Data published in [Aufderheide et al., 2015a].

Protein1	Protein2	AbsPos1	AbsPos2	deltaS	ld-Score	FDR
GST_Ubp6	Rpt2 (P40327)	177	20	0.6	31.57	0.045
GST_Ubp6	Rpt2 (P40327)	177	30	0.41	30.29	0.059
GST_Ubp6	Beta5 (P30656)	378	71	0.57	29.27	0.084
GST_Ubp6	Rpt1 (P33299)	375	394	0.63	28.52	0.112
GST_Ubp6	Rpt1 (P33299)	370	394	0.73	28.14	0.112
GST_Ubp6	Rpt1 (P33299)	378	394	0.38	27.07	0.126

two datasets with supplemented Ubp6 exhibit different state occupancies. For the 26S–Ubp6 dataset approximately equal amounts of particles are assigned to s1 and s2 (s1/s2=1:1). In contrast, the majority of proteasomes in the 26S–Ubp6–UbAld dataset are in an s2-like conformation (s1/s2=1:5). Overall, the different state occupancies of the three datasets are consistent with the respective reconstructions prior to classification (Figure 3.1.3). Thus, the binding of Ubp6 and additional UbAld to the 26S proteasome strongly increases the occupancy of the s2 state.

A striking property of the reconstructions from the s1 and s2-like particles is that the extra density (marked by orange ellipses and arrows in Figure 3.1.4), which is observed in the overall 26S–Ubp6–UbAld reconstruction, is exclusively present in the s2-like conformations. This feature is most clearly discernible in the reconstruction from the s2-like 26S–Ubp6–UbAld particles. In addition, the s2-like class reconstructions from the 26S–Ubp6 and 26S–UbAld datasets show indications of this extra density in the respective areas, whereas none of the s1-like groups exhibit any sign of it.

3.1.4 Focused classification results

To further investigate the relatively weak extra density in the s2-like states of the 26S–Ubp6 and 26S–UbAld datasets, the s2-like particles were classified out of the full datasets and subjected to a second round of classification focused on the region

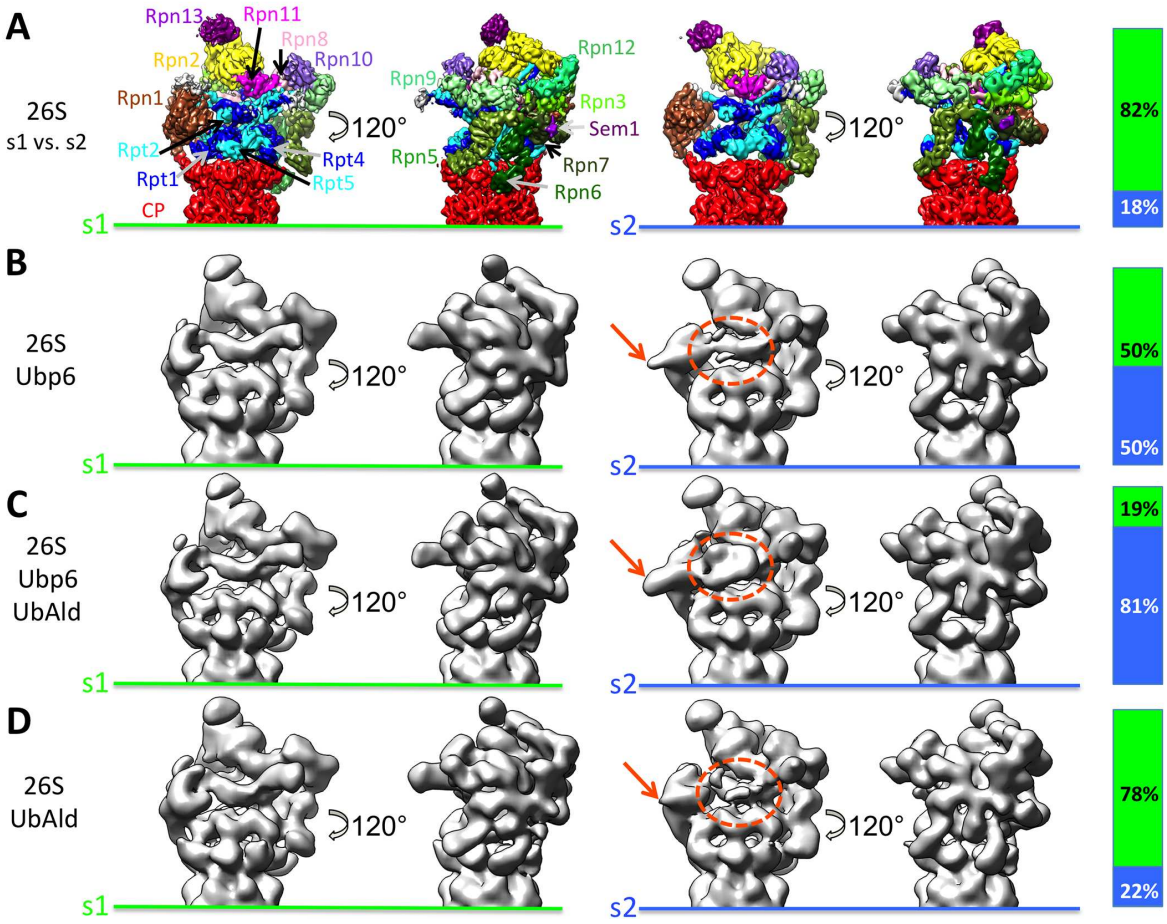

Figure 3.1.4: Classification of datasets into s1 and s2 states. The bars indicate the relative frequencies of s1 and s2 states. (A) The s1 and s2 reconstructions obtained from 26S proteasomes alone ([Unverdorben et al., 2014]. The different subunits of the regulatory particles are indicated for the s1 state. (B-D) As in A, for the 26S–Ubp6 (B), 26S–Ubp6–UbAld (C), and 26S–UbAld (D) datasets. The dotted orange ellipses and the orange arrows mark the extra density seen for the 26S–Ubp6–UbAld reconstruction shown in Figure 3.1.3 C. Figure adapted from [Aufderheide et al., 2015a].

between Rpn1 and Rpn10 as described in subsection 2.4.1 (Figure 2.4.1 B). As all classes from dataset 26S–Ubp6–UbAld from the first round of classification (Figure 2.4.1 A) showed extra density, no focused classification was needed for this dataset to extract the particles showing the extra density.

In contrast to previous classification results on the 26S alone [Unverdorben et al., 2014], for the 26S–Ubp6 dataset, 6% of all particles show an extra density, which is located at the same position as the one identified in the 26S–Ubp6–UbAld reconstruction, but which appears to be slightly smaller (Figure 3.1.5). Thus, Ubp6 alone can induce a similar conformation as seen with the 26S–Ubp6–UbAld dataset. However, as the population of this conformation is relatively small, it is most likely

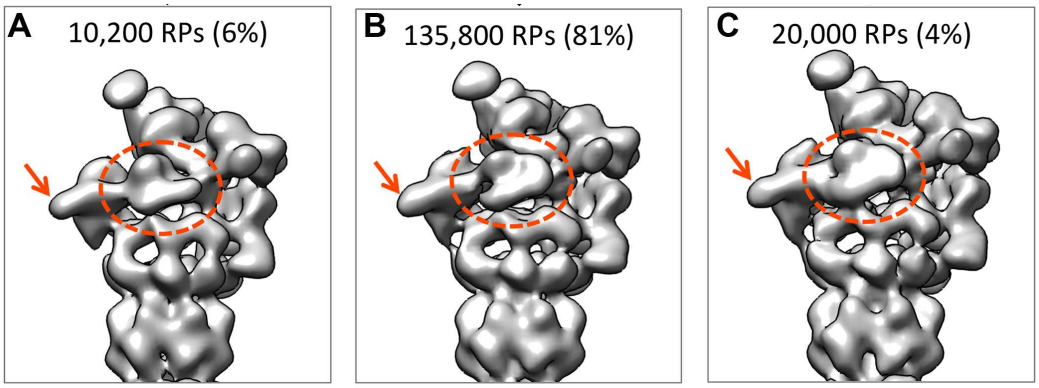

Figure 3.1.5: Focused classification result: Reconstructions of particles showing extra density in the s2-like state of the 26S–Ubp6 (A), 26S–Ubp6–UbAld (B), and 26S–UbAld (C) datasets and according RP numbers (see Table 3.1.3). Orange ellipses and arrows mark the extra densities in the final reconstructions of the classification results. Note the difference in the shape of the extra density in the 26S–Ubp6 reconstruction as compared with the other two. Figure adapted from [Aufderheide et al., 2015a].

one of many conformations adopted by the 26S–Ubp6 complex.

The analysis of the 26S–UbAld dataset also reveals an extra density for $\sim$ 4% of the particles. In contrast to 26S–Ubp6, this extra density has approximately the same size as seen for 26S–Ubp6–UbAld (Figure 3.1.5). The most likely explanation for this population is the binding of UbAld to the sub-stoichiometric amounts of endogenous Ubp6 present in purified 26S proteasome samples (Table 3.1.1). Due to the small percentage of particles exhibiting the extra density, it is likely that some of these particles are erroneously grouped during the multi-step classification procedure. Therefore, the given percentages of particles with this feature, most likely constitutes a lower boundary value.

The extra density-containing reconstructions from the 26S–Ubp6–UbAld and 26S–UbAld data are nearly identical, in particular there is no difference in the extra density, indicating that the N-terminal GST tag of the recombinant Ubp6 is not resolved in the 26S–Ubp6–UbAld reconstruction because it is flexibly linked to the UBL domain by an 8-residue linker.

3.1.5 Positioning of Ubp6

In order to analyse the structure of proteasome bound Ubp6–UbAld in more detail, the full 26S–Ubp6–UbAld dataset was ‘cleaned‘ and refined as described in subsection 2.4.1. This procedure lead to a map of an overall resolution of 9.5 Å (Figure 3.1.6 A). Determination of the local resolution showed that while many parts of the 26S proteasome are resolved at sub-nanometer level, the extra density is less

well-defined (Figure 3.1.6 B). This locally reduced resolution is most likely caused by structural heterogeneity of Ubp6, which is consistent with differences in the extra density of the individual classes found in the initial classification (Figure S4 in [Aufderheide et al., 2015a]).

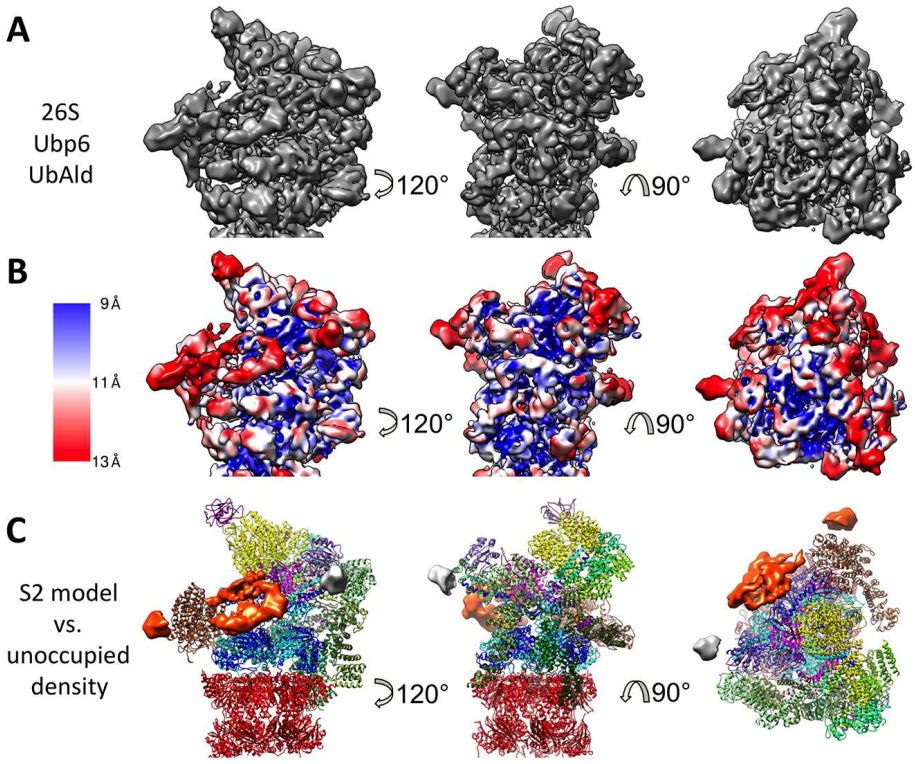

Figure 3.1.6: The 26S–Ubp6–UbAld complex at a global resolution of 9.5 Å: (A) Refined density filtered to its local resolution. (B) Same map as in (A) coloured according to the determined local resolution. (C) Comparison of the atomic model of the s2 state and the density. The difference between the two is rendered as an isosurface. The orange density is specific for the 26S–Ubp6–UbAld data, and the gray area corresponds to the disordered N termini of the coiled-coils of Rpt4/5, which are also present in the EM density from 26S alone but are not included in the model. Figure adapted from [Aufderheide et al., 2015a].

The refined density is clearly in an s2-like state. Therefore, the available s2 pseudo-atomic model (PDB code 4CR3) was rigid-body-fitted into the map. This allowed us to isolate computationally the segments not accounted for by the model (Figure 3.1.6 C). In addition to the extra density, the difference between the map and model includes a small density at the tips of the coiled-coils of Rpt4/5. However, this density is also present in the s2 26S cryo-EM maps (Figure 3.1.4 A), although it is not explained by the s2 atomic model and, therefore, does not correlate with Ubp6. The extra density attributed to Ubp6 consists of two segments. The smaller one is attached to Rpn1 and its volume approximately matches that of the UBL domain of Ubp6. It contacts Rpn1 in proximity to the helices H2–H5 of its toroid

domain. The larger segment is highly similar in size, shape and volume to the atomic structure for the catalytic USP domain of Ubp6 (PDB code 1VJV) and Usp14 bound to UbAld (PDB code 2AYO) [Hu et al., 2005].

3.1.6 A pseudo-atomic model for the 26S–Ubp6–UbAld complex

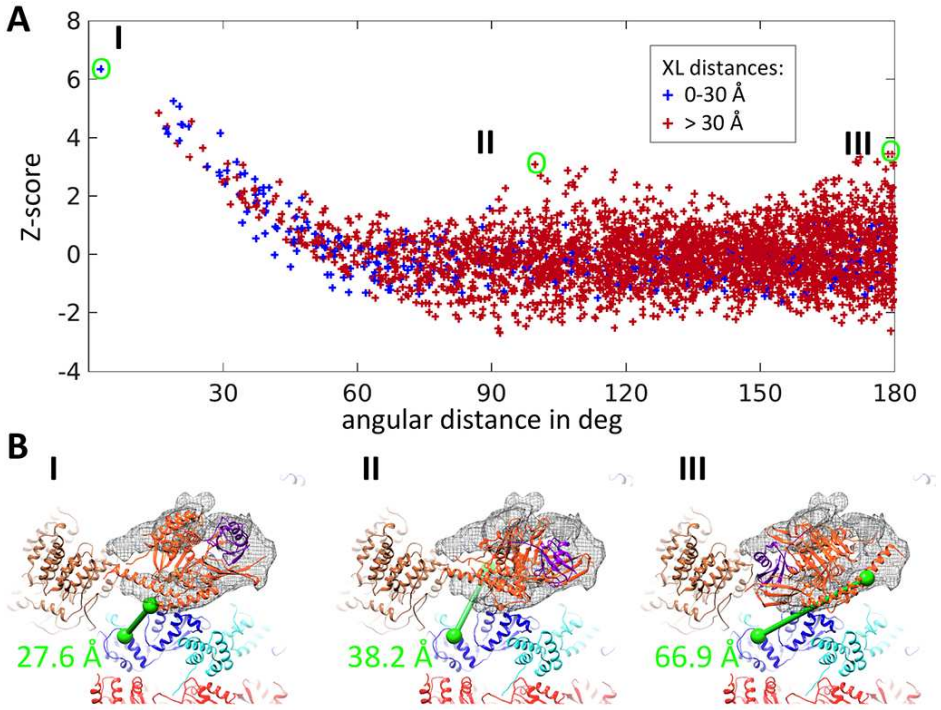

Figure 3.1.7: Fit of the Ubp6 USP domain in the refined 26S–Ubp6–UbAld density. (A) Assessment of orientation specificity of fitting. The Z-scores of the correlation are plotted against the angular distance to the best-fitting result, which is more than six standard deviations above the mean value. The coordinates are coloured according to the distance of the cross-linked residues of the USP domain and Rpt1 (Table 3.1.4). (B) Visualisation of the crosslink for the three best-scoring solutions in A (orange: Ubp6; purple: UbAld; blue: Rpt1; brown: Rpt1; cyan: Rpt5; red: CP). Figure adapted from [Aufderheide et al., 2015a].

In contrast to the small segment of the extra density, which is too small for fitting the UBL domain of Ubp6 accurately at the achieved resolution, the larger segment could be used to position an atomic model of USP domain ($Ubp6_{USP}$, residues 104-499) bound to UbAld. The model of $Ubp6_{USP}$–UbAld was created by superposing the $Ubp6_{USP}$ crystal structure (PDB code 1VJV) onto the Usp14–UbAld structure (PDB code 2AYO). In order to fit this model into the large segment of the extra density, my colleague Florian Beck supplied me with a six-dimensional (exhaustive translation and orientation) correlation search procedure, which was applied to the $Ubp6_{USP}$–UbAld template against the area of the extra density. To assess the

specificity of the orientations, the respective correlation values were transformed to Z-scores in a two-step procedure. Firstly, a Fisher transformation was applied to the correlation values and secondly, the results were normalised by subtracting the mean and dividing by the standard deviation. The Z-scores reveal that the best-fitting orientation scores significantly better than all other solutions (Figure 3.1.7 A). The scores decreased slightly when Ubp6$_{USP}$ alone was used as a search template, but the angular positioning remained the same (Figure S8 in [Aufderheide et al., 2015a]).

In the best-fitting result (Figure 3.1.7 B, I) UbAld is positioned in the part of the extra density, which is closest to Rpn10 and Rpn11, facing the OB-ring of the ATPase. Interestingly, the extra density in the classified subset of the 26S–Ubp6 dataset lacks density in precisely the area assigned to UbAld (Figure 3.1.8 A), whereas the subsets from the 26S–UbAld and 26S–Ubp6–UbAld datasets exhibit the complete extra density (Figure 3.1.8 B-C). Taken together, the findings indicate that this part of the extra density represents UbAld.

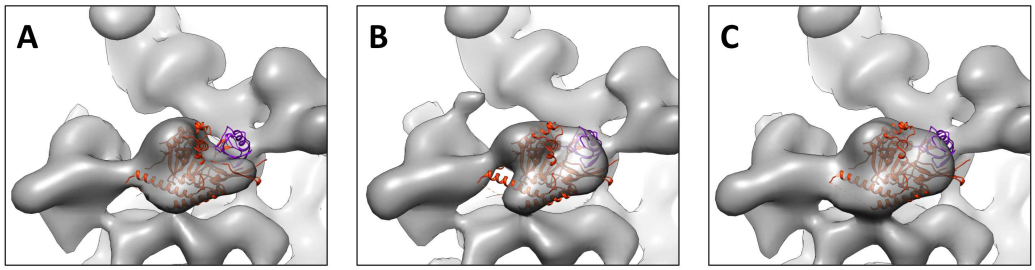

Figure 3.1.8: Comparison of the best-fitting Ubp6-UbAld model with extra-density in classified subsets of (A) 26S–Ubp6, (B) 26S–Ubp6–UbAld, (C) 26S–UbAld. Strikingly, UbAld is positioned precisely in the area, where the 26S–Ubp6 reconstruction is lacking density in comparison with the reconstructions from the two datasets containing UbAld.

The positioning of Ubp6 is further supported by the XL-MS data (Table 3.1.4). Despite crosslinks which involve residues within unstructured domains, one crosslink was identified between lysines of Ubp6 and Rpt1 that are covered by the available atomic models (PDB codes 1VJV and 4CR3, respectively). For the best fit result of Ubp6, the distance of the respective Cα -atoms is $\sim$28 Å, which is below the cut-off of 30 Å previously applied for intersubunit crosslinks of the 26S proteasome [Walzthoeni et al., 2012]. For the majority of alternative solutions the distances are much larger (Figure 3.1.7). Thus, the analysis of the XL-MS data of 26S–Ubp6–UbAld constitutes orthogonal evidence for the suggested placement of the catalytic domain of Ubp6 bound to the 26S proteasome.

The determined 26S–Ubp6$_{USP}$–UbAld model, shows the N-terminal end of the

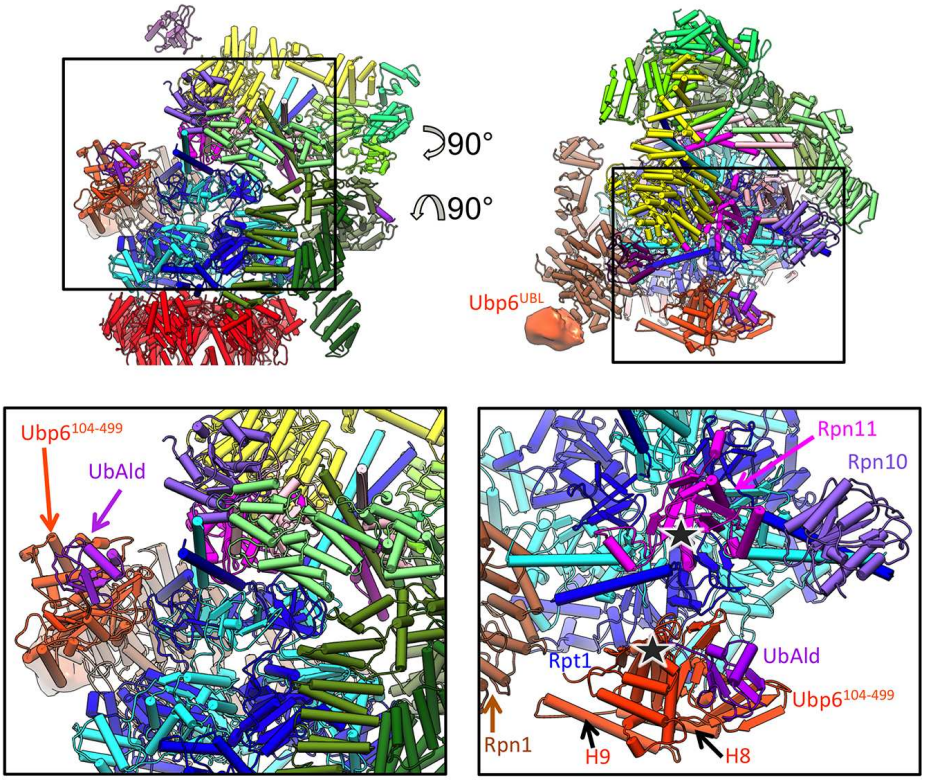

Figure 3.1.9: The model of proteasome-bound Ubp6–UbAld: (Upper row) Atomic model of the 26S–Ubp6–UbAld complex seen in two different views. (Lower row) The boxed region is enlarged for better visualisation of $Ubp6_{USP}$ ($Ubp6^{104-499}$ in the image) and UbAld. In the enlarged top view (Lower Right) Rpn13, Rpn2, Rpn8, and the PCI horseshoe have been removed for clarity. The stars mark the active sites if Ubp6 and Rpn11. Figure adapted from [Aufderheide et al., 2015a].

$Ubp6_{USP}$ domain (residue 104) in direct proximity to Rpn1. This finding agrees well with the proposed positioning of the UBL domain also at Rpn1. An additional contact with Rpn1 is established by helices H8 and H9 that protrude from the palm domain of Ubp6 towards Rpn1 (Figure 3.1.9). This segment is specific for Ubp6 and is not present in related USP enzymes, such as herpes virus-associated ubiquitin-specific protease [Hu et al., 2005]. The N terminus of H9 is most proximal to the very N-terminal helix of the toroid domain of Rpn1. H8 and H9 are connected by an unstructured linker, which might also play a role in the interaction. The largest interaction area of $Ubp6_{USP}$ with the 26S proteasome is formed by a patch constituted by Ubp6 residues K316–V333 and E473–S488, which contacts the OB domain of Rpt1. Interestingly, the K316–V333 loop and an adjacent loop block the binding groove for the C terminus of ubiquitin in the crystal structure of free Usp14 [Hu et al., 2005]. The interaction area in Rpt1 includes residue from the structured regions G158–E169 and Y181–R190. Intriguingly, an extended unstructured region

(residues G110–D140) is located in immediate proximity to this area. This segment is specific for Rpt1. Therefore, it is conceivable that it has evolved to interact with Ubp6. The catalytic triad of Ubp6 faces the Rpt1/2 coiled-coil (Figure 3.1.9), whereas the UbAld moiety is positioned between the coiled-coils of Rpt1/2 and Rpt4/5. Therefore, in the complex UbAld, i.e. Ubp6 bound ubiquitin, is found in immediate proximity of the pore of the ATPase OB-ring, in direct vicinity of the integral DUB Rpn11 and close to the ubiqutin receptor Rpn10.

3.2 Discussion

3.2.1 Flexibility of Ubp6 and the 26S–Ubp6 complex and stabilisation by UbAld

The overall reconstruction as well as the classification of the 26S–Ubp6 dataset (Figure 3.1.3 and Figure 3.1.4 B) both underline the conformational heterogeneity of the 26S proteasome in presence of Ubp6. This heterogeneity hinders the detection of Ubp6 related density. In particular, density arising from the bound UBL domain averages out in the overall reconstruction as the positioning of the interacting subunit Rpn1 differs significantly between the s1 and s2 state. Although the UBL domain becomes visible after classification in the reconstruction of s2-like particles, only a very small fraction of particles (6%) identified by focused classification shows a defined extra density, which can be assigned to the USP domain of Ubp6. The two domains are connected by a flexible linker, which allows the USP domain to adopt various conformations, as a consequence the density averages out in the reconstruction of s2-like particles.

The presence of UbAld stabilises the conformation, in which both domains of Ubp6 are visible, which manifests itself in the predominance of the extra densities and the s2-like particles of the 26S–Ubp6–UbAld dataset (Figure 3.1.3 and Figure 3.1.4 C). The refinement of the reconstruction from these particles allowed us to derive a pseudo-atomic model of the 26S–Ubp6–UbAld complex (subsection 3.1.6) and, thereby, to study the stabilisation effect on a molecular level. The patch of residues in Ubp6 which form the connection with Rpt1 (K316-V333 and E473-S488) are in close proximity to residues that block the active side of Ubp6 in the unbound state (loops BL_1 and BL_2). A recently published higher-resolution structure of the human 26S proteasome in complex with Ubp6–UbAld even stated a direct interaction between the BL_1 and BL_2 loops and the OB-ring of the ATPAse for this organism [Huang et al., 2016]. Interestingly, binding of ubiquitin or UbAld to Ubp6

causes a conformational change in the BL_1 and BL_2 loops [Hu et al., 2005]. Therefore, the stabilisation of the 26S–Ubp6 complex is most likely caused through structural changes in the patch of Ubp6 residues interacting with Rpt1 upon binding of UbAld to Ubp6. Assuming, the changes in this patch indeed stabilise the interaction with Rpt1, a conformational change to the s1-like state would be sterically hindered, due to an interference of Rpn1 with the USP domain of Ubp6 upon the conformational change. This is in line with the predominance of s2-like particles.

In a structural study, similar the one presented here, Ubp6 bound to ubiquitin vinyl sulfone (UbVS), which inhibits Ubp6 in a similar manner than UbAld, was added to the 26S proteasome [Bashore et al., 2015]. Different from our study, the authors added ATP-γS to their sample to get a well defined extra density in their map calculated from negative stain electron microscopy data. ATP-γS induces the s3-like conformation. This suggests that the proteasome has to be in an s3- (or s2-) like state to form a complex with Ub-bound Ubp6 (study of [Bashore et al., 2015]), whereas ubiquitin (UbAld) can bind to the 26S–Ubp6 complex without an external condition inducing the s2 or s3 state (data presented here). This comparison leads to the speculation that binding of ubiquitin (or UbVS/UbAld) might cause a change of the conformation of free Ubp6 or of its flexible properties.

3.2.2 Structure of the 26S–Ubp6 Complex

The model determined based on the refined structure of the 26S–Ubp6–UbAld complex (subsection 3.1.6) gives insights into the structural arrangements of the subunits within the complex. In this conformation of the complex, both domains of Ubp6 contact the 26S proteasome. The UBL domain binds to Rpn1 close to helices H2–H5 of its toroid domain and seems to function as an anchor. A recent biochemical study located the binding site of the $Ubp6_{UBL}$ domain on Rpn1 to the residues 419-436 within the toroid helix H5, which is in excellent agreement with our structural data [Shi et al., 2016]. The USP domain interacts with the ATPase OB-ring through Rpt1, which puts it in close proximity to Rpn10, Rpn11 and the entry to the ATPase pore and, therefore, in an ideal position to act on a bound substrate. Interestingly, a recent study has pointed out that in this position cleaving of distal Ub moieties is sterically occluded [Lee et al., 2016]. Therefore, the position of $Ubp6_{USP}$ obtained from our density is rather in line with the *en-bloc* removal identified for cyclin B substrates in the recent study [Lee et al., 2016], than with previous biochemical evidence, indicating that Ubp6 shortens polyubiquitin chains from the distal end [Hu et al., 2005; Lee et al., 2011].

Comparison with other structural studies

The positioning of $Ubp6_{USP}$ in the 26S–Ubp6–UbAld complex determined in this work (Figure 3.2.1 A) has recently been confirmed by a corresponding study on the human homologs, Usp14 and the human 26S proteasome [Huang et al., 2016]. Surprisingly, although the authors claim an overall resolution of 4.4 Å, they did

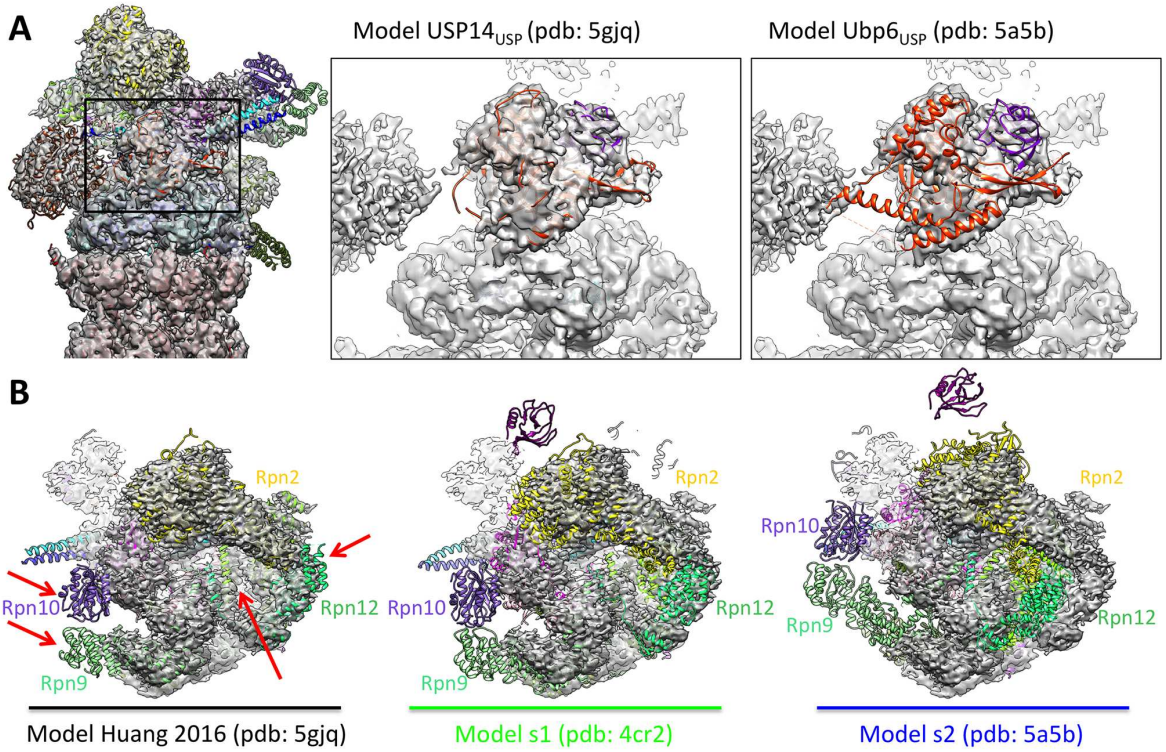

Figure 3.2.1: Density obtained for human 26S–Usp14–UbAld from [Huang et al., 2016] (EMDB: 9511) compared with different models. (A) Model from [Huang et al., 2016] (left and middle, DPB: 5gjq). The region of $Usp14_{USP}$ is enlarged (middle) and a comparison with the location obtained for $Ubp6_{USP}$ (right, PDB: 5a5b) shows that the positioning of the USP domain is identical, although some secondary structure elements differ between yeast and human. (B) The density is displayed in a top view and compared with the s1 model (middle, PDB: 4cr2) and the s2 model (right, PDB: 5a5b). Areas that differ significantly between the two states coincide with those poorly resolved in the map (left panel, red arrows).

not observe any density that can be attributed to the UBL domain of Usp14. Additionally, the reconstruction seems to be in an overall s1-like state and the authors claim that Rpn1, which appears to be flexible, is the only notable difference to the s1 arrangement of the RP subunits. However, all regions that significantly differ between the s1 and s2 state, such as Rpn1,5,9,10,12 as well as the helical bundle, are poorly resolved or average out completely in the reconstruction filtered to the claimed resolution (Figure 3.2.1 B). Strikingly, the classification was not focused on

one RP and the resulting classes seem to reflect the particle quality rather than different conformational states (compare [Huang et al., 2016] Supplementary Figure 9). The resulting mix of s1- and s2-like particles explains the lower resolution in the areas mentioned above. In particular, the weak density for Rpn1 is most likely caused by averaging over its significantly different positions in the s1 and s2 states, rather than flexibility within a states as claimed. This prohibits the detection of the UBL domain and also effects Ubp6 due to the overlap of bound Ubp6 in the s2 state and Rpn1 in the s1 state, which offers an explanation, why the resolution of this area was not good enough for accurate fitting as stated in [Huang et al., 2016].

In a negative-stain EM study [Bashore et al., 2015], the 26S–Ubp6–UbVS complex was visualised in the presence of ATP-γS. Therefore, the 26S proteasome is in an overall s3-like state, which differs from the s2-like conformation found for the 26S–Ubp6–UbAld complex. Although the overall localisation of $Ubp6_{USP}$ remains the same, the position of $Ubp6_{USP}$ in the 26S–Ubp6–UbVS–ATP-γS reconstruction (s3-like state) is slightly shifted towards the 20S in comparison with the density in the 26S–Ubp6–UbAld complex (s2-like state) (see Figure 3.2.2 B). Interestingly, Rpt1

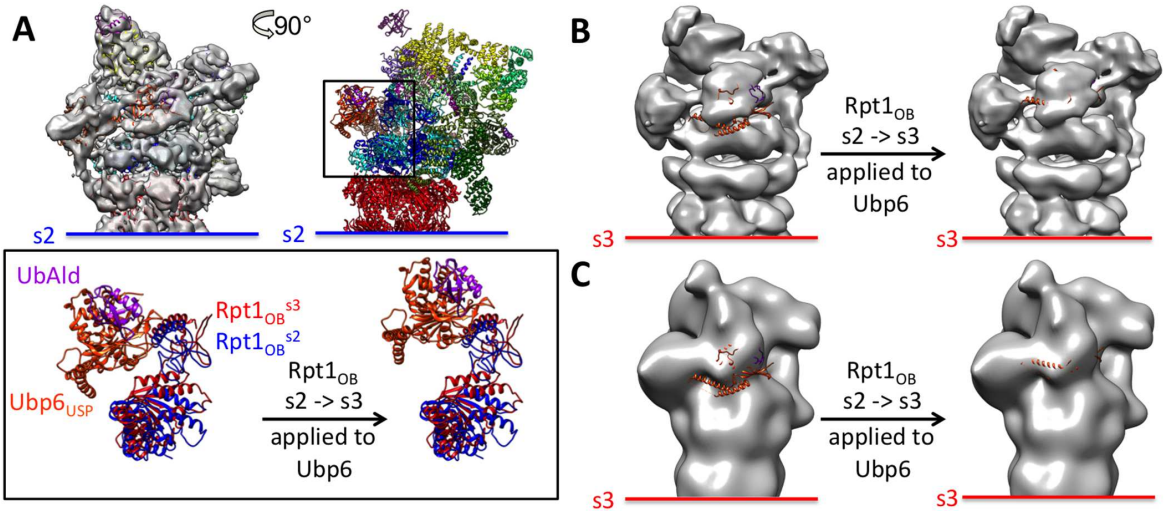

Figure 3.2.2: (A) top: Positioning of Ubp6 in the 26S–Ubp6–UbAld complex, the box marks the orientation used for the bottom panel; bottom: Comparison of the conformations of Rpt1 in the s2 (blue) and the s3 (red) state. On the left, $Ubp6_{USP}$ in complex with UbAld is positioned as determined from the 26S-Ubp6-UbAld complex (s2 state). On the right, the movement of the $Rpt1_{OB}$ domain between the s2 and s3 state has been applied to $Ubp6_{USP}$. (B) Comparison of the Ubp6 positions displayed in A with the density of 26S–Ubp6–UbVS–ATPγS from [Bashore et al., 2015] (EMDB: 2995). (C) Comparison of the Ubp6 positions displayed in A with the subtomogram average of *in-situ* 26S proteasomes from neuronal cells in an activated state from [Asano et al., 2015] (EMDB: 2831).

undergoes a significant rotation between the s2 and s3 state, moving away from the 20S. The movement is particularly pronounced for the OB domain ($Rpt1_{OB}$), to

which Ubp6 binds. This transformation places the $Ubp6_{USP}$–UbAld model in the extra density observed in presence of UbVS (see Figure 3.2.2 A&B). Thus, the two structural results agree in the positioning of $Ubp6_{USP}$.

Similarly, the determined position of $Ubp6_{USP}$–UbAld is compared with a subtomogram average of 26S proteasomes from hypocampal neurons identified to be in a substrate processing (s3-like) state (see Figure 3.2.2 C). This reconstruction exhibits an extra density, which could not be assigned to any of the integral subunits of the 26S proteasome and was suggested to be caused by several PIPs acting in concert on a processed substrate. Also here, the $Ubp6_{USP}$–UbAld model fits well into the lower parts of the extra density after the s2-s3 movement of $Rpt1_{OB}$ is applied. It is likely that $Ubp6_{USP}$ causes parts of the extra density, as the shape of this part of the density nicely agrees with the $Ubp6_{USP}$ model and the density of Rpn1 is turned outwards at the position, where the UBL domain was identified to bind. Further experiments are required to prove this hypothesis.

Correlation of Ubp6 binding with substrate processing

In all three structures discussed above, the appearance of an extra density assigned to Ubp6 coexists with an s2- or s3-like state of the 26S proteasome. Both states have been linked to substrate processing [Unverdorben et al., 2014; Matyskiela et al., 2013]. In contrast to these two states the s1-state is believed to constitute a lower energy state responsible for the initial binding of substrates [Unverdorben et al., 2014]. Interestingly, in the s1-state the binding of $Ubp6_{USP}$ to Rpt1 as shown by our model is sterically inhibited. This is consistent with the absence of a corresponding density in the s1-like classes (see Figure 3.1.4). Taken together, the findings suggest a correlation of a stable binding of Ubp6 with substrate processing.

Interplay of Ubp6 with other subunits of the 26S proteasome

A notable difference of the s2 and s3 state compared with the s1 state is a repositioning of Rpn10 into the direct neighbourhood of the $Ubp6_{USP}$-domain in the complex. This placement into proximity of Ubp6 implies that Rpn10 has a cooperative role in transferring substrate to Ubp6.

Another subunit found in direct vicinity of Ubp6 is the integral DUB subunit Rpn11. Although both proteins are DUBs, they belong to different DUB families. Ubp6 is part of the family of ubiquitin-specific proteases (USPs) and Rpn11 is a metalloprotease (subsection 1.3.1). Interestingly, Ubp6 and Rpn11 appear to have complementary roles during substrate degradation. The activity of Rpn11 is ATP-

dependent and enhances substrate degradation [Verma et al., 2002; Yao and Cohen, 2002; Pathare et al., 2014; Worden et al., 2014], whereas the removal of Ub by Ubp6 may suppress the degradation of substrates [Leggett et al., 2002; Lee et al., 2010; Crosas et al., 2006; Lee et al., 2016].

The model of the 26S–Ubp6–UbAld complex reveals that the active sites of Ubp6 and Rpn11 are positioned in vicinity of to the mouth of the OB-ring (~50 Å and ~30 Å, respectively) and of each other (~40 Å). In the presence of ATP-γS, Ubp6 and Rpn11 were reported to come even closer together (~30 Å [Bashore et al., 2015]) due to the movement demonstrated in Figure 3.2.2. The proximity of the two active sites may allow simultaneous processing of substrates by the two DUBs, possibly causing an increased efficiency of proteasomal degradation for specific types of ubiquitylation patterns [Lu et al., 2015]. However, the small distance between Ubp6 and Rpn11, especially in the presence of ATP-γS, might also sterically restrict the access of other substrates to Rpn11 and thereby inhibit deubiquitylation by Rpn11 (see subsection 3.2.4 for further discussion).

3.2.3 Activation of Ubp6

Biochemical studies have indicated that Ubp6 is activated upon binding to the 26S proteasome [Leggett et al., 2002; Lee et al., 2010]. Crystal structures of free $Ubp6_{USP}$ and $Usp14_{USP}$ suggested that two loops (BL_1 and BL_2) block its active site in the unbound state. These loops adopt a different conformation in the crystal structure of $Usp14_{USP}$ bound to UbAld [Hu et al., 2005]. The conformational change of these loops provides the C-terminal end of UbAld access to the catalytic site of Usp14. Intriguingly, BL_1 and BL_2 are located in the area involved in the binding of Ubp6 to Rpt1. Therefore, our structural results support the notion that the physical interaction with Rpt1 leads to a conformational change of BL_1 and BL_2 activating Ubp6.

In line with our structural results, Bashore and colleagues demonstrated that the presence of Rpn1 is not sufficient to activate Ubp6, wheras the additional presence of all other base subunits, which includes the ATPase, increases the hydrolysis of Ub-AMC significantly [Bashore et al., 2015]. Interestingly, the addition of ATP-γS to the 26S–Ubp6 complex further enhanced the activity of Ubp6. As ATP-γS induces conformational switching into the s3 state, in which the interaction region in Rpt1 is well exposed, this finding further supports that the activation of Ubp6 is stimulated through the interaction with Rpt1.

3.2.4 Effects of Ubp6 on the catalytic activity of the 20S

As described in section 3.1.1, we have confirmed the findings from [Peth et al., 2009] that, independent of its own activity, Ubp6 modulates the activity of the CP especially in the presence of ubiquitin or UbAld (Figure 3.1.1). The observed increase in degradation of small peptides by the 20S in the presence of Ubp6 and UbAld was originally attributed to a hypothesised opening of the gate in the α-ring of the 20S. However, the most notable difference in our results is the predominance of s2-like particles (Figure 3.1.4). Therefore, the enhanced degradation is most likely caused by the better alignment of the ATPase channel axis and the 20S, characteristic for the s2 and in particular the s3 state. This improved spatial alignment could facilitate the access of small peptides to the gated pore of the 20S. Similarly, an increase in degradation of small peptides by the 20S upon addition of ATP-γS to the 26S proteasome could be explained by an overall conformational change from the s1 to the s3 state [Sledz et al., 2013].

Ubiquitin-bound Ubp6 also increases ATP-hydrolysis by the ATPase [Peth et al., 2013; Bashore et al., 2015]. Our observation of a change in the state occupancy upon binding of Ubp6 to Rpt1 implies an alteration of the energy landscape, which might lead to an increased ATP hydrolysis rate.

In contrast to the increase in small peptide degradation and ATP hydrolysis, Ubp6 has been reported to delay degradation of folded and ubiquitylated substrates in a catalytic and noncatalytic manner [Hanna et al., 2006; Leggett et al., 2002; Lee et al., 2011]. From our structural results, we can derive two possible explanations for this effect. Catalytically, Ubp6 is near the OB-cavity (section 3.2.2) of the ATPase, well positioned to cleave Ub chains until substrates are released. Noncatalytically, ubiquitin-bound Ubp6 was found to inhibit deubiquitylation by Rpn11 [Hanna et al., 2006; Bashore et al., 2015], which can be explained by the small distance between the two DUBs in an arrangement that restricts access of substrates to Rpn11, especially in the substrate-bound (s3-like) state (section 3.2.2), as suggested in [Bashore et al., 2015].

Bashore and colleagues also studied single and multiple turnover of folded but ubiquitin independent substrates [Bashore et al., 2015]. They found that Ubp6 on its own neither influenced single nor multiple turnover. This is not surprising as the degradation of ubiquitin-independent substrates neither depends on ubiquitin receptors (Rpn10) nor DUBs (Rpn11 and Ubp6). However, in presence of ubiquitin-bound Ubp6 multiple turnover was drastically decreased, while single turnover was not affected. From this result the authors concluded that Ubp6 binds to Rpt1

when the 26S proteasome is in a substrate-bound conformation. Furthermore, they suggest that this conformation is then stabilised by Ubp6 as long as ubiquitin is bound to Ubp6, in order to allow complete degradation, before a new substrate can bind. If Ubp6 is stalled in the ubiquitin-bound conformation, as induced by UbAld, UbVS or inactive Ubp6, the 26S proteasome is constantly trapped in the s2 or s3 conformation and cannot engage the next substrate.

Taken together, our structural data of the 26S–Ubp6 complex in presence and absence of UbAld can explain effects observed by biochemical assays. The structural and biochemical results form a coherent picture of the influence of Ubp6 on the 26S proteasome and advance the understanding of proteasomal substrate degradation.

4 High-resolution structure of the human 26S proteasome

The structure of the human 26S proteasome was studied, aiming at the highest resolution possible. The project included three distinct aspects, which were addressed by different individuals. The human 26S proteasomes were purified by Andreas Schweitzer and the protocol is discussed in his PhD thesis [Schweitzer, 2016]. My main responsibility was to implement and apply an image processing pipeline suitable for the DED data of the 26S proteasome. The obtained high-resolution structure furthermore served as a basis for an atomic model built by our collaborator Till Rudack (University of Illinois Urbana-Champaign). A refinement of the model as well as the analysis and interpretation of the results was achieved in a close collaboration by the three of us. The combined efforts resulted in a shared first-author publication [Schweitzer et al., 2016], which is the basis of this chapter.

4.1 Results

The results presented here comprise my main contribution to the project. Therefore, the section includes a description of the intermediate results of the implemented workflow and the structural insights obtained from the high-resolution structure in conjunction with the density-based model. Details on the sample purification and characterisation as well as the initial model building can be found elsewhere [Schweitzer, 2016; Schweitzer et al., 2016].

4.1.1 The image processing workflow: improving the resolution step-by-step

As described in subsection 2.4.2 the picked particles were sorted into 230,000 single- and 458,000 double-capped (sc26S and dc26S) particles and processed separately until they are merged for the final refinement. As sc26S particles do not have any pseudo-symmetry axis, they can in principle be processed with standard tools and

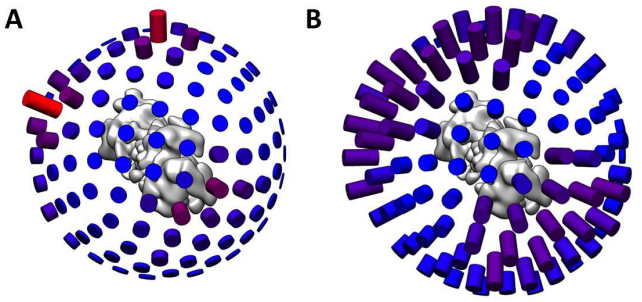

C

Test dataset	Resolution Mask RP	Runtime [h] on 128CPUs
182,700 particles	5.7 Å	73
106,700 particles randomly reduced	6.4 Å	28
106,700 particles reduced by PD value	5.9 Å	26

Figure 4.1.1: Uneven angular distribution enables data reduction. Angular distribution of all dc26S particles before data reduction (A) and of the reduced set of dc26S particles after discarding particles from highly-populated classes (B). (C) The obtained resolution values from applying the method to a subset of particles show no significant impact of discarding particles with low rlnMaxValueProbDistibution values (PD). Figure adapted from [Schweitzer et al., 2016].

procedures. Unfortunately, only one third of the picked particles were sc26S. The majority was categorised as dc26S. Therefore, a workflow for the dc26S particles was implemented to adapt the processing in RELION to the peculiarities and challenges of dc26S data, such as C2 pseudosymmetry and conformational heterogeneity (subsection 2.4.2). In the following, the outcome of each step of the dc26S workflow is presented, illustrating how the challenges were met.

In order to achieve a high-resolution structure of the 26S proteasome, large datasets are required, due to the presence of multiple RP states (section 1.2), flexibility of subunits of the 26S proteasome and preferred orientation of particles on the grid. Processing of several hundred thousands of particles makes refinement and particle polishing in RELION slow and challenging in terms of computer memory. During the last iteration of the refinement and at the beginning of particle polishing, reconstructions of unfiltered volumes are calculated using all spatial frequencies of all angular classes, which is a major reason for the high amount of memory required. Therefore, we had to reduce the number of particles without reducing the resolution, before further processing of the data.

In a first step, we aligned and reconstructed the dc26S particles imposing C2-symmetry. Although the resulting angular distribution does not display completely missing projection angles, the angular classes are very unevenly populated (Figure 4.1.1 A), reflecting the preferred orientation on the grid.

Searching for a route to reduce the size of our dataset, we reasoned that discarding particles from highly-populated angular classes should only result in a minor loss in resolution. On a subset of ~180,000 particles, different criteria for discarding particles were tested. This assessment demonstrated that the most ef-

ficient way of data reduction is to decrease the occupancy of angular classes with an above average particle-per-class number by discarding those particles with the worst 'rlnMaxValueProbDistibution' values. This value is determined by RELION during the alignment and is an indicator of the particle quality because it is a measure of how unambiguously a particle can be assigned to the best matching angular class. Applying this method to the test subset only led to a negligible reduction in resolution (Figure 4.1.1 C). Therefore, we opted to decrease the size of the dc26S data set from 460,000 to 270,000 particles according to the outlined protocol. As a result, the particles in the reduced data set are more evenly distributed over the angular classes (Figure 4.1.1 B). For all further steps, this reduced dc26S particle set was used.

Table 4.1.1: Resolutions obtained from human 26S proteasome reconstructions at different steps of the workflow. The steps refer to the processing of dc26S particles, in the last step RPs from the cleaned sc26S were added as shown in Figure 2.4.2. For each refinement, the resolution was measured with a soft mask around one half of the 26S proteasome. Please note, 'combined*' is the resolution determined from the FCS between the 2 data half sets and 'cleaned' refers to the particle sets after 3D classification, discarding bad classes.

Workflow Step	number of particles or RPs	applied symmetry	resolution [Å]
particles before polishing	135,000	C2	4.63
particles after polishing	135,000	C2	4.28
particles after polishing combined*	270,000	C2	4.11
RPs (after *in-silico* separation)	540,000	C1	4.08
cleaned RPs	360,000	C1	4.11
cleaned RPs dc26S and sc26S	460,000	C1	3.93

After reduction of the dataset, we subjected the particles to polishing. Due to memory restrictions, we had to split the 270,000 particles into two subsets, which were processed separately. The particle polishing (as described in subsection 2.4.2), based on a C2 refinement, increased the resolution by ∼0.5 Å. Table 4.1.1 summarises the obtained resolutions for this and all further steps. Visual inspection of the reconstructions shows that the polishing procedure particularly improves the side chains (Figure 4.1.2 A&B), which is in line with the increased signal in the high-resolution range demonstrated by a comparison of the corresponding FSCs (Figure 4.1.2 C).

Upon refinement of the polished, 'shiny', particles (Figure 4.1.2 B), helices in the CP and the ATPase significantly improved on the side chain level. However, the

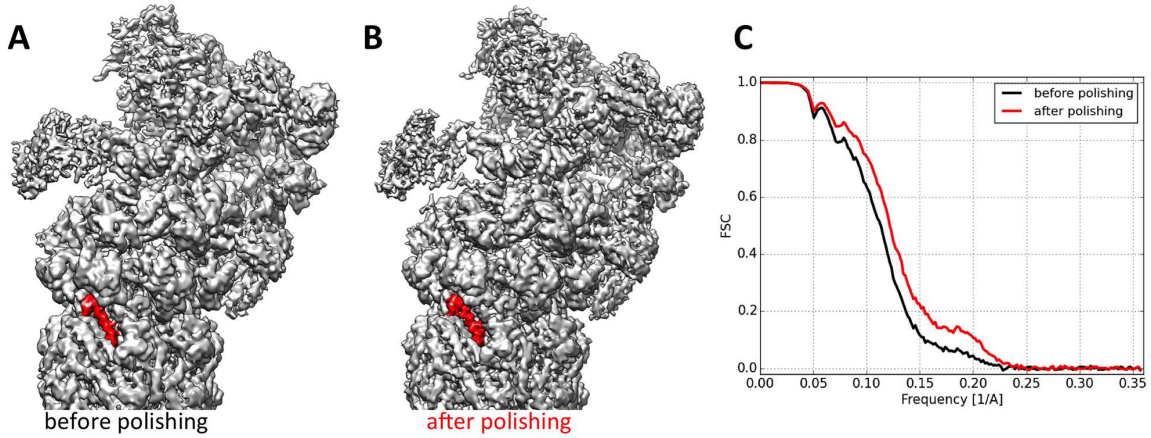

Figure 4.1.2: Particle polishing in RELION increases the high-resolution signal. (A) Map reconstructed from one half of the dc26S particles before polishing. (B) Map reconstructed from the same particles as in A after polishing. Note the better visible side chains of e.g. the helix highlighted in red. (C) The FSCs calculated before (black) and after (red) particle polishing further demonstrate the increase of signal in particular in the high-resolution range.

outer parts of the RP remained 'hairy', indicating heterogeneity of RP states. In order to separate the different states, we had to address the broken C2 symmetry first, done by the *in-silico* separation of the RPs as described in subsection 2.4.2.

After the *in-silico* separation of the RPs, 540,000 RPs were subjected to 3D classification using a mask on one of the RPs and keeping the assigned projection angles constant. Since the reconstructions from previous steps were clearly in an s1-like conformation (Figure S2 [Schweitzer et al., 2016]), we aimed for a high-resolution structure of this conformation. Therefore, particles from badly aligned classes or classes that showed conformations different from the s1 state were discarded, leading to a 'cleaned' dataset of 360,000 RPs after two rounds of classification. A local refinement of these particles showed no decrease in the overall resolution (Table 4.1.1), whereas the signal of the outer parts of the lid relative to the 20S and the ATPase improved, indicating a successful cleaning by 3D classification.

In the last step, the alignment parameters of dc26S RPs and sc26S particles (processed as described in subsection 2.4.2) were refined together under restricted alignment conditions with a mask on one RP and the CP. The addition of 100,000 sc26S RPs only caused a minor increase in the average resolution of ∼0.15 Å, which is most likely within the error of precision, indicating that the limits of this dataset were reached. The density resulting from this final refinement was resolved to 3.9 Å on average, which is about $2/3$ of the Nyquist frequency. However, despite the efforts to clean the dataset from different RP conformations, the local resolution remained rather heterogenous, varying from ∼3.5 Å in the CP and parts of the ATPase to ∼8 Å in the outer parts of the lid (Figure 4.1.3 A). Due to this heterogeneous

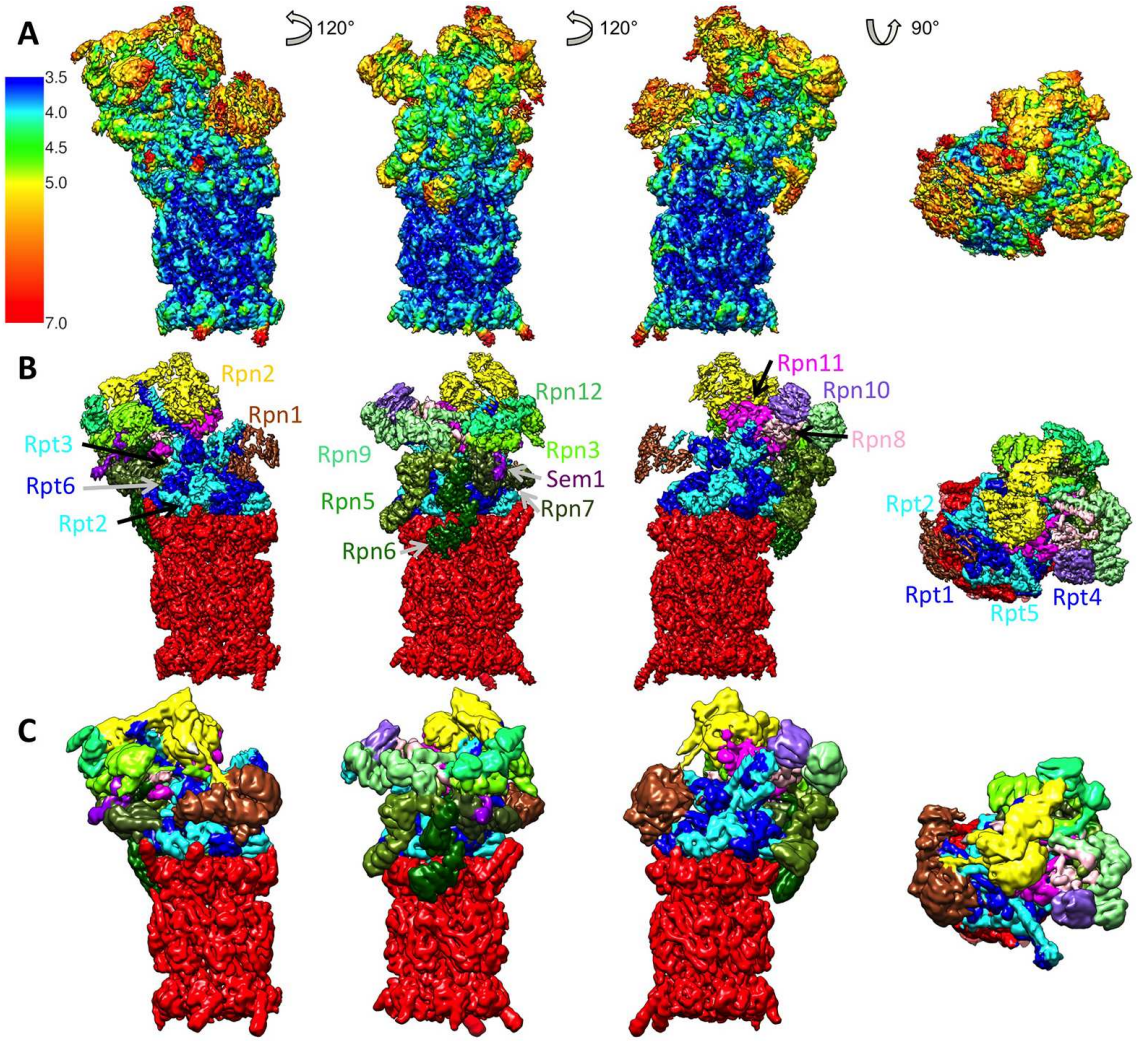

Figure 4.1.3: The final human 26S proteasome structure. (A) Map filtered to the average resolution of 3.9 Å, coloured according to its local resolution. (B) Map as in A but rendered at a different threshold and coloured by subunits. (C) Map filtered to 7.7 Å and coloured with respect to subunits as in B. Figure adapted from [Schweitzer et al., 2016].

local resolution, we analysed the final map filtered to two different resolutions, the average resolution of 3.9 Å and a lower resolution of 7.7 Å (Figure 4.1.3 B and C).

4.1.2 Evolutionary conservation of the 26S proteasome from yeast to humans

Fitting of the *S. cerevisiae* model of the s1 state (PDB: 4cr2, [Unverdorben et al., 2014]) into the density of the human 26S proteasome shows an overall agreement of the subunit arrangement, with the exception of the subunits Rpn1 and Rpn13 (Figure 4.1.4). Although the overall positioning of Rpn1 remains the same, the corresponding density in the human 26S proteasome is shifted towards Rpt1. Such a

shift of Rpn1 with respect to its position in yeast was also found in a subtomogram average of the mammalian 26S proteasomes from rat hypocampal neurones [Asano et al., 2015]. Therefore, this shift appears to be a structural difference between the yeast and the mammalian 26S proteasome. For Rpn13, no corresponding density can be identified in the reconstruction. This finding is consistent with quantification of subunit abundance by mass spectrometry data of the purified human 26S proteasome, indicating a low stoichometry of 10% for Rpn13 [Schweitzer, 2016], whereas in the 26S proteasome purified from yeast Rpn13 is present in nearly stoichiometric amounts (Table 3.1.1). Previous studies also found Rpn13 to be essentially absent in isolated human 26S proteasomes [Chen et al., 2010]. Most likely, substoichiometrically-bound Rpn13 dissociates from the 26S proteasome during the isolation procedure, because electron cryo-tomography studies of 26S proteasomes in rat neurons indicated a substoichometric occupancy of Rpn13 in the cellular environment [Asano et al., 2015].

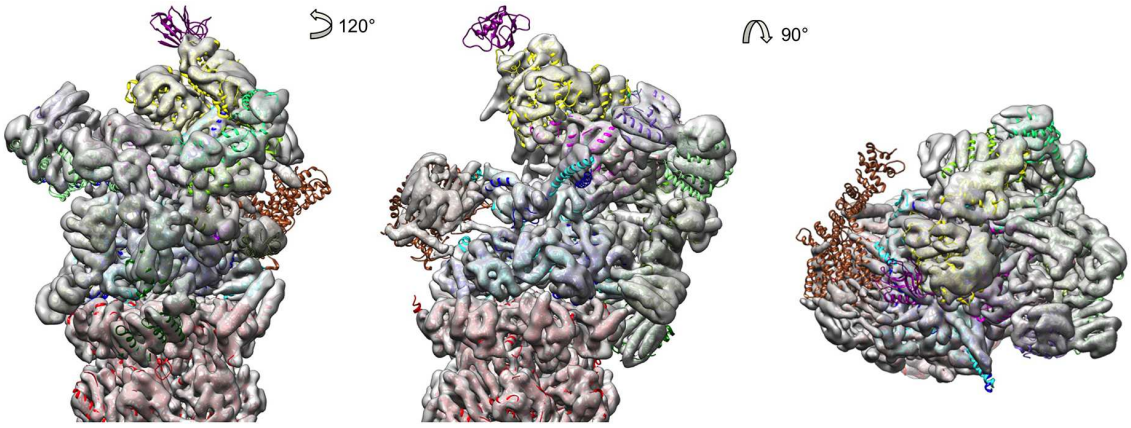

Figure 4.1.4: Pseudo-atomic model of *S. cerevisiae* (PDB: 4cr2) 26S proteasome fitted to the human reconstruction filtered to 7.7 Å resolution. Apart from the lack of Rpn13 in the human structure and a previously reported shift of Rpn1 ([Asano et al., 2015]), the overall architecture is well conserved. The subunits are coloured as given in Figure 4.1.3 B.

However, the structure and even most of the secondary structure elements of all other subunits align perfectly. This indicates a high structural conservation from yeast to human, which is consistent with the high sequence conservation of the RP subunits ($>$ 30% almost throughout). The conserved architecture does not confirm differences that have been suggested previously [da Fonseca et al., 2012]. In particular, Rpn8 and Rpn12, which were claimed to be located differently, remain largely invariant. The postulated differences between the human and the yeast RP in [da Fonseca et al., 2012] are likely caused by an overestimation of the resolution leading to a misinterpretation of the map, as suggested by [Lander et al., 2013].

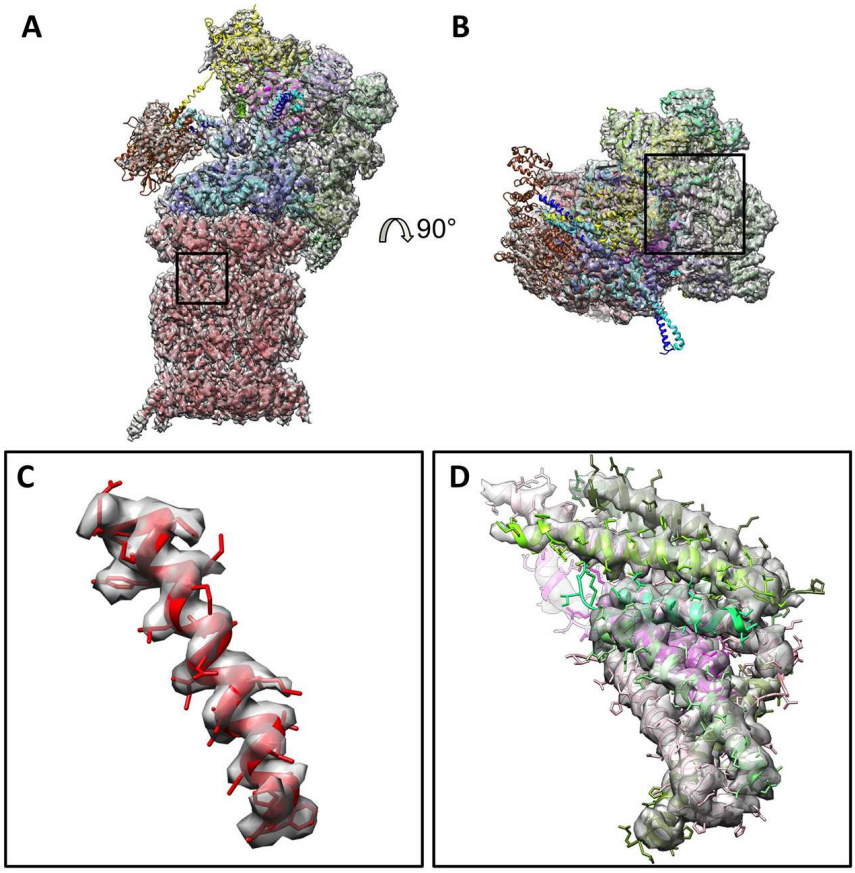

Figure 4.1.5: Model derived from homology modelling and the high-resolution human 26S proteasome map from two different views (A& B). Closeup on a helix in the CP (C) and the helical bundle (D), marked by black boxes in A and B, respectively. The subunits are coloured as given in Figure 4.1.3 B.

4.1.3 The atomic model of the human 26S proteasome

The high-resolution of the obtained map as well as the overall improved quality in comparison to previous studies [Unverdorben et al., 2014; da Fonseca et al., 2012] allowed for accurate model building. The initial model was obtained from an established comparative modelling strategy followed by fitting and refinement steps using the two maps filtered to 3.9 and 7.7 Å resolutions as depicted in Figure 4.1.3 (for details see [Schweitzer et al., 2016]). Throughout the entire map secondary structure elements like α-helices can be detected for all subunits, although with varying accuracy depending on the resolution. In the lower resolution areas, such as the lid subunits, we identified segments missing in previous models. Within the better resolved areas of the map (resolution $<$4 Å), such as the CP, the AAA-ATPase and the helical bundle, we were able to position the residues within secondary structure elements with high accuracy, due to unambiguous fitting of the side chains. An overview of the model is depicted in Figure 4.1.5 and the new insights therein are described in the following section.

4.1.4 Structural features of the human 26S proteasome revealed by high- and low-resolution information

Features of the RP lid subcomplex

The RP consists of two independently assembling subcomplexes, the base and the lid (see section 1.2 for details). The lid subcomplex is held together by a helical bundle, which is formed by C-terminal helices from all lid subunits with the exception of Sem1 [Beck et al., 2012; Estrin et al., 2013]. This small lid subunit was recently suggested to act as a ubiquitin receptor [Paraskevopoulos et al., 2014] and is positioned between Rpn7 and Rpn3 [Dambacher et al., 2016; Bohn et al., 2013]. In our reconstruction, we could trace a part of Sem1, which interacts with Rpn3 but has hardly any secondary structure elements (Figure 4.1.6 A).

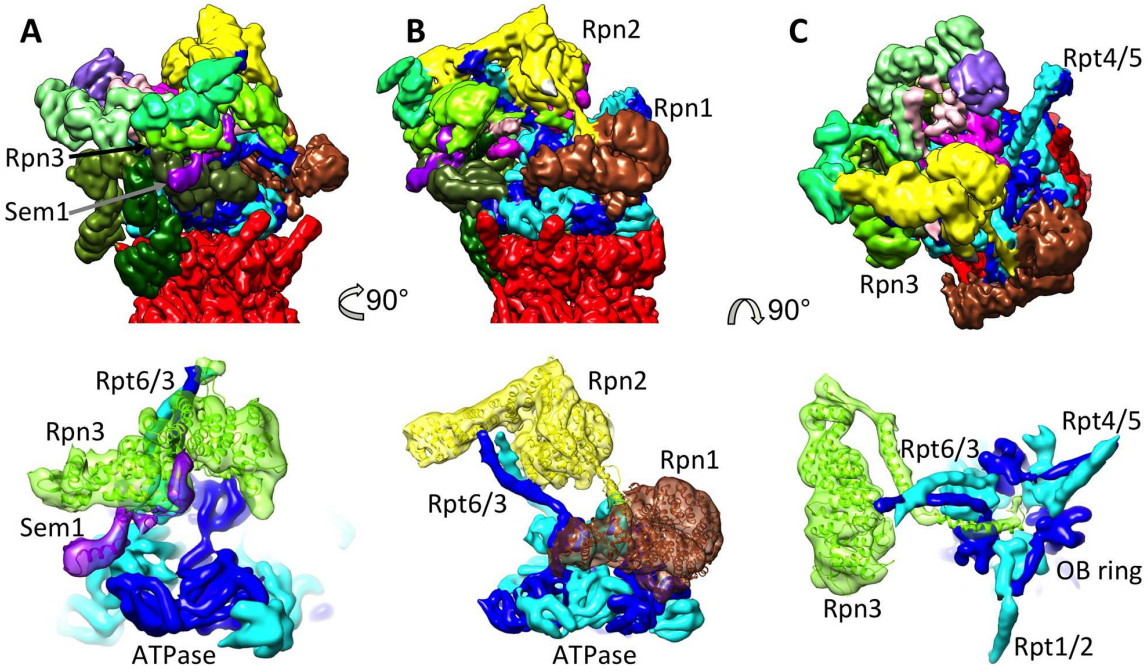

Figure 4.1.6: Previously unresolved features of the RP. The top row demonstrates the overall arrangement of the RP from the views used for the segmented close-ups in the bottom row depicting the interaction of Sem1 with Rpn3 (A), the connecting density between Rpn1 and Rpn2 (B) and the obstruction of the OB ring by the C-terminus of Rpn3 (C). Figure adapted from [Schweitzer et al., 2016].

As observed in a previous study of the isolated yeast lid [Dambacher et al., 2016], the helical bundle is the best resolved part of the lid (Figure 4.1.3 and Figure 4.1.5 D) and hence the least flexible. In contrast to the other PCI subunits, Rpn3 has, in addition to the helix entangled in the helical bundle, a segment at its very C-Terminus that is predicted to be a helix but could not be resolved in the isolated

yeast lid nor in the previous studies of the holocomplex [Unverdorben et al., 2014; Dambacher et al., 2016]. In the structure of the human 26S proteasome filtered to 7.7 Å, we could assign this C-terminal end of Rpn3 to a helix density, that protrudes parallel to the Rpt3/6 coiled coil into the mouth of the OB fold ring of the AAA module (Figure 4.1.6 C).

Organisation of the RP base subcomplex

The base subcomplex comprises the ATPase heterohexamer and 2 non-ATPases: Rpn1 and Rpn2 (section 1.2). The ATPase, which will be discussed in further detail in the next section, binds Rpn1 and Rpn2 through coiled-coils formed by the N-terminal helices of Rpt1/2 and Rpt3/6, respectively [Beck et al., 2012]. Rpn2 seems to function mainly as a binding scaffold between the lid subunits and the ATPase. In contrast, Rpn1 is positioned in a very exposed position and serves as a ubiquitin receptor and a hub for PIP binding (for details see section 1.2). In all previous reconstructions of the yeast 26S proteasome, the density of Rpn1 was completely separate from all other Rpn subunits. The overall improved SNR in the map of the human 26S proteasome reveals a connection between Rpn1 and Rpn2, which becomes particularly clear in the map filtered to 7.7 Å resolution (Figure 4.1.6 B). This connection is most likely formed by a helix in Rpn2 ranging from approximately Glu826 to Glu852, which would then attach to the interface between the N-terminal helix of Rpt2 (Gln57-Pro87) and Rpn1.

Structure of the AAA-ATPase subunits

The Rpt subunits in the base part of the RP assemble in an asymmetric 'split washer' within the heterohexamer [Lander et al., 2012]. All Rpts contain aromatic hydrophobic (Ar-Φ) 'pore loops', which project into the pore of the heterohexamer and have been suggested to pull the substrate into the CP [Nyquist and Martin, 2014]. The split-washer positioning of the Rpt subunits causes an arrangement of the pore loops in a spiral staircase. Whereas in previous intermediate-resolution studies the positions of the Ar-Φ pore loops could only be inferred from the fitted structures of Rpt homologs, the high-resolution structure reveals the Ar-Φ pore loops directly (Figure 4.1.7 A). Five of the six Ar-Φ pore loops form a remarkably accurate spiral staircase (Rpt3, -4, -5, -1 and -2, ordered by decreasing elevation). However, the Ar-Φ pore loop of the sixth Rpt, Rpt6, is positioned in-between.

Interestingly, Rpt6 not only deviates from its neighbours in terms of the positioning of the Ar-Φ pore- loop but also in other structural aspects. A comparison of the

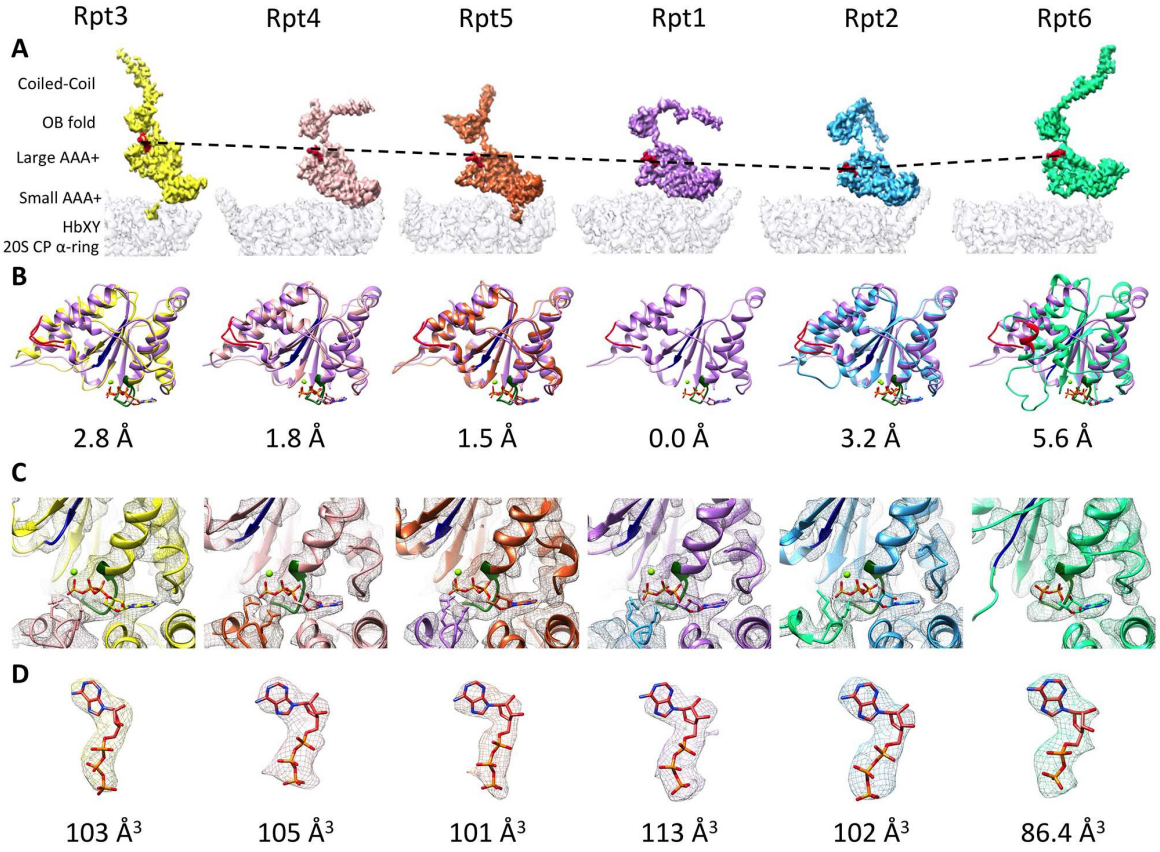

Figure 4.1.7: Organisation of the ATPase. (A) Segmented densities of the Rpt subunits rotated successively in 60° steps around the CP axis. The Ar-Φ pore loops are shown in red. (B) Structural comparison of each AAA+ domain with Rpt1 (dark green: Walker A, dark blue: Walker B, red: poor loop). The root mean square deviation of the respective AAA+ domain with that of Rpt1 is given below each panel. (C) Close-ups on the nucleotide binding sites at the Walker A motives (green) showing the nucleotides, coordinated Mg^{2+} and Arg-fingers of the neighbouring subunits. (D) Segmented densities of the nucleotides bound to the respective Rpt subunit and the modelled nucleotides. The volume of the respective nucleotide density, obtained from the difference map (Figure 4.1.8) is given below each panel. Figure adapted from [Schweitzer et al., 2016].

large AAA+ subdomains of the Rpt-subunits shows that, whereas the other Rpts share a highly similar structure of this domain, Rpt6 deviates significantly (Figure 4.1.7 B). Many secondary structure elements are displaced with respect to their counterparts in the other Rpts. Most notably, the Ar-Φ pore loop orients differently and adopts a partially helical fold. This helix forms pronounced hydrophobic contacts to a small helix at the N terminus of the large AAA+ domain (Leu219-Val140, Val220-Leu137, Phe223-Pro133). Due to its fold the Rpt6 pore loop does not protrude into the pore, which is nicely in line with Rpt6 not being part of the staircase.

In comparison with the crystal structure of the archaeal homolog PAN [Zhang et al., 2009a], none of the Rpts share the β-strand positioned at the N terminus of

the PAN AAA+ domain. As clearly visible from the density of the human 26S proteasome, the corresponding segments form short helices or a loop (Rpt3). A possible explanation for the occurrence of the β-strand formation and its integration in the adjacent β-sheet in PAN, is the truncation of the large AAA subunit in the construct for the crystal structure.

Nucleotide loading of the AAA-ATPase

As described in section 1.2, the binding and hydrolysis of nucleotides is vital for the functioning of AAA-ATPases. Each Rpt subunit in the 26S harbours a nucleotide binding site formed by the Walker A and Walker B motive. The binding of ATP to the Rpts is further stabilised by two arginine (Arg) fingers positioned in the AAA chain of the neighbouring Rpt subunit. As a consequence to the overall split washer arrangement of the Rpts, only five of the six Arg–finger motifs interact with bound ATP. In the s1 state, the Arg–fingers of Rpt3 cannot reach into the binding site of Rpt6 [Sledz et al., 2013].

The limited resolution of previous studies has prevented the detection of nucleotides. Inspection of the cryo-EM map at 3.9 Å shows clear extra densities at all nucleotide binding sites, which also become apparent in a difference map between the experimental density and a density simulated from the model of the Rpts (Figure 4.1.8). All extra densities are clearly of the approximate size and shape of the

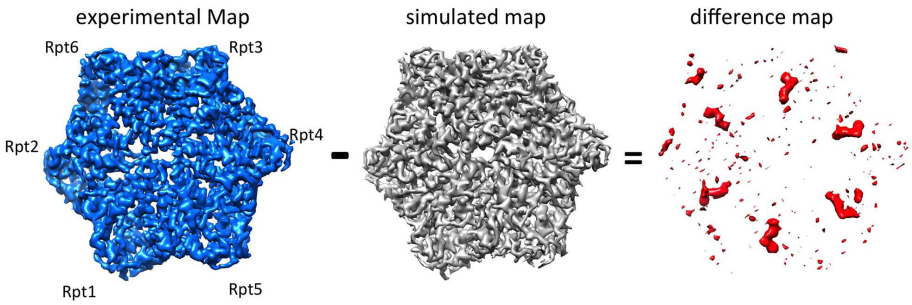

Figure 4.1.8: Visualisation of the bound nucleotides. Subtraction of the density simulated from an atomic model without nucleotides (grey) from the cryo-EM reconstruction (blue) yields the density of the nucleotides (red). Figure adapted from [Schweitzer et al., 2016].

binding nucleotides ATP and ADP (Figure 4.1.7 C). The nucleotide density bound to Rpt6 is the smallest and can be assigned to ADP (Figure 4.1.7 C). The finding of ADP binding at this site agrees well with the fact that in the s1 state the Arg–fingers of Rpt3 cannot engage with the nucleotide binding site of Rpt6. The other five nucleotide densities are significantly larger than the one bound to Rpt6 and the binding of the two Arg–fingers can be clearly observed. Therefore, we tentatively

assigned them to ATP. However, they could also arise from an ADP-Pi intermediate state or an overlay of ATP and ADP. An unambiguous assignment will require a higher-resolution structure.

The AAA-CP interface and the CP

Three of the six AAA-ATPase subunits (Rpt2, Rpt3 and Rpt5) share a C-terminal motif, formed by a hydrophobic residue (Hb), a tyrosine and a residue of any type (HbYX). These HbYX motifs, which are absent in the other three Rpt subunits, can bind to pockets in the α-ring of the CP [Smith et al., 2007] (for details see section 1.2). In the high-resolution density of the human 26S proteasome the C-termini of Rpt3 and Rpt5 are clearly resolved. Bulky side chains can be discerned, allowing for an accurate placement of the two HbYX motifs (Figure 4.1.9). In contrast, the C-

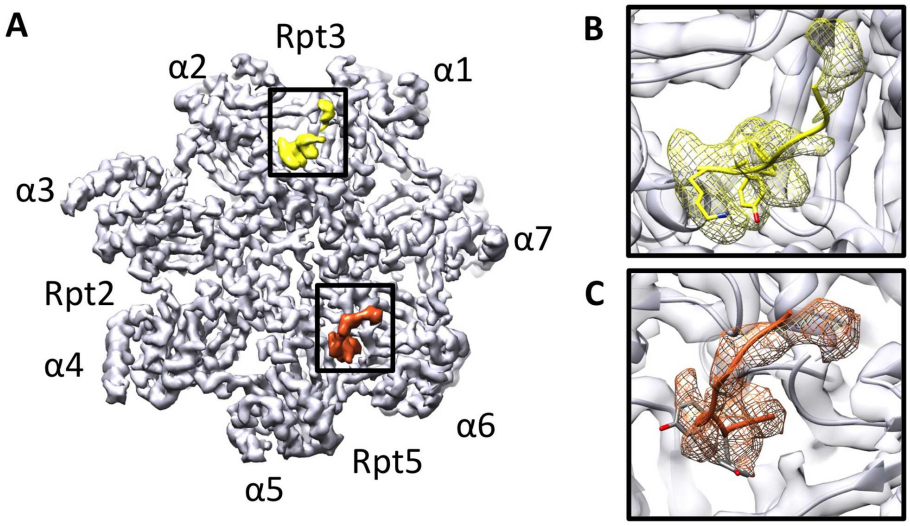

Figure 4.1.9: The HbXY motives of Rpt3 and Rpt5 bind to the respective binding pockets of the α-ring. (A) Segmented HbXY motives of Rpt3 (yellow) and Rpt5 (orange). (B) Model of the Rpt3 HbXY motif located in the pocket formed by α_1 and α_2. (C) Model of the Rpt5 HbXY motif located in the pocket formed by α_5 and α_6. Figure adapted from [Schweitzer et al., 2016].

terminus of Rpt2 cannot be detected, indicating structural flexibility. For the yeast 26S proteasome, also one HbYX motif was found to be flexible, but it was the C-terminus of Rpt5 [Tian et al., 2011; Beck et al., 2012].

It has been suggested that the binding of HbYX motifs to the pockets in the α-ring causes opening of the CP gate [Smith et al., 2007]. However, comparing the high-resolution reconstruction with the crystal structure of the isolated bovine CP with a closed gate [Unno et al., 2002], they show no remarkable differences. Espe-

cially, no indications of gate opening can be identified in the high-resolution reconstruction. Although this stands in contrast to a low-resolution negative stain study [Da Fonseca and Morris, 2008], it agrees with all intermediate-resolution cryo-EM structures of the yeast 26S proteasome [Luan et al., 2016; Lander et al., 2012; Lasker et al., 2012; Beck et al., 2012; Unverdorben et al., 2014] and was confirmed by a high-resolution structure of the human 26S proteasome that appeared after our structure was published [Huang et al., 2016].

4.2 Discussion

4.2.1 Advantages of the developed image processing workflow

The state-of-the-art software to process single-particle data from DED cameras is RELION [Scheres, 2012a]. In order to make use of the methods implemented in RELION for the 26S proteasome, a variety of challenges had to be met as outlined in subsection 4.1.1.

The preferred orientation on the grid and conformational heterogeneity requires acquisition of a high quantity of particles to achieve high-resolution. The relatively large size of the complex (∼50 nm in length) combined with the need for a small pixel size (1.35 Å) lead to a box size of nearly 400x400 pixels (see subsection 2.4.2). The combination of these two requirements is very demanding in terms of memory for refinement and polishing in RELION. Therefore, it is necessary to reduce the dataset to make the polishing computationally feasible in a reasonable amount of time. Thorough evaluation showed that the protocol, developed for discarding particles, did not significantly reduce the overall achieved resolution (Figure 4.1.1).

The other major challenge of the dataset is due to the uncorrelated nature of the RP conformations, breaking the C2 symmetry of the 26S proteasome [Unverdorben et al., 2014]. A cryo-EM study of the human 26S proteasome, published shorly after ours, did not take the broken symmetry into account and applied C2-symmetry throughout classification and refinement [Huang et al., 2016]. Although the structure of this study was refined to an average resolution of 3.5 Å and confirmed our findings on the ATPase and the CP, none of the insights we obtained for the Rpn subunits were observed. This missing information can be explained by the fact that a classification under applied C2-symmetry does not allow the separation of s1- and s2-like RPs. Averaging over the conformational difference between the s1 and s2 state, a lever-like movement anchored at the ATPase, causes smeared out densities for the distant Rpn subunits. Therefore, a seperate treatment of the RPs is

particularly useful for deciphering the structural arrangement of the Rpn subunits.

The *in-silico* separation of the RPs as described in [Beck et al., 2012] was implemented for the RELION metadata format and the subsequent steps of refinement and classification in RELION were adapted (subsection 2.4.2). The *in-silico* separation enables us to group the particles with respect to differences on the RP level by classification with a mask on one half of the 26S proteasome. In RELION, given masks are applied to the 3D volumes but not to the 2D particles, which may lead to erroneous alignments, as the algorithm tries to include more density in the masked area, known as 'moving target artefacts'. This can lead to classification according to the artefacts rather than the conformational differences. Therefore, we had to keep the alignment fixed, which limits the accuracy of the classification. However, since the overall reconstruction before classification is clearly s1-like and does not show indications of other states (Figure S2 in [Schweitzer et al., 2016]), it can be assumed that most of the particles are in an s1-like conformation and that the angular alignment is highly accurate for RP particles in this state. Thus, the performed classification was anticipated to be suitable for the selection of well-aligning RPs in the s1 state, which is confirmed by the improved reconstruction after classification (subsection 4.1.1).

Although the overall quality of the reconstruction improves through classification, the local resolution remains heterogeneous (Figure 4.1.3 A). This indicates that the s1 state has small-scale variability within the RP, which can not be eliminated by the developed classification method, limiting the resolution in these parts of the RP to an intermediate level. In order to obtain a more homogeneous resolution and a high-resolution structure of the outer parts of the RP, further improvements will be needed. Either a classification method must be developed, which allows to distinguish these small differences, or the RP needs to be stabilised by biochemical means (see chapter 5).

4.2.2 Structural insights into the RP organisation

Although the lid and also the base subunits Rpn1 and Rpn2 are only resolved at intermediate resolution (Figure 4.1.3), the higher overall quality of the map provides new insights into some details, which helped to complement the atomic model of the 26S proteasome. The biggest improvements were achieved for Rpn3, Rpn2 and Sem1 (section 4.1.4).

The C-terminal helix of Rpn3, missing in previous structures, was identified to protrude into the mouth of the OB fold ring of the AAA module (Figure 4.1.6 C).

This position is in an area, which has previously been suggested to be a composite active site, where substrate deubiquitylation and unfolding occurs [Pathare et al., 2014]. Therefore, the C-terminal helix of Rpn3 may be a sensor for a substrate engaged by the OB mouth. Through its connection to the helical bundle, Rpn3 might induce the conformational change of the lid subunits required for the activation of Rpn11 and hence the composite active site [Matyskiela et al., 2013; Sledz et al., 2013]. Consistent with this hypothesis, the C-terminal helix of Rpn3 locates in close proximity to the region in Rpn11 (Ile163 to His199) which has been proposed to function as a trigger for substrate recognition [Pathare et al., 2014]. In the X-ray structures of the isolated Rpn8/Rpn11 dimer [Pathare et al., 2014; Worden et al., 2014] this region was not resolved, indicating flexibility of the respective residues in the isolated context. In contrast, the region is resolved in the high-resolution structure of the 26S holocomplex, most likely due to stabilisation by Rpn2 and Rpn3.

The connection between Rpn1 and Rpn2, identified from the map filtered to 7.7 Å, was determined to result from an insertion in Rpn2 (section 4.1.4, Figure 4.1.6 B). This insertion forms a connection with Rpn1 and the N-terminal helix of Rpt2 and may, thereby, stabilise the base subcomplex and facilitate coordination of rotational motions of Rpn1 and all other Rpn subunits during transition between the different conformational states (s1, s2 and s3).

In conclusion, both previously unresolved helices in Rpn2 and Rpn3 most likely have coordinating roles during the process of substrate degradation by the 26S proteasome.

4.2.3 Nucleotide loading of the ATPase and the connection of the ATPase to the CP

The high-resolution allowed us to identify nucleotides bound to all six ATPase subunits. This finding was confirmed by the study from [Huang et al., 2016]. Full occupancy of nucleotides has been observed in crystal structures of some prokaryotic homologs of the Rpts [Trame and McKay, 2001; Sauer and Baker, 2011]. However, this full nucleotide loading has been considered unphysiological and mechanistic models of the ATPase functioning assume a maximal occupancy of four nucleotides for the hexamer in solution [Sauer and Baker, 2011; Smith et al., 2011]. The full occupancy of nucleotides of the 26S proteasome in the presence of an excess of ATP provides evidence that either these models must be revised or that the mechanisms in the 26S proteasome differ from those in its simpler prokaryotic counterparts.

Only one Rpt was found to bind ADP, namely Rpt6. Interestingly, this difference

in nucleotide binding correlates with a number of structural peculiarities of Rpt6, the most pronounced being the Ar-Φ pore loop, which does not protrude into the channel of the ATPase (section 4.1.4). The unique structure of Rpt6 might be caused by the nucleotide binding state. However, from this study we cannot exclude that structural differences also arise from its sequence. Further high-resolution structures of the 26S proteasome in the s3 state will be needed to address the reasons for the unique structure of Rpt6.

When looking at the HbYX motifs of Rpt2, -3 and -5, which form the connection between the ATPase and the CP, only Rpt3 and Rpt5 show densities corresponding to this motif (Figure 4.1.9), indicating that the HbYX motif of Rpt2 remains flexible. This finding, which is in line with the finding from [Huang et al., 2016], is rather surprising, as Rpt2 is most proximal to the CP in the split-washer arrangement. The unbound HbYX motif of Rpt2 might facilitate motions of the AAA module on the CP α-ring during the conformational changes of the 26S proteasome. To validate this hypothesis further studies including high-resolution structures of other states are required.

5 Conclusion and Outlook

This work furthers the mechanistic understanding of the function and regulation of the 26S proteasome through SP cryo-EM studies. The 3D maps of the 26S–Ubp6 complex in presence and absence of UbAld constitute the first structural investigation of the complete 26S proteasome in complex with a PIP. Beyond the mode of interaction of Ubp6 with the 26S holocomplex, it reveals the influence of Ubp6 on the conformational landscape of the 26S proteasome (subsection 3.1.3). In the second part of this work, a workflow was implemented, which is tailored to the peculiarities of the 26S proteasome and DED data. Applying this workflow to an SP cryo-EM dataset of the human 26S proteasome resulted in a 3D structure at an average resolution of 3.9 Å (subsection 4.1.1), which allowed building an atomic model that is highly accurate for most parts of the complex (subsection 4.1.3).

Due to the heterogeneous resolution of the human 26S proteasome structure, the atomic model is less reliable in the peripheral parts of the complex than in the CP, the ATPase and the helical bundle. Improving the resolution in the lower-resolved areas would allow building a model that is accurate on the side chain level for the entire complex.

Additionally, structural studies of inhibitors binding to 26S proteasome enzymes would further the understanding of their functioning on a molecular level. Examples of identified inhibitors are compounds that inhibit Ubp6 [Lee et al., 2010] and β_5 [Neilsen et al., 2013; Schrader et al., 2016]. Whereas structures of the 20S with bound inhibitors have been reported [da Fonseca and Morris, 2015; Schrader et al., 2016], the influence of inhibitors on the 26S proteasome holocomplex has not been studied structurally. A detailed structural dissection of inhibitor-binding would require higher resolution than obtained in this study.

Several measures could be employed to improve the resolution that was obtained within the context of this thesis. Firstly, data can be acquired at higher magnification [Merk et al., 2016], i.e. smaller pixel size on the specimen level, leading to a higher Nyquist frequency. This results in an increase of the DQE value, i.e. the signal, for a respective frequency compared to lower magnification. Secondly, a low dose rate is critical for further optimisation of the DQE and thereby the SNR.

Thirdly, in this resolution range, the optimisation of the coma-free alignment should be carried our with even higher precision than done in this study, as coma induces artefacts to high-resolution information. Finally, stabilisation of the RP by biochemical means would help to overcome the locally varying resolution (Figure 4.1.3 A).

Additionally, in order to reduce the heterogeneity of the resolution, it would be beneficial to have a classification method, which can accurately align the particles during a focused classification (in contrast to keeping the alignment parameters constant as done here, subsection 4.1.1). One possibility to accomplish the simultaneous alignment and focused classification is to subtract the density outside the masked area from the particle images prior to classification. This approach has been implemented in RELION [Bai et al., 2015]. However, when applied to the human 26S dataset, the subtraction led to substantial artefacts, prohibiting a successful classification. Therefore, in order to use this approach the subtraction protocol needs to be improved.

The results on the 26S–Ubp6–UbAld complex suggest a route for stabilisation of the RP and hence improving the homogeneity of the resolution. The data acquired for this project in the presence of ATP indicate that the addition of UbAld improves the overall sample quality: The number of intact particles on the cryo-EM grids increased (data not shown). Additionally, purification of 26S proteasomes in the presence of ATP-γS or in particular AMP-PNP may stabilise the 26S–Ubp6–UbAld complex further ([Bashore et al., 2015], personal communication with Marc Wehmer). These non-hydrolysable ATP analogues induce the s3 conformation, which allows the interaction of Ubp6 with Rpt1. Such a stabilisation in combination with DED data acquisition, optimised for the highest amount of signal, will likely result in a high-resolution structure of more homogeneous resolution.

In addition to reducing resolution heterogeneity of the 26S proteasome, higher resolution information of the 26S proteasome in complex with Ubp6 are of interest, as the *in-situ* structure of the substrate processing (s3-like) state includes an extra density partially explained by Ubp6 (section 3.2.2, [Asano et al., 2015]). Such a high-resolution structure would also provide more detailed information on the residues mediating the interaction between Ubp6 and the 26S holocomplex.

Apart from Ubp6, there is a variety of PIPs, which interact with the 26S proteasome during the degradation process (section 1.3). The extra density in the *in-situ* structure of the substrate processing state of the 26S proteasome is not fully explained by Ubp6 and, therefore, suggests that several PIPs act in concert to assist substrate processing at the RP ([Asano et al., 2015], Figure 3.2.2). Many PIPs are predicted to be largely unstructured [Aufderheide et al., 2015b] and would there-

fore average out in a cryo-EM reconstructions. Based on the analysis in [Aufderheide et al., 2015b], the most prominent candidates to cause the unexplained part of the density are the substoichiometric subunit Rpn13, the PIP UCH37 and perhaps parts of the PIPs Dsk2 and Hul5. SP cryo-EM studies of these PIPs and the human or mammalian 26S proteasome, stabilised in the substrate processing state (e.g. by using AMP-PNP), could identify this extra density completely and would help to provide clues on how PIPs assist the degradation process.

Furthermore, a substrate could be added *in-vitro* to purified 26S proteasomes for visualisation in the presence of different combinations of PIPs. The resulting reconstructions would constitute snapshots of PIP-assisted substrate processing, which could be compared to the results from the *in-situ* study [Asano et al., 2015] in order to unravel the role of PIPs during the proteasomal degradation process under physiological conditions.

A Appendix

Abbreviations

2D	=	two-dimensional
3D	=	three-dimensional
AAA	=	ATPases associated with diverse cellular activities
ADP	=	adenosine diphosphate
Ar-Φ	=	hydrophobic aromatic
Arg	=	arginine
ATP	=	adenosine triphosphate
CCD	=	charge-coupled device
CET	=	cryo-electron tomography
CP	=	core particle (20S proteasome)
CPh	=	creatine phosphate
CPK	=	creatine phosphate kinase
cryo-EM	=	cryo-electron microscopy
CTF	=	contrast transfer function
dc26S	=	double-capped 26S proteasome
DED	=	direct electron detector
DQE	=	detective quantum efficiency
DTT	=	dithiothreitol
DUB	=	deubiquitylating enzyme
E1	=	ubiquitin-activating enzyme
E2	=	ubiquitin-conjugating enzyme
E3	=	ubiquitin-ligase
E.coli	=	*Escherichia coli*
eIF3	=	eukaryotic translation initiation factor 3
EM	=	electron microscopy
EMDB	=	Electron Microscopy Data Bank
FCR	=	Fourier cross resolution

FEG = field emission gun
FIB = focused ion beam
FSC = Fourier shell correlation
GGL-AMC = glycine-glycine-leucine-7-amido-4-methylcoumarin
HbYX = hydrophobic-tyrosine-any amino acid tripeptide
HECT = Homology to E6AP C Terminus
JAMM = JAB1/MPN/Mov34 metalloenzyme
MAP = maximum a posteriori
MDFF = Molecular Dynamics Flexible Fitting, plugin for VMD
ML = maximum likelihood
MPN = Mpr1/Pad1 N-terminal
MTF = modulation transfer function
Ntn = N-terminal nucleophilic
OB = oligosaccharide binding
PC = proteasome/cyclosome
PCA = principle component analysis
PCI = proteasome, COP9 signalosome, eIF3 translation initiation complex
PDB = Protein Data Bank
PIP = proteasome interacting protein
PRU = pleckstrin-like receptor for ubiquitin
PSF = point spread function
RING = Really Interesting New Gene
RP = regulatory particle
Rpn = regulatory particle non-ATPase
Rpt = regulatory particle tripleA-ATPase
$Rpt1_{OB}$ = OB domain of Rpt1
S. cerevisiae = *Saccharomyces cerevisiae*
sc26S = single-capped 26S proteasome
SDS-PAGE = sodium dodecyl sulfate polyacrylamide gel electrophoresis
SEM = scanning electron microscope
SNR = signal-to-noise ratio
SP cryo-EM = single-particle cryo-electron microscopy
SPA = single-particle analysis
SSNR = spectral signal-to-noise ratio
sUbR = shuttling Ub-receptors
TEM = transmission electron microscope

Ub	=	ubiquitin
Ub-AMC	=	ubiquitin-7-amido-4-methylcoumarin
UbAld	=	ubiquitin aldehyde
UBL	=	ubiquitin-like
Ubp6	=	ubiquitin-specific protease 6 (Usp14 in human)
$Ubp6_{USP}$	=	USP domain of Ubp6, residues 104-499
UbVS	=	ubiquitin vinyl sulfone
UCH	=	ubiquitin C-terminal hydrolase
UIM	=	ubiquitin-interacting motif
UPS	=	ubiquitin-proteasome-system
USP	=	ubiquitin-specific protease
Usp14	=	ubiquitin-specific protease 14 (Ubp6 in yeast)
$Usp14_{USP}$	=	USP domain of Usp14
VMD	=	Visual Molecular Dynamics, program for the visualisation of molecular systems
WPA	=	weak phase approximation
WT	=	wild type
XL-MS	=	cross-linking mass spectrometry
YPD	=	yeast extract peptone dextrose

Constants and designations

Table A.1: Constants and units

Constants and units		
speed of light	c	$= 2.9979 \cdot 10^{8}\,\mathrm{m\,s^{-1}}$
Planck constant	h	$= 6.626 \cdot 10^{-34}\,\mathrm{J\,s}$
		$= 4.136 \cdot 10^{-15}\,\mathrm{eV\,s}$
elementary charge	e_0	$= 1.602 \cdot 10^{-19}$
rest mass	m_0	$= 9.1091 \cdot 10^{-31}\mathrm{kg}$
rest energy	E_0	$= 8.14 \cdot 10^{-14}$ J
		$= 511$ keV

Table A.2: Used designation of variables

variable	designation	comment
kinetic energy	E	$1\,\mathrm{eV} = 1.602 \cdot 10^{-19}\mathrm{J}$
energy loss	ΔE	e.g. through inelastic scattering
wave length	λ	
position vector	$\mathbf{r}$	$\mathbf{r}$ = (x,y,z)
momentum	p	$= \lvert\mathbf{p}\rvert$
velocity	v	$= \lvert\mathbf{v}\rvert$
mass	m	
scattering cross section	ρ	
mean free path	Λ	$\Lambda = 1/\rho$
angular aperture	α	
resolving power	d	[length]
spatial frequency	k	$= \lvert\mathbf{k}\rvert = \lvert(kx, ky)\rvert$; [1/length]
aperture function	$A(\mathbf{k})$	
spherical-aberration coefficient	C_s	
chromatic-aberration coefficient	C_c	
contrast	C	
intensity	I	see Equation 1.17 and Equation 1.8
wave function	$\Psi(\mathbf{r})$	
Coulomb potential	$V(\mathbf{r})$	
phase shift (upon scattering)	Φ	
phase shift (induced by TEM)	γ	see Equation 1.12
defocus	Δz	
scattering angle	θ	
Fourier transform	$\mathcal{F}$	
inverse Fourier transform	$\mathcal{F}^{-1}$	
envelope function	$E(\mathbf{k})$	
aberration function	$B(\mathbf{k})$	
ratio of amplitude and phase contrast	$Q(\mathbf{k})$	approximated to be constant Q_0

Bibliography

P. D. Adams, R. W. Grosse-Kunstleve, L.-W. Hung, T. R. Ioerger, A. J. McCoy, N. W. Moriarty, R. J. Read, J. C. Sacchettini, N. K. Sauter, and T. C. Terwilliger. PHENIX: building new software for automated crystallographic structure determination. *Acta Crystallographica Section D Biological Crystallography*, 58(11):1948–1954, nov 2002. ISSN 0907-4449.

K. Aoyama, F. Zühl, T. Tamura, and W. Baumeister. 2-D Crystallization of the Rhodococcus 20S Proteasome. *Journal of Structural Biology*, 116(3):438–442, may 1996. ISSN 10478477.

S. Asano. *Electron CryoTomography Studies of Mammalian Neurons*. PhD thesis, Technische Universität München, 2015.

S. Asano, Y. Fukuda, F. Beck, A. Aufderheide, F. Forster, R. Danev, and W. Baumeister. Proteasomes. A molecular census of 26S proteasomes in intact neurons. *Science*, 347(6220):439–442, 2015.

A. Aufderheide, F. Beck, F. Stengel, M. Hartwig, A. Schweitzer, G. Pfeifer, A. L. Goldberg, E. Sakata, W. Baumeister, and F. Förster. Structural characterization of the interaction of Ubp6 with the 26S proteasome. *Proceedings of the National Academy of Sciences of the United States of America*, 112(28):8626–31, jul 2015a. ISSN 1091-6490.

A. Aufderheide, P. Unverdorben, W. Baumeister, and F. Förster. Structural disorder and its role in proteasomal degradation. *FEBS Letters*, 589(19PartA):2552–2560, sep 2015b. ISSN 00145793.

X.-C. Bai, G. McMullan, and S. H. W. Scheres. How cryo-EM is revolutionizing structural biology. *Trends in Biochemical Sciences*, 40(1):49–57, jan 2014. ISSN 13624326.

X.-C. Bai, E. Rajendra, G. Yang, Y. Shi, and S. H. Scheres. Sampling the conformational space of the catalytic subunit of human γ-secretase. *eLife*, 4(6178):e11182, mar 2015. ISSN 2050-084X.

L. A. Baker and J. L. Rubinstein. *Radiation damage in electron cryomicroscopy*, volume 481. Elsevier Masson SAS, 2010. ISBN 9780123749062.

C. Bashore, C. M. Dambacher, E. A. Goodall, M. E. Matyskiela, G. C. Lander, and A. Martin. Ubp6 deubiquitinase controls conformational dynamics and substrate degradation of the 26S proteasome. *Nature structural & molecular biology*, 22(9): 712–9, sep 2015. ISSN 1545-9985.

W. Baumeister and A. C. Steven. Macromolecular electron microscopy in the era of structural genomics, dec 2000. ISSN 09680004.

W. Baumeister, R. Grimm, and J. Walz. Electron tomography of molecules and cells, feb 1999. ISSN 09628924.

F. Beck, P. Unverdorben, S. Bohn, A. Schweitzer, G. Pfeifer, E. Sakata, S. Nickell, J. M. Plitzko, E. Villa, W. Baumeister, and F. Förster. Near-atomic resolution structural model of the yeast 26S proteasome. *Proceedings of the National Academy of Sciences of the United States of America*, 109(37):14870–14875, 2012.

D. Berko, S. Tabachnick-Cherny, D. Shental-Bechor, P. Cascio, S. Mioletti, Y. Levy, A. Admon, T. Ziv, B. Tirosh, A. L. Goldberg, and A. Navon. The Direction of Protein Entry into the Proteasome Determines the Variety of Products and Depends on the Force Needed to Unfold Its Two Termini. *Molecular cell*, 2012.

C. E. Berndsen and C. Wolberger. New insights into ubiquitin E3 ligase mechanism. *Nature structural & molecular biology*, 21(4):301–307, 2014.

A. Beskow, K. B. Grimberg, L. C. Bott, F. A. Salomons, N. P. Dantuma, and P. Young. A conserved unfoldase activity for the p97 AAA-ATPase in proteasomal degradation. *Journal of molecular biology*, 394(4):732–746, 2009.

S. Bohn, F. Beck, E. Sakata, T. Walzthoeni, M. Beck, R. Aebersold, F. Förster, W. Baumeister, and S. Nickell. Structure of the 26S proteasome from Schizosaccharomyces pombe at subnanometer resolution. *Proceedings of the National Academy of Sciences of the United States of America*, 107(49):20992–20997, 2010.

S. Bohn, E. Sakata, F. Beck, G. R. Pathare, J. Schnitger, I. Nagy, W. Baumeister, and F. Förster. Localization of the regulatory particle subunit Sem1 in the 26S proteasome. *Biochemical and biophysical research communications*, 435(2):250–254, 2013.

C. Booth and P. Mooney. Applications of electron-counting direct-detection cameras in high- resolution cryo-electron microscopy. *Microscopy and Analysis*, 27(6):13–21, 2013.

L. Borissenko and M. Groll. 20S proteasome and its inhibitors: crystallographic knowledge for drug development. *Chemical reviews*, 107(3):687–717, 2007.

A. Borodovsky, B. M. Kessler, R. Casagrande, H. S. Overkleeft, K. D. Wilkinson, and H. L. Ploegh. A novel active site-directed probe specific for deubiquitylating enzymes reveals proteasome association of USP14. *The EMBO journal*, 20(18): 5187–5196, 2001.

G. Cardone, J. B. Heymann, and A. C. Steven. One number does not fit all: mapping local variations in resolution in cryo-EM reconstructions. *Journal of structural biology*, 184(2):226–236, 2013.

S. Chen, G. McMullan, A. R. Faruqi, G. N. Murshudov, J. M. Short, S. H. Scheres, and R. Henderson. High-resolution noise substitution to measure overfitting and validate resolution in 3D structure determination by single particle electron cryomicroscopy. *Ultramicroscopy*, 135:24–35, 2013.

X. Chen, B. H. Lee, D. Finley, and K. J. Walters. Structure of proteasome ubiquitin receptor hRpn13 and its activation by the scaffolding protein hRpn2. *Molecular cell*, 38(3):404–415, 2010.

B. Crosas, J. Hanna, D. S. Kirkpatrick, D. P. Zhang, Y. Tone, N. A. Hathaway, C. Buecker, D. S. Leggett, M. Schmidt, R. W. King, S. P. Gygi, and D. Finley. Ubiquitin chains are remodeled at the proteasome by opposing ubiquitin ligase and deubiquitinating activities. *Cell*, 127(7):1401–1413, 2006.

P. C. da Fonseca, J. He, and E. P. Morris. Molecular model of the human 26S proteasome. *Molecular cell*, 46(1):54–66, 2012.

P. C. A. Da Fonseca and E. P. Morris. Structure of the human 26S proteasome: Subunit radial displacements open the gate into the proteolytic core. *Journal of Biological Chemistry*, 283(34):23305–23314, aug 2008. ISSN 00219258.

P. C. A. da Fonseca and E. P. Morris. Cryo-EM reveals the conformation of a substrate analogue in the human 20S proteasome core. *Nature communications*, 6 (May):7573, 2015. ISSN 2041-1723.

C. M. Dambacher, E. J. Worden, M. A. Herzik, A. Martin, and G. C. Lander. Atomic structure of the 26S proteasome lid reveals the mechanism of deubiquitinase inhibition. *eLife*, 5(January):1–17, 2016. ISSN 2050-084X.

W. J. de Ruijter and J. K. Weiss. Methods to measure properties of slow-scan CCD cameras for electron detection. *Review of Scientific Instruments*, 63(10):4314, 1992. ISSN 00346748.

J. Dubochet, M. Adrian, J. J. Chang, J. C. Homo, J. Lepault, A. W. McDowall, and P. Schultz. Cryo-electron microscopy of vitrified specimens. *Quarterly reviews of biophysics*, 21(2):129–228, may 1988. ISSN 0033-5835.

S. Elsasser, R. R. Gali, M. Schwickart, C. N. Larsen, D. S. Leggett, B. Muller, M. T. Feng, F. Tubing, G. A. Dittmar, and D. Finley. Proteasome subunit Rpn1 binds ubiquitin-like protein domains. *Nature cell biology*, 4(9):725–730, 2002.

P. Emsley, B. Lohkamp, W. G. Scott, and K. Cowtan. Features and development of Coot. *Acta Crystallographica Section D Biological Crystallography*, 66(4):486–501, apr 2010. ISSN 0907-4449.

H. Engelhard. Elektronenmikroskopie. In F. Lottspeich and J. W. Engels, editors, *Bioanalytik*, chapter 18, pages 461–494. Spektrum Akademischer Verlag Elservier München, München, 2 edition, 2006.

E. Estrin, J. R. Lopez-Blanco, P. Chacon, and A. Martin. Formation of an intricate helical bundle dictates the assembly of the 26S proteasome lid. *Structure*, 21(9): 1624–1635, 2013.

D. Finley. Recognition and processing of ubiquitin-protein conjugates by the proteasome. *Annual review of biochemistry*, 78:477–513, 2009.

D. Finley, H. D. Ulrich, T. Sommer, and P. Kaiser. The ubiquitin-proteasome system of Saccharomyces cerevisiae. *Genetics*, 192(2):319–360, 2012.

F. Förster, K. Lasker, F. Beck, S. Nickell, A. Sali, and W. Baumeister. An atomic model AAA-ATPase/20S core particle sub-complex of the 26S proteasome. *Biochemical and biophysical research communications*, 388(2):228–233, 2009.

F. Förster, K. Lasker, S. Nickell, A. Sali, and W. Baumeister. Toward an Integrated Structural Model of the 26S Proteasome. *Molecular & Cellular Proteomics*, 9(8): 1666–1677, aug 2010. ISSN 1535-9476.

F. Förster, E. Villa, D. Thomas, A. Korinek, and W. Baumeister. 1.14 Structure Determination of Macromolecular Complexes by Cryo-Electron Microscopy in vitro and in situ. In *Comprehensive Biophysics*, volume 1, pages 245–276. Elsevier, 2012.

F. Förster, P. Unverdorben, P. Sledz, and W. Baumeister. Unveiling the Long-Held Secrets of the 26S Proteasome. *Structure*, 21(9):1551–1562, 2013.

F. Förster, J. M. Schuller, P. Unverdorben, and A. Aufderheide. Emerging mechanistic insights into AAA complexes regulating proteasomal degradation. *Biomolecules*, 4(3):774–794, 2014.

J. Frank. Single-particle reconstruction of biological macromolecules in electron microscopy - 30 years. *Quarterly Reviews of Biophysics*, 42(03):139, aug 2009. ISSN 0033-5835.

J. J. Frank. *Three-dimensional electron microscopy of macromolecular assemblies visualization of biological molecules in their native state*. Oxford University Press, 2 edition, 2006. ISBN 9780195182187.

M. Funakoshi, X. Li, I. Velichutina, M. Hochstrasser, and H. Kobayashi. Sem1, the yeast ortholog of a human BRCA2-binding protein, is a component of the proteasome regulatory particle that enhances proteasome stability. *Journal of cell science*, 117(Pt 26):6447–54, dec 2004. ISSN 0021-9533.

R. M. Glaeser. Review: electron crystallography: present excitement, a nod to the past, anticipating the future. *Journal of structural biology*, 128(1):3–14, dec 1999. ISSN 1047-8477.

M. H. Glickman and A. Ciechanover. The ubiquitin-proteasome proteolytic pathway: destruction for the sake of construction. *Physiological reviews*, 82(2):373–428, apr 2002. ISSN 0031-9333.

M. H. Glickman, D. M. Rubin, O. Coux, I. Wefes, G. Pfeifer, Z. Cjeka, W. Baumeister, V. A. Fried, and D. Finley. A subcomplex of the proteasome regulatory particle required for ubiquitin-conjugate degradation and related to the COP9-signalosome and eIF3. *Cell*, 94(5):615–23, sep 1998a. ISSN 0092-8674.

M. H. Glickman, D. M. Rubin, V. A. Fried, and D. Finley. The regulatory particle of the Saccharomyces cerevisiae proteasome. *Molecular and cellular biology*, 18(6): 3149–3162, 1998b.

B. C. Goh, J. A. Hadden, R. C. Bernardi, A. Singharoy, R. McGreevy, T. Rudack, C. K. Cassidy, and K. Schulten. Computational Methodologies for Real-Space Structural Refinement of Large Macromolecular Complexes. *Annual Review of Biophysics*, 45(1):253–278, jul 2016. ISSN 1936-122X.

J. I. Goldstein, C. Lyman, D. Newbury, E. Lifshin, P. Echilin, L. Sawyer, D. Joy, and J. Michael. The SEM and Its Modes of Operation. In *Scanning Electron Microscopy and X-Ray microanalysis*, chapter 2, page 675. Springer US, Boston, MA, 3 edition, 2003. ISBN 0-306-47292-9.

T. A. Gomez, N. Kolawa, M. Gee, M. J. Sweredoski, and R. J. Deshaies. Identification of a functional docking site in the Rpn1 LRR domain for the UBA-UBL domain protein Ddi1. *BMC Biology*, 9:33, 2011.

B. J. Greber, D. Boehringer, M. Leibundgut, P. Bieri, A. Leitner, N. Schmitz, R. Aebersold, and N. Ban. The complete structure of the large subunit of the mammalian mitochondrial ribosome. *Nature*, 515(7526):283, oct 2014. ISSN 0028-0836.

R. Grimm, D. Typke, M. Bärmann, and W. Baumeister. Determination of the inelastic mean free path in ice by examination of tilted vesicles and automated most probable loss imaging. *Ultramicroscopy*, 63(3-4):169–179, jul 1996. ISSN 03043991.

M. Groll, L. Ditzel, J. Lowe, D. Stock, M. Bochtler, H. D. Bartunik, and R. Huber. Structure of 20S proteasome from yeast at 2.4 A resolution. *Nature*, 386(6624): 463–471, 1997.

M. Groll, M. Bajorek, A. Kohler, L. Moroder, D. M. Rubin, R. Huber, M. H. Glickman, and D. Finley. A gated channel into the proteasome core particle. *Nature structural biology*, 7(11):1062–1067, 2000.

J. Hamazaki, S. Iemura, T. Natsume, H. Yashiroda, K. Tanaka, and S. Murata. A novel proteasome interacting protein recruits the deubiquitinating enzyme UCH37 to 26S proteasomes. *The EMBO journal*, 25(19):4524–4536, 2006.

J. Hanna, N. A. Hathaway, Y. Tone, B. Crosas, S. Elsasser, D. S. Kirkpatrick, D. S. Leggett, S. P. Gygi, R. W. King, and D. Finley. Deubiquitinating enzyme Ubp6 functions noncatalytically to delay proteasomal degradation. *Cell*, 127(1):99–111, 2006.

J. He, K. Kulkarni, P. C. A. da Fonseca, D. Krutauz, M. H. Glickman, D. Barford, and E. P. Morris. The structure of the 26S proteasome subunit Rpn2 reveals its PC repeat domain as a closed toroid of two concentric α-helical rings. *Structure*, 20(3):513–21, mar 2012. ISSN 1878-4186.

R. Henderson. Image contrast in high-resolution electron microscopy of biological macromolecules: TMV in ice. *Ultramicroscopy*, 46(1-4):1–18, 1992. ISSN 03043991.

A. Hershko and A. Ciechanover. The ubiquitin system. *Annual review of biochemistry*, 67:425–479, 1998.

H. Hiyama, M. Yokoi, C. Masutani, K. Sugasawa, T. Maekawa, K. Tanaka, J. H. Hoeijmakers, and F. Hanaoka. Interaction of hHR23 with S5a. The ubiquitin-like domain of hHR23 mediates interaction with S5a subunit of 26 S proteasome. *The Journal of biological chemistry*, 274(39):28019–28025, 1999.

M. Hu, P. Li, L. Song, P. D. Jeffrey, T. A. Chenova, K. D. Wilkinson, R. E. Cohen, and Y. Shi. Structure and mechanisms of the proteasome-associated deubiquitinating enzyme USP14. *The EMBO journal*, 24(21):3747–3756, 2005.

X. Huang, B. Luan, J. Wu, and Y. Shi. An atomic structure of the human 26S proteasome. *Nature Structural & Molecular Biology*, 23(9):778–785, jul 2016. ISSN 1545-9993.

W. Humphrey, A. Dalke, and K. Schulten. VMD: visual molecular dynamics. *Journal of Molecular Graphics*, 14(1):27–28,33–38, 1996.

K. Husnjak, S. Elsasser, N. Zhang, X. Chen, L. Randles, Y. Shi, K. Hofmann, K. J. Walters, D. Finley, and I. Dikic. Proteasome subunit Rpn13 is a novel ubiquitin receptor. *Nature*, 453(7194):481–488, 2008.

T. Inobe, S. Fishbain, S. Prakash, and A. Matouschek. Defining the geometry of the two-component proteasome degron. *Nature chemical biology*, 7(3):161–167, 2011.

O. Iosefson, A. R. Nager, T. a. Baker, and R. T. Sauer. Coordinated gripping of substrate by subunits of a AAA+ proteolytic machine. *Nature Chemical Biology*, 11 (January):201–206, 2015. ISSN 1552-4450.

T. Jung and B. Catalgol. The proteasomal system. *Molecular Aspects of Medicine*, 30 (4):191–296, 2009. ISSN 00982997.

T. Jung and T. Grune. The proteasome and the degradation of oxidized proteins: Part I-structure of proteasomes. *Redox biology*, 1(1):178–82, 2013. ISSN 2213-2317.

A. V. Kajava. What curves alpha-solenoids? Evidence for an alpha-helical toroid structure of Rpn1 and Rpn2 proteins of the 26 S proteasome. *Journal of Biological Chemistry*, 277(51):49791–49798, dec 2002. ISSN 00219258.

K. W. Kaufmann, G. H. Lemmon, S. L. DeLuca, J. H. Sheehan, and J. Meiler. Practically Useful: What the R osetta Protein Modeling Suite Can Do for You. *Biochemistry*, 49(14):2987–2998, apr 2010. ISSN 0006-2960.

Y.-C. Kim, A. Snoberger, J. Schupp, and D. M. Smith. ATP binding to neighbouring subunits and intersubunit allosteric coupling underlie proteasomal ATPase function. *Nature communications*, 6:8520, 2015. ISSN 2041-1723.

D. Komander. Mechanism, specificity and structure of the deubiquitinases. *Subcellular biochemistry*, 54:69–87, 2010.

D. Komander, M. J. Clague, and S. Urbe. Breaking the chains: structure and function of the deubiquitinases. *Nature reviews. Molecular cell biology*, 10(8):550–563, 2009.

Y. Kravtsova-Ivantsiv and A. Ciechanover. Non-canonical ubiquitin-based signals for proteasomal degradation. *Journal of cell science*, 125(Pt 3):539–48, feb 2012. ISSN 1477-9137.

O. L. Krivanek, S. L. Friedman, A. J. Gubbens, and B. Kraus. An imaging filter for biological applications. *Ultramicroscopy*, 59(1-4):267–282, jul 1995. ISSN 03043991.

M. Kuijper, G. van Hoften, B. Janssen, R. Geurink, S. De Carlo, M. Vos, G. van Duinen, B. van Haeringen, and M. Storms. FEI's direct electron detector developments: Embarking on a revolution in cryo-TEM. *Journal of Structural Biology*, 192(2):179–187, 2015. ISSN 10958657.

G. C. Lander, E. Estrin, M. E. Matyskiela, C. Bashore, E. Nogales, and A. Martin. Complete subunit architecture of the proteasome regulatory particle. *Nature*, 482 (7384):186–191, 2012.

G. C. Lander, A. Martin, and E. Nogales. The proteasome under the microscope: the regulatory particle in focus. *Current Opinion in Structural Biology*, 23(2):243–251, 2013. ISSN 0959440X.

K. Lasker, F. Forster, S. Bohn, T. Walzthoeni, E. Villa, P. Unverdorben, F. Beck, R. Aebersold, A. Sali, and W. Baumeister. Molecular architecture of the 26S proteasome holocomplex determined by an integrative approach. *Proceedings of the National Academy of Sciences of the United States of America*, 109(5):1380–1387, 2012.

A. Leaver-Fay, M. Tyka, S. M. Lewis, O. F. Lange, J. Thompson, R. Jacak, K. W. Kaufman, P. D. Renfrew, C. A. Smith, W. Sheffler, I. W. Davis, S. Cooper, A. Treuille, D. J. Mandell, F. Richter, Y.-E. A. Ban, S. J. Fleishman, J. E. Corn, D. E. Kim, S. Lyskov, M. Berrondo, S. Mentzer, Z. Popović, J. J. Havranek, J. Karanicolas, R. Das, J. Meiler, T. Kortemme, J. J. Gray, B. Kuhlman, D. Baker, and P. Bradley. Chapter nineteen - Rosetta3: An Object-Oriented Software Suite for the Simulation and Design of Macromolecules. In *Methods in Enzymology*, volume 487, pages 545–574. 2011. ISBN 9780123812704.

B. H. Lee, M. J. Lee, S. Park, D. C. Oh, S. Elsasser, P. C. Chen, C. Gartner, N. Dimova, J. Hanna, S. P. Gygi, S. M. Wilson, R. W. King, and D. Finley. Enhancement of proteasome activity by a small-molecule inhibitor of USP14. *Nature*, 467(7312): 179–184, 2010.

B.-H. Lee, Y. Lu, M. A. Prado, Y. Shi, G. Tian, S. Sun, S. Elsasser, S. P. Gygi, R. W. King, and D. Finley. USP14 deubiquitinates proteasome-bound substrates that are ubiquitinated at multiple sites. *Nature*, 532(7599):398–401, 2016. ISSN 1476-4687.

M. J. Lee, B. H. Lee, J. Hanna, R. W. King, and D. Finley. Trimming of ubiquitin chains by proteasome-associated deubiquitinating enzymes. *Molecular & cellular proteomics : MCP*, 10(5):R110 003871, 2011.

D. S. Leggett, J. Hanna, A. Borodovsky, B. Crosas, M. Schmidt, R. T. Baker, T. Walz, H. Ploegh, and D. Finley. Multiple associated proteins regulate proteasome structure and function. *Molecular cell*, 10(3):495–507, 2002.

X. Li, P. Mooney, S. Zheng, C. R. Booth, M. B. Braunfeld, S. Gubbens, D. A. Agard, and Y. Cheng. Electron counting and beam-induced motion correction enable near-atomic-resolution single-particle cryo-EM. *Nature methods*, 10(6):584–590, 2013.

S. Lindert and J. A. McCammon. Improved cryoEM-Guided Iterative Molecular Dynamics–Rosetta Protein Structure Refinement Protocol for High Precision Protein Structure Prediction. *Journal of chemical theory and computation*, 11(3):1337–46, mar 2015. ISSN 1549-9626.

C. W. Liu, X. Li, D. Thompson, K. Wooding, T. L. Chang, Z. Tang, H. Yu, P. J. Thomas, and G. N. DeMartino. ATP binding and ATP hydrolysis play distinct roles in the function of 26S proteasome. *Molecular cell*, 24(1):39–50, 2006.

J. Löwe, D. Stock, B. Jap, P. Zwickl, W. Baumeister, and R. Huber. Crystal structure of the 20S proteasome from the archaeon T. acidophilum at 3.4 A resolution. *Science*, 268(5210):533–539, 1995.

Y. Lu, B. H. Lee, R. W. King, D. Finley, and M. W. Kirschner. Substrate degradation by the proteasome: a single-molecule kinetic analysis. *Science*, 348(6231):1250834, 2015.

B. Luan, X. Huang, J. Wu, Z. Mei, Y. Wang, X. Xue, C. Yan, J. Wang, D. J. Finley, Y. Shi, and F. Wang. Structure of an endogenous yeast 26S proteasome reveals two major conformational states. *Proceedings of the National Academy of Sciences of the United States of America*, 113(10):2642–7, mar 2016. ISSN 1091-6490.

A. Lupas, M. Van Dyke, and J. Stock. Predicting coiled coils from protein sequences. *Science (New York, N.Y.)*, 252(5010):1162–4, 1991. ISSN 0036-8075.

A. N. Lupas and M. Gruber. The Structure of α-Helical Coiled Coils. *Advances in Protein Chemistry*, 70:37–38, 2005. ISSN 00653233.

M. E. Matyskiela, G. C. Lander, and A. Martin. Conformational switching of the 26S proteasome enables substrate degradation. *Nature structural & molecular biology*, 20(7):781–788, 2013.

G. McMullan, A. R. Faruqi, D. Clare, and R. Henderson. Comparison of optimal performance at 300keV of three direct electron detectors for use in low dose electron microscopy. *Ultramicroscopy*, 147:156–163, 2014. ISSN 18792723.

A. Merk, A. Bartesaghi, S. Banerjee, V. Falconieri, P. Rao, M. I. Davis, R. Pragani, M. B. Boxer, L. A. Earl, J. L. S. Milne, and S. Subramaniam. Breaking Cryo-EM Resolution Barriers to Facilitate Article Breaking Cryo-EM Resolution Barriers to Facilitate Drug Discovery. *Cell*, 165(7):1–10, 2016. ISSN 0092-8674.

H. J. Meyer and M. Rape. Enhanced protein degradation by branched ubiquitin chains. *Cell*, 157(4):910–921, may 2014. ISSN 10974172.

T. Müller-Reichert, H. Hohenberg, E. T. O'Toole, and K. Mcdonald. Cryoimmobilization and three-dimensional visualization of C. elegans ultrastructure. In *Journal of Microscopy*, volume 212, pages 71–80. Blackwell Science Ltd, oct 2003.

I. Nagy, T. Tamura, J. Vanderleyden, W. Baumeister, and R. De Mot. The 20S proteasome of Streptomyces coelicolor. *Journal of bacteriology*, 180(20):5448–53, oct 1998. ISSN 0021-9193.

P. M. Neilsen, A. D. Pehere, K. I. Pishas, D. F. Callen, and A. D. Abell. New 26S proteasome inhibitors with high selectivity for chymotrypsin-like activity and p53-dependent cytotoxicity. *ACS Chemical Biology*, 8(2):353–359, feb 2013. ISSN 15548937.

S. Nickell, F. Förster, A. Linaroudis, W. D. Net, F. Beck, R. Hegerl, W. Baumeister, and J. M. Plitzko. TOM software toolbox: acquisition and analysis for electron tomography. *Journal of structural biology*, 149(3):227–234, 2005.

E. Nogales and S. H. W. Scheres. Cryo-EM: A Unique Tool for the Visualization of Macromolecular Complexity. *Molecular Cell*, 58(4):677–689, may 2015. ISSN 10974164.

K. Nyquist and A. Martin. Marching to the beat of the ring: Polypeptide translocation by AAA+ proteases. *Trends in Biochemical Sciences*, 39(2):53–60, 2014. ISSN 09680004.

A. O. Olivares, T. A. Baker, and R. T. Sauer. Mechanistic insights into bacterial AAA+ proteases and protein-remodelling machines. *Nature Reviews Microbiology*, 14(1):33–44, 2016. ISSN 1740-1526.

E. V. Orlova and H. R. Saibil. Structural analysis of macromolecular assemblies by electron microscopy. *Chemical reviews*, 111(12):7710–7748, 2011.

E. T. O'Toole. Chlamydomonas. Cryopreparation methods for the 3-D analysis of cellular organelles. *Methods in Cell Biology*, 96(C):71–91, 2010. ISSN 0091679X.

K. Paraskevopoulos, F. Kriegenburg, M. H. Tatham, H. I. Rosner, B. Medina, I. B. Larsen, R. Brandstrup, K. G. Hardwick, R. T. Hay, B. B. Kragelund, R. Hartmann-Petersen, and C. Gordon. Dss1 is a 26S proteasome ubiquitin receptor. *Molecular cell*, 56(3):453–461, 2014.

G. R. Pathare, I. Nagy, S. Bohn, P. Unverdorben, A. Hubert, R. Korner, S. Nickell, K. Lasker, A. Sali, T. Tamura, T. Nishioka, F. Förster, W. Baumeister, and A. Bracher. The proteasomal subunit Rpn6 is a molecular clamp holding the core and regulatory subcomplexes together. *Proceedings of the National Academy of Sciences of the United States of America*, 109(1):149–154, 2012.

G. R. Pathare, I. Nagy, P. Sledz, D. J. Anderson, H. J. Zhou, E. Pardon, J. Steyaert, F. Förster, A. Bracher, and W. Baumeister. Crystal structure of the proteasomal deubiquitylation module Rpn8-Rpn11. *Proceedings of the National Academy of Sciences of the United States of America*, 111(8):2984–2989, 2014.

P. A. Penczek. Resolution measures in molecular electron microscopy. *Methods in Enzymology*, 482(C):73–100, 2010. ISSN 00766879.

P. A. Penczek, M. Kimmel, and C. M. Spahn. Identifying conformational states of macromolecules by eigen-analysis of resampled cryo-EM images. *Structure*, 19 (11):1582–1590, 2011.

J.-M. Peters, Z. Cejka, J. Harris, J. A. Kleinschmidt, and W. Baumeister. Structural Features of the 26 S Proteasome Complex. *Journal of Molecular Biology*, 234(4): 932–937, dec 1993. ISSN 00222836.

A. Peth, H. C. Besche, and A. L. Goldberg. Ubiquitinated proteins activate the proteasome by binding to Usp14/Ubp6, which causes 20S gate opening. *Molecular cell*, 36(5):794–804, 2009.

A. Peth, T. Uchiki, and A. L. Goldberg. ATP-dependent steps in the binding of ubiquitin conjugates to the 26S proteasome that commit to degradation. *Molecular cell*, 40(4):671–681, 2010.

A. Peth, N. Kukushkin, M. Bosse, and A. L. Goldberg. Ubiquitinated proteins activate the proteasomal ATPases by binding to Usp14 or Uch37 homologs. *The Journal of biological chemistry*, 288(11):7781–7790, 2013.

S. Prakash, L. Tian, K. S. Ratliff, R. E. Lehotzky, and A. Matouschek. An unstructured initiation site is required for efficient proteasome-mediated degradation. *Nature structural & molecular biology*, 11(9):830–837, 2004.

L. Reimer and H. Kohl. *Transmission Electron Microscopy: Physics of Image Formation*, volume 36 of *Springer Series in Optical Sciences*. Springer New York, New York, NY, 5 edition, 2008. ISBN 978-0-387-40093-8.

H. Richly, M. Rape, S. Braun, S. Rumpf, C. Hoege, and S. Jentsch. A series of ubiquitin binding factors connects CDC48/p97 to substrate multiubiquitylation and proteasomal targeting. *Cell*, 120(1):73–84, jan 2005. ISSN 0092-8674.

A. Rigort, F. J. Bäuerlein, E. Villa, M. Eibauer, T. Laugks, W. Baumeister, and J. M. Plitzko. Focused ion beam micromachining of eukaryotic cells for cryoelectron tomography. *Proceedings of the National Academy of Sciences of the United States of America*, 109(12):4449–4454, mar 2012. ISSN 1091-6490.

A. Rohou and N. Grigorieff. CTFFIND4: Fast and accurate defocus estimation from electron micrographs. *Journal of Structural Biology*, 192(2):216–221, 2015. ISSN 10958657.

P. B. Rosenthal and R. Henderson. Optimal Determination of Particle Orientation, Absolute Hand, and Contrast Loss in Single-particle Electron Cryomicroscopy. *Journal of Molecular Biology*, 333(4):721–745, 2003. ISSN 00222836.

R. Rosenzweig, V. Bronner, D. Zhang, D. Fushman, and M. H. Glickman. Rpn1 and Rpn2 coordinate ubiquitin processing factors at proteasome. *The Journal of biological chemistry*, 287(18):14659–14671, 2012.

A. M. Ruschak, T. L. Religa, S. Breuer, S. Witt, and L. E. Kay. The proteasome antechamber maintains substrates in an unfolded state. *Nature*, 467(7317):868–71, oct 2010. ISSN 1476-4687.

R. S. Ruskin, Z. Yu, and N. Grigorieff. Quantitative characterization of electron detectors for transmission electron microscopy. *Journal of Structural Biology*, 184: 385–393, 2013.

Y. Saeki, T. Sone, A. Toh-e, and H. Yokosawa. Identification of ubiquitin-like protein-binding subunits of the 26S proteasome. *Biochemical and biophysical research communications*, 296(4):813–819, 2002.

E. Sakata, F. Stengel, K. Fukunaga, M. Zhou, Y. Saeki, F. Forster, W. Baumeister, K. Tanaka, and C. V. Robinson. The catalytic activity of Ubp6 enhances maturation of the proteasomal regulatory particle. *Molecular cell*, 42(5):637–649, 2011.

E. Sakata, S. Bohn, O. Mihalache, P. Kiss, F. Beck, I. Nagy, S. Nickell, K. Tanaka, Y. Saeki, F. Forster, and W. Baumeister. Localization of the proteasomal ubiquitin receptors Rpn10 and Rpn13 by electron cryomicroscopy. *Proceedings of the National Academy of Sciences of the United States of America*, 109(5):1479–1484, 2012.

A. Šali and T. L. Blundell. Comparative Protein Modelling by Satisfaction of Spatial Restraints. *Journal of Molecular Biology*, 234(3):779–815, dec 1993. ISSN 00222836.

R. T. Sauer and T. A. Baker. AAA+ proteases: ATP-fueled machines of protein destruction. *Annual review of biochemistry*, 80:587–612, 2011.

S. H. Scheres. Classification of structural heterogeneity by maximum-likelihood methods. *Methods in enzymology*, 482:295–320, 2010.

S. H. Scheres. RELION: implementation of a Bayesian approach to cryo-EM structure determination. *Journal of structural biology*, 180(3):519–530, 2012a.

S. H. Scheres, H. Gao, M. Valle, G. T. Herman, P. P. Eggermont, J. Frank, and J. M. Carazo. Disentangling conformational states of macromolecules in 3D-EM through likelihood optimization. *Nature methods*, 4(1):27–29, 2007.

S. H. Scheres, R. Nunez-Ramirez, C. O. Sorzano, J. M. Carazo, and R. Marabini. Image processing for electron microscopy single-particle analysis using XMIPP. *Nature protocols*, 3(6):977–990, 2008.

S. H. W. Scheres. A bayesian view on cryo-EM structure determination. *Journal of Molecular Biology*, 415(2):406–418, 2012b. ISSN 00222836.

M. Schmidt, J. Hanna, S. Elsasser, and D. Finley. Proteasome-associated proteins: regulation of a proteolytic machine. *Biological chemistry*, 386(8):725–737, 2005.

J. Schrader, F. Henneberg, R. A. Mata, K. Tittmann, T. R. Schneider, H. Stark, G. Bourenkov, and A. Chari. The inhibition mechanism of human 20S proteasomes enables next-generation inhibitor design. *Science (New York, N.Y.)*, 353 (6299):594–8, aug 2016. ISSN 1095-9203.

P. Schreiner, X. Chen, K. Husnjak, L. Randles, N. Zhang, S. Elsasser, D. Finley, I. Dikic, K. J. Walters, and M. Groll. Ubiquitin docking at the proteasome through a novel pleckstrin-homology domain interaction. *Nature*, 453(7194):548–552, 2008.

A. Schweitzer. *Kryo-EM Struktur des humanen 26S Protasoms*. Phd thesis, Technische Universität München, 2016.

A. Schweitzer, A. Aufderheide, T. Rudack, F. Beck, G. Pfeifer, J. M. Plitzko, E. Sakata, K. Schulten, F. Förster, and W. Baumeister. Structure of the human 26S proteasome at a resolution of 3.9 Å. *Proceedings of the National Academy of Sciences*, 113 (28):7816–7821, jul 2016. ISSN 0027-8424.

A. Sharipo, M. Imreh, A. Leonchiks, S. Imreh, and M. G. Masucci. A minimal glycine-alanine repeat prevents the interaction of ubiquitinated I kappaB alpha with the proteasome: a new mechanism for selective inhibition of proteolysis. *Nature Medicine*, 4(8):939–944, 1998.

Y. Shi, X. Chen, S. Elsasser, B. B. Stocks, G. Tian, B.-H. Lee, Y. Shi, N. Zhang, S. A. H. de Poot, F. Tuebing, S. Sun, J. Vannoy, S. G. Tarasov, J. R. Engen, D. Finley, and K. J. Walters. Rpn1 provides adjacent receptor sites for substrate binding and deubiquitination by the proteasome. *Science (New York, N.Y.)*, 351(6275), feb 2016. ISSN 1095-9203.

F. J. Sigworth. A maximum-likelihood approach to single-particle image refinement. *Journal of structural biology*, 122(3):328–39, 1998. ISSN 1047-8477.

F. J. Sigworth, P. C. Doerschuk, J. M. Carazo, and S. H. W. Scheres. *An introduction to maximum-likelihood methods in cryo-EM*, volume 482. Elsevier Inc., 1 edition, 2010. ISBN 9780123849915.

P. Sledz, P. Unverdorben, F. Beck, G. Pfeifer, A. Schweitzer, F. Förster, and W. Baumeister. Structure of the 26S proteasome with ATP-gammaS bound provides insights into the mechanism of nucleotide-dependent substrate translocation. *Proceedings of the National Academy of Sciences of the United States of America*, 110(18):7264–7269, 2013.

D. M. Smith, S. C. Chang, S. Park, D. Finley, Y. Cheng, and A. L. Goldberg. Docking of the proteasomal ATPases' carboxyl termini in the 20S proteasome's alpha ring opens the gate for substrate entry. *Molecular cell*, 27(5):731–744, 2007.

D. M. Smith, H. Fraga, C. Reis, G. Kafri, and A. L. Goldberg. ATP binds to proteasomal ATPases in pairs with distinct functional effects, implying an ordered reaction cycle. *Cell*, 144(4):526–538, 2011.

T. Sone, Y. Saeki, A. Toh-E, and H. Yokosawa. Sem1p Is a novel subunit of the 26 S proteasome from Saccharomyces cerevisiae. *Journal of Biological Chemistry*, 279 (27):28807–28816, jul 2004. ISSN 00219258.

C. O. S. Sorzano, R. Marabini, A. Pascual-Montano, S. H. W. Scheres, and J. M. Carazo. Optimization problems in electron microscopy of single particles. *Annals of Operations Research*, 148(1):133–165, 2006. ISSN 02545330.

C. M. Spahn and P. A. Penczek. Exploring conformational modes of macromolecular assemblies by multiparticle cryo-EM. *Current opinion in structural biology*, 19 (5):623–631, 2009.

B. M. Stadtmueller and C. P. Hill. Proteasome activators. *Molecular cell*, 41(1):8–19, jan 2011. ISSN 1097-4164.

J. E. Stone, R. McGreevy, B. Isralewitz, and K. Schulten. GPU-accelerated analysis and visualization of large structures solved by molecular dynamics flexible fitting. *Faraday Discuss.*, 169(0):265–283, mar 2014. ISSN 1359-6640.

J. Takeuchi, H. Chen, and P. Coffino. Proteasome substrate degradation requires association plus extended peptide. *The EMBO journal*, 26(1):123–131, 2007.

J. S. Thrower, L. Hoffman, M. Rechsteiner, and C. M. Pickart. Recognition of the polyubiquitin proteolytic signal. *The EMBO journal*, 19(1):94–102, jan 2000. ISSN 0261-4189.

G. Tian, S. Park, M. J. Lee, B. Huck, F. McAllister, C. P. Hill, S. P. Gygi, and D. Finley. An asymmetric interface between the regulatory and core particles of the proteasome. *Nature structural & molecular biology*, 18(11):1259–1267, 2011.

R. J. Tomko and M. Hochstrasser. Molecular architecture and assembly of the eukaryotic proteasome. *Annual review of biochemistry*, 82:415–45, 2013. ISSN 1545-4509.

R. J. Tomko, M. Funakoshi, K. Schneider, J. Wang, and M. Hochstrasser. Heterohexameric Ring Arrangement of the Eukaryotic Proteasomal ATPases: Implications for Proteasome Structure and Assembly. *Molecular Cell*, 38(3):393–403, may 2010. ISSN 10972765.

C. Toyoshima and N. Unwin. Contrast transfer for frozen-hydrated specimens: Determination from pairs of defocused images. *Ultramicroscopy*, 25(4):279–291, jan 1988. ISSN 03043991.

L. G. Trabuco, E. Villa, K. Mitra, J. Frank, and K. Schulten. Flexible fitting of atomic structures into electron microscopy maps using molecular dynamics. *Structure*, 16(5):673–683, 2008.

C. B. Trame and D. B. McKay. Structure of Haemophilus influenzae HslU protein in crystals with one-dimensional disorder twinning. *Acta Crystallographica Section D: Biological Crystallography*, 57(8):1079–1090, aug 2001. ISSN 09074449.

M. Unno, T. Mizushima, Y. Morimoto, Y. Tomisugi, K. Tanaka, N. Yasuoka, and T. Tsukihara. The structure of the mammalian 20S proteasome at 2.75 A resolution. *Structure*, 10(5):609–618, 2002. ISSN 09692126.

M. Unser, B. L. Trus, and A. C. Steven. A new resolution criterion based on spectral signal-to-noise ratios. *Ultramicroscopy*, 23(1):39–51, 1987. ISSN 03043991.

M. Unser, B. L. Trus, J. Frank, and A. C. Steven. The Spectral Signal-to-Noise Ratio Resolution Criterion: Computational Efficiency and Statistical Precision. *Ultramicroscopy*, 30:429–434, 1989. ISSN 1098-6596.

M. Unser, C. O. S. Sorzano, P. Thévenaz, S. Jonić, C. El-Bez, S. De Carlo, J. F. Conway, and B. L. Trus. Spectral signal-to-noise ratio and resolution assessment of 3D reconstructions. *Journal of Structural Biology*, 149(3):243–255, 2005. ISSN 10478477.

P. Unverdorben. *Pseudo-atomare Interpretation von Konformationsänderungen des 26S Proteasoms nach Klassifizierung von Kryo-Elektronenmikroskopie-Daten*. PhD thesis, Technische Universität München, 2014.

P. Unverdorben, F. Beck, P. Sledz, A. Schweitzer, G. Pfeifer, J. M. Plitzko, W. Baumeister, and F. Förster. Deep classification of a large cryo-EM dataset defines the conformational landscape of the 26S proteasome. *Proceedings of the National Academy of Sciences of the United States of America*, 111(15):5544–5549, 2014.

M. Van Heel. Similarity measures between images. *Ultramicroscopy*, 21(1):95–100, jan 1987. ISSN 03043991.

M. van Heel, B. Gowen, R. Matadeen, E. V. Orlova, R. Finn, T. Pape, D. Cohen, H. Stark, R. Schmidt, M. Schatz, and a. Patwardhan. Single-particle electron cryomicroscopy: towards atomic resolution. *Quarterly reviews of biophysics*, 33:307–369, 2000. ISSN 00335835.

S. van Nocker, S. Sadis, D. M. Rubin, M. Glickman, H. Fu, O. Coux, I. Wefes, D. Finley, and R. D. Vierstra. The multiubiquitin-chain-binding protein Mcb1 is a component of the 26S proteasome in Saccharomyces cerevisiae and plays a nonessential, substrate-specific role in protein turnover. *Molecular and cellular biology*, 16 (11):6020–6028, 1996.

R. Verma, L. Aravind, R. Oania, W. H. McDonald, J. R. Yates 3rd, E. V. Koonin, and R. J. Deshaies. Role of Rpn11 metalloprotease in deubiquitination and degradation by the 26S proteasome. *Science*, 298(5593):611–615, 2002.

D. Voges, P. Zwickl, and W. Baumeister. The 26S proteasome: a molecular machine designed for controlled proteolysis. *Annual review of biochemistry*, 68:1015–1068, 1999.

K. J. Walters, M. F. Kleijnen, A. M. Goh, G. Wagner, and P. M. Howley. Structural studies of the interaction between ubiquitin family proteins and proteasome subunit S5a. *Biochemistry*, 41(6):1767–1777, 2002.

K. J. Walters, P. J. Lech, A. M. Goh, Q. Wang, and P. M. Howley. DNA-repair protein hHR23a alters its protein structure upon binding proteasomal subunit S5a. *Proceedings of the National Academy of Sciences of the United States of America*, 100(22): 12694–12699, 2003.

T. Walzthoeni, M. Claassen, A. Leitner, F. Herzog, S. Bohn, F. Forster, M. Beck, and R. Aebersold. False discovery rate estimation for cross-linked peptides identified by mass spectrometry. *Nature methods*, 9(9):901–903, 2012.

X. Wang and L. Huang. Identifying dynamic interactors of protein complexes by quantitative mass spectrometry. *Molecular & cellular proteomics : MCP*, 7(1):46–57, 2008.

P. Wendler, S. Ciniawsky, M. Kock, and S. Kube. Structure and function of the AAA+ nucleotide binding pocket. *Biochimica et Biophysica Acta (BBA) - Molecular Cell Research*, 1823(1):2–14, 2012. ISSN 01674889.

T. Wenzel and W. Baumeister. Conformational constraints in protein degradation by the 20S proteasome. *Nature structural biology*, 2(3):199–204, 1995.

D. B. Williams and C. B. Carter. *Transmission electron microscopy: A textbook for materials science*. Springer US, Boston, MA, 2 edition, 2009. ISBN 9780387765006.

E. J. Worden, C. Padovani, and A. Martin. Structure of the Rpn11-Rpn8 dimer reveals mechanisms of substrate deubiquitination during proteasomal degradation. *Nature structural & molecular biology*, 21(3):220–7, mar 2014. ISSN 1545-9985.

T. Yao and R. E. Cohen. A cryptic protease couples deubiquitination and degradation by the proteasome. *Nature*, 419(6905):403–407, 2002.

F. Zhang, M. Hu, G. Tian, P. Zhang, D. Finley, P. D. Jeffrey, and Y. Shi. Structural insights into the regulatory particle of the proteasome from Methanocaldococcus jannaschii. *Molecular cell*, 34(4):473–484, 2009a.

F. Zhang, Z. Wu, P. Zhang, G. Tian, D. Finley, and Y. Shi. Mechanism of substrate unfolding and translocation by the regulatory particle of the proteasome from Methanocaldococcus jannaschii. *Molecular cell*, 34(4):485–496, 2009b.

Acknowledgements

The work of this theses was conducted in the group of Dr. Friedrich Förster within the department of Molecular Structural Biology at the Max-Planck Institute for Biochemistry in Martinsried. I would like to thank all department members for the good working atmosphere.
I am particularly grateful to the following people.

I would like to thank Prof. Dr. Baumeister for the supervision of this thesis and the excellent infrastructure, he has built up in the department.
Dr. Friedrich Förster was my direct supervisor and I am very grateful for his constant support, helpful advise and the proof-reading of this thesis in the middle of moving houses and workplace.
I would also like to acknowledge all members of my thesis advisory committee for their helpful comments during our annual meetings: Prof. Dr. Baumeister, Prof. Dr. Beckmann, Dr. Friedrich Förster and Dr. Eri Sakata.

I am grateful to Oana Mihalache, Günter Pfeifer and Dr. Jürgen Plitzko, who made this work possible through their help with the cryo-EM sample preparation and image acquisition.
I would like to particularly thank Florian Beck, who introduced me to the world of cryo-EM image processing, who has always been open for discussions and from whom I learned a lot about programming.

For the 26S–Ubp6 project, I received advice and support from many biochemists. I am very thankful to Dr. Eri Sakata and Andreas Schweitzer for fruitful discussions about the project and their help with wet lab experiments. I also thank Dr. Andreas Peth (Havard Medical School) for advice on Ubp6 purification, Claire Basquin from the Department of Structural Cell Biology for advise on the fluorogenic assays and Michaela Hartwig for help with purifications. Additionally, I thank our cooperation partner Dr. Florian Stengel from the University of Konstanz for the fast processing of the XL-MS data, he contributed to the 26S–Ubp6 project.

During the high-resolution project, I greatly enjoyed the team work with Andreas Schweitzer and our cooperation partner Dr. Till Rudack from the University of Illinois Urbana-Champaign. Thank you for this great science experience.

For the computational parts of this project, I spent a lot of time in the department's computer room and thank all 'inhabitants', among them Florian, Daniel, Shoh, Marc and Sahradah, for the fun times we have shared.

I am grateful to Birgit Book and Nathalie Leclercq for all their efforts to make bureaucracy run smoothly in the department and to Inga Wolf for help with computer hick-ups, data migration and her motivation to join a yoga class together with me. I would like to thank Stefan Pfeffer for his help here and there and Pia Unverdorben for teaching me her MDFF and Chimera skills, for proof-reading and for her friendship. I am also grateful to Daniel Bollschweiler and Stefanie Paarmann for (partially express-) proof-reading.

My boyfriend Matthias has prepared countless pre-cooked lunches during my time as a PhD candidate (thank you!) and I deeply thank him for always being there for me. Last but not least, I would like to thank my parents for their unconditional support and encouragement whenever needed.